

Electronic Thesis and Dissertation Repository

11-29-2010 12:00 AM

A New Signal Processing Approach to Study Action Potential Content in Sympathetic Neural Signals

Aryan Salmanpour
The University of Western Ontario

Supervisor

Dr. Lyndon Brown
The University of Western Ontario Joint Supervisor

Dr. Kevin Shoemaker
The University of Western Ontario

Graduate Program in Electrical and Computer Engineering

A thesis submitted in partial fulfillment of the requirements for the degree in Doctor of Philosophy

© Aryan Salmanpour 2010

Follow this and additional works at: <https://ir.lib.uwo.ca/etd>



Part of the [Electrical and Computer Engineering Commons](#)

Recommended Citation

Salmanpour, Aryan, "A New Signal Processing Approach to Study Action Potential Content in Sympathetic Neural Signals" (2010). *Electronic Thesis and Dissertation Repository*. 44.

<https://ir.lib.uwo.ca/etd/44>

This Dissertation/Thesis is brought to you for free and open access by Scholarship@Western. It has been accepted for inclusion in Electronic Thesis and Dissertation Repository by an authorized administrator of Scholarship@Western. For more information, please contact wlsadmin@uwo.ca.

A NEW SIGNAL PROCESSING APPROACH TO STUDY ACTION
POTENTIAL CONTENT IN SYMPATHETIC NEURAL SIGNALS

(Spine title: Action potential content in sympathetic recordings)

(Thesis format: Integrated Article)

by

Aryan Salmanpour

Graduate Program in Electrical and Computer Engineering

A thesis submitted in partial fulfillment
of the requirements for the degree of
Doctor of Philosophy

The School of Graduate and Postdoctoral Studies
The University of Western Ontario
London, Ontario, Canada

© Aryan Salmanpour 2010

THE UNIVERSITY OF WESTERN ONTARIO
School of Graduate and Postdoctoral Studies

CERTIFICATE OF EXAMINATION

Supervisor:

.....
Dr. Lyndon J. Brown

Co-Supervisor:

.....
Dr. J. Kevin Shoemaker

Supervisory Committee:

.....
Dr. James C. Lacefield

Examiners:

.....
Dr. James C. Lacefield

.....
Dr. Hanif Ladak

.....
Dr. Dwayne Jackson

.....
Dr. Andre Diedrich

The thesis by

Aryan Salmanpour

entitled:

A new signal processing approach to study action potential content in sympathetic neural signals

is accepted in partial fulfillment of the
requirements for the degree of
Doctor of Philosophy

.....
Date

.....
Chair of the Thesis Examination Board

Abstract

Sympathetic nerve activity plays an essential role in the normal regulation of blood pressure in humans and in the etiology and progression of many chronic diseases. Sympathetic nerve recordings associated with blood pressure regulation can be recorded directly using microneurography. A general characteristic of this signal is spontaneous burst activity of spikes (action potentials) separated by silent periods against a background of considerable gaussian noise. During measurement with electrodes, the raw muscle sympathetic nerve activity (MSNA) signal is amplified, band-pass filtered, rectified and integrated. This integration process removes important information regarding action potential content and their discharge properties.

The first objective of this thesis was to propose a new method for detecting action potentials from the raw MSNA signal to enable investigation of post-ganglionic neural discharge properties. The new method is based on the design of a mother wavelet that is matched to an actual mean action potential template extracted from a raw MSNA signal and applying it to the raw MSNA signal using a continuous wavelet transform (CWT) for spike detection. The performance of the proposed method versus two previous wavelet-based approaches was evaluated using 1) MSNA recorded from seven healthy participants and, 2) simulated MSNA. The results show that the new matched wavelet performs better than the previous wavelet-based methods that use a non-matched wavelet in detecting action potentials in the MSNA signal.

The second objective of this thesis was to employ the proposed action potential detection and classification technique to study the relationship between the recruitment of sympathetic action potentials (i.e., neurons) and the size of integrated sympathetic bursts in human MSNA signal. While in other neural systems (e.g. the skeletal motor system) there is a well understood pattern of neural recruitment during activation, our understanding of how sympathetic neurons are coordinated during baseline and baroreceptor unloading are very limited. We demonstrate that there exists a hierarchical pattern of recruitment of additional faster conducting neurons of larger amplitude as the sympathetic bursts become stronger. This information has important implications for how blood pressure is controlled, and the malleability of sympathetic activa-

tion in health and disease.

Keywords: Muscle sympathetic nerve activity, Action potential detection and classification, Microneurography, Wavelet analysis

Co-Authorship Statement

The following thesis contains the following manuscripts that have been published or submitted.

1. **A. Salmanpour**, L. J. Brown, J. K. Shoemaker, “Spike detection in human muscle sympathetic nerve activity using a matched wavelet approach,” *Journal of Neuroscience Methods*, vol. 193, pp. 343-355, 2010.
2. **A. Salmanpour**, L. J. Brown, C. Steinback, C. W. Usselman, R. Goswami and J. K. Shoemaker, “Relationship between size and latency of action potentials in human muscle sympathetic nerve activity,” *Journal of Neurophysiology*.
3. **A. Salmanpour**, L. J. Brown and J. K. Shoemaker, “Detection of Single Action Potential in Multi-unit Postganglionic Sympathetic Nerve Recordings in Humans: A Matched Wavelet Approach,” in *Proc IEEE Acoust Speech Signal Processing*, pp. 554-557, 2010.
4. **A. Salmanpour**, L. J. Brown and J. K. Shoemaker, “Detection and Classification of Raw Action Potential Patterns in Human Muscle Sympathetic Nerve Activity,” in *Proc IEEE Eng Med Biol Soc*, pp. 2928-31, 2008.
5. **A. Salmanpour**, L. J. Brown and J. K. Shoemaker, “Performance Analysis of Stationary and Discrete Wavelet Transform for Action Potential Detection from Sympathetic Nerve Recordings in Humans,” in *Proc IEEE Eng Med Biol Soc*, pp. 2932-5, 2008.

These studies were designed by A Salmanpour, LJ Brown and JK Shoemaker. Co-authors provided experimental support as follows:

C Steinback, CW Usselman and R Goswami provided the real MSNA data for study 2.

All software development, data analysis and the drafting of original manuscripts for the present thesis were performed by A Salmanpour. Co-authors provided editorial feedback as necessary.

Acknowledgements

I would like to acknowledge all the people who made this work possible. First of all, I would like to thank my advisors, Dr. Brown and Dr. Shoemaker, for their supports and guidance during the past four years. Without their supports, this work would not have been a reality.

I would also like to thank all my friends at Neurovascular Research laboratory (NVRL) that supported and helped me during this work. Finally, I would like to thank my family and my wife, for their support during this work.

Contents

| | |
|---|------------|
| Certificate of Examination | ii |
| Abstract | iii |
| Co-Authorship Statement | v |
| Acknowledgements | vi |
| List of Tables | xi |
| List of Figures | xii |
| 1 Introduction | 1 |
| 1.1 Microneurography: a direct method to assess autonomic function | 3 |
| 1.2 Integrated MSNA burst Analysis | 8 |
| 1.2.1 General quantification | 8 |
| 1.2.2 Integrated burst reflex latency | 10 |
| 1.2.3 Baroreflex pressure threshold and baroreflex sensitivity analyses | 14 |
| 1.3 Drawbacks and limitations of the integrated burst analysis | 17 |
| 1.4 Spike Detection in human MSNA signal | 19 |
| 1.5 Objective and Outline of this thesis | 22 |
| 1.6 Contributions of the author | 23 |
| References | 24 |

| | |
|--|-----------|
| 2 Spike detection using stationary and discrete wavelet transform from sympathetic nerve recordings in humans | 30 |
| 2.1 Introduction | 30 |
| 2.2 Background | 32 |
| 2.2.1 Discrete Wavelet Transform (DWT) | 32 |
| 2.2.2 Stationary or Undecimated Wavelet Transform (SWT) | 36 |
| 2.2.3 Wavelet-Denoising: Thresholding and Noise Estimation | 37 |
| 2.3 Materials and Methods | 37 |
| 2.3.1 Data acquisition and recording conditions | 37 |
| 2.3.2 Proposed method for action potential detection | 40 |
| 2.3.3 The method for generating simulated MSNA | 40 |
| 2.4 Results | 44 |
| 2.4.1 Comparison between DWT and SWT | 44 |
| 2.4.2 An averaged action potential after band-pass filtering | 47 |
| 2.4.3 An averaged action potential before pre-Amplification | 50 |
| 2.4.4 Action potential classification | 54 |
| 2.5 Conclusion | 56 |
| References | 56 |
| | |
| 3 Spike detection in human muscle sympathetic nerve activity using a matched wavelet approach | 60 |
| 3.1 Introduction | 60 |
| 3.2 Materials and Methods | 64 |
| 3.2.1 Data acquisition and recording conditions | 64 |
| 3.2.2 Action potential detection using a matched wavelet | 67 |
| 3.2.3 Wavelet decomposition using continuous wavelet transform with matched wavelet | 68 |
| 3.2.4 Matching a wavelet to the mean action potential template | 70 |

| | | |
|-------|---|----|
| 3.2.5 | A new method for generating simulated MSNA signal | 73 |
| 3.2.6 | Evaluation of detection performance using simulated data | 77 |
| 3.2.7 | Performance evaluation of the algorithm on overlapping spikes | 78 |
| 3.2.8 | Validation using lower body negative pressure protocol | 79 |
| 3.3 | Results | 80 |
| 3.3.1 | Matching a wavelet to the mean action potential template | 80 |
| 3.3.2 | Evaluation of detection performance using simulated data | 83 |
| 3.3.3 | Performance evaluation of the algorithm on overlapping spikes | 85 |
| 3.3.4 | Validation using lower body negative pressure protocol | 88 |
| 3.4 | Discussion | 90 |
| 3.5 | Appendix A: Algorithms for designing a matched wavelet | 92 |
| 3.5.1 | Wavelet analysis and pattern detection | 92 |
| 3.5.2 | Conditions for an orthonormal multiresolution analysis | 93 |
| 3.5.3 | Matching discrete spectrum magnitude | 94 |
| 3.5.4 | Matching discrete spectrum phase | 95 |
| | References | 96 |

4 Relationship between size and latency of action potentials in human muscle

| | | |
|-------|---|------------|
| | sympathetic nerve activity | 103 |
| 4.1 | Introduction | 103 |
| 4.2 | Methods | 105 |
| 4.2.1 | Subjects | 105 |
| 4.2.2 | Experimental Protocol | 106 |
| 4.2.3 | Sympathetic Neural Recordings | 106 |
| 4.2.4 | Integrated MSNA burst Analysis | 107 |
| 4.2.5 | Action Potential Detection and Analysis | 108 |
| 4.2.6 | Action Potential Summation Simulation | 109 |
| 4.2.7 | Statistical Analysis | 110 |

| | | |
|----------|--|------------|
| 4.3 | Results | 110 |
| 4.3.1 | Baseline vs. LBNP -60 mmHg | 111 |
| | Integrated Bursts Analysis | 111 |
| | Action Potential Analysis | 115 |
| 4.3.2 | Baseline vs. LBNP -80 mmHg | 122 |
| 4.4 | Discussion | 126 |
| 4.4.1 | Integrated burst and action potential Analysis | 126 |
| 4.4.2 | Action Potential Size - Latency Relationship | 128 |
| 4.4.3 | Baroreflex Control? | 129 |
| 4.4.4 | Limitations | 130 |
| 4.4.5 | Summary and Conclusions | 131 |
| 4.5 | Acknowledgments | 131 |
| | References | 131 |
| 5 | Conclusions | 135 |
| 5.1 | Summary of results | 136 |
| 5.2 | Overall Conclusions | 138 |
| 5.3 | Future Directions | 140 |
| | References | 141 |
| | Curriculum Vitae | 143 |

List of Tables

| | | |
|-----|---|-----|
| 2.1 | some statistical information about each subject | 49 |
| 2.2 | Distributions of 3 classes found from all 3 subjects | 55 |
| 4.1 | Post-ganglionic sympathetic action potentials (AP) and action potential clusters within sympathetic bursts detected at baseline and LBNP -60 mmHg for each participant. | 115 |
| 4.2 | Sympathetic burst parameters at baseline and LBNP -80 mmHg for group (B). . | 124 |
| 4.3 | Post-ganglionic sympathetic action potentials (AP) and action potential clusters within sympathetic bursts detected at baseline and LBNP -80 mmHg for group (B). | 124 |

List of Figures

| | | |
|------|---|----|
| 1.1 | The peroneal nerve | 5 |
| 1.2 | The technique of microneurography | 6 |
| 1.3 | Common signal conditioning steps during recording of muscle sympathetic nerve activity. | 7 |
| 1.4 | General methods of quantifying integrated MSNA signal. | 9 |
| 1.5 | The inverse relationship between blood pressure and MSNA | 12 |
| 1.6 | The reflex latency | 13 |
| 1.7 | The relationship between variations in blood pressure and MSNA. | 15 |
| 1.8 | The baroreflex threshold and sensitivity diagrams. | 16 |
| 1.9 | The fused burst patterns | 18 |
| 1.10 | General concept of spike detection and classification | 21 |
| 2.1 | The Symlet 7 wavelet | 35 |
| 2.2 | The raw and integrated MSNA signals | 39 |
| 2.3 | The block diagram of the Iowa nerve traffic analysis system 662C-3 | 39 |
| 2.4 | The power spectral density (PSD) of the measured and simulated noise | 42 |
| 2.5 | Simulated bursts of action potentials with SNR=3. | 43 |
| 2.6 | Mean results for simulations with varied noise levels. | 46 |
| 2.7 | The complete process for finding the averaged action potential after bandpass filtering. | 48 |
| 2.8 | Averaged action potentials for all subjects after bandpass filtering. | 49 |

| | | |
|------|--|-----|
| 2.9 | Illustration of the method for finding mean AP template before the bandpass filter and after electrodes | 52 |
| 2.10 | Averaged action potentials for all subjects before pre-amplification (after electrodes). | 53 |
| 2.11 | An ideal action potential waveform. | 53 |
| 2.12 | Classification of action potential waveforms | 55 |
| 3.1 | The cross-section of the peroneal nerve and common signal conditioning of the MSNA signal | 66 |
| 3.2 | Detected and mean action potential templates in five subjects. | 72 |
| 3.3 | Illustration of the simulation components. | 75 |
| 3.4 | A simulated burst at two different SNRs. | 76 |
| 3.5 | Designing a wavelet match to the mean action potential template | 81 |
| 3.6 | Performance of the new action potential detection method on the real MSNA signal. | 82 |
| 3.7 | Mean results for simulations with varied noise levels, mean burst rate and action potential rate | 84 |
| 3.8 | Performance of the MWD method to the overlapping spike signal | 87 |
| 3.9 | Comparison of spike detection and burst parameters during a lower body negative pressure (LBNP) protocol | 89 |
| 4.1 | A representative example of filtered raw and integrated muscle sympathetic nerve activity | 112 |
| 4.2 | The occurrence of sympathetic bursts in relation to diastolic blood pressure | 113 |
| 4.3 | Relationship between relative integrated burst size and corresponding reflex latencies at baseline (A) and LBNP -60 mmHg (B) | 114 |
| 4.4 | Mean action potential clusters | 116 |

| | | |
|-----|---|-----|
| 4.5 | Relationship between action potential content and relative integrated burst size during baseline and LBNP | 118 |
| 4.6 | The relationship between the occurrence of individual action potential clusters as a function of burst amplitude in one subject during baseline (A) and LBNP -60 mmHg (B) | 120 |
| 4.7 | Mean action potential latency for each cluster as a function of normalized cluster amplitude (cluster 1 = 100%) for each participant during baseline (A) and at LBNP -60 mmHg (B) | 121 |
| 4.8 | A representative example of filtered raw and integrated muscle sympathetic nerve activity at rest (A) and LBNP -80 mmHg (B). | 123 |
| 4.9 | The relationship between the occurrence of individual action potential clusters as a function of burst amplitude in one subject during baseline (A) and LBNP -80 mmHg (B) | 125 |

Chapter 1

Introduction

The autonomic nervous system (ANS) regulates many physiologic processes autonomously, that is, without conscious controls. The two major divisions are the sympathetic and parasympathetic systems. Disorders of the ANS cause autonomic insufficiency or failure and can affect any system of the body. Therefore, understanding and studying of both the normal and abnormal characteristics of the ANS is very important. For instance, conditions like hypertension [1–3], congestive heart failure [4] and obesity [5, 6] are associated with autonomic dysregulation.

One of the powerful research tools used to directly assess autonomic function and to examine the origin of many autonomic disorders is a technique developed by Hagbarth and Vallbo [7]. The technique is known as Microneurography and consists of directly recording the sympathetic nerve activity from a peripheral nerve in awake subjects. Microneurography has provided an exciting era in research regarding autonomic outflow and the neural control of the cardiovascular system with opportunities to study neurovascular control in skeletal muscle [8] and blood pressure regulation [9]. Researchers have been using this technique to study the relationship between the sympathetic nerve activity and hypertension [1–4] and other diseases.

The human muscle sympathetic nerve activity (MSNA), a signal recorded using microneurography, is generated by multiple neurons supplying the muscle vascular bed in human sub-

jects. A general characteristic of this signal is the spontaneous burst activity of spikes (action potentials) that are time-locked with the cardiac cycle and separated by silent periods against a background of considerable gaussian noise. Traditionally, due to relatively poor signal-to-noise aspects of this neurogram, analysis of this multi-fiber recording from human peripheral nerves has, to a large extent, been constrained to the integrated neurogram signal through band-pass filtering, rectification and integration. These steps reduce background noise and provide a quantitative measure of sympathetic outflow, but eliminate action potential information. For instance, the number of action potentials and their morphologies that contribute to a given sympathetic burst are lost during integration process.

The main reasons for studying action potential content are: 1) Loss of information that occurs in the integration process, 2) Potential for recruitment of different post-ganglionic neuronal populations and 3) Population differences in recruitment patterns. Detail of coding patterns in the single action potentials should, in theory, provide information about recruitment strategies used by the central nervous system to achieve the spontaneous activity and stress responses. However, this high frequency content of the signal is lost in the integrated signal. Understanding the recruitment patterns of sympathetic neurons may have important implications for how blood pressure and blood flow are controlled, and the malleability of sympathetic activation in health and disease.

Therefore, to retrieve the action potential content of the multi-fibre recording for variations in action potential frequency, morphology and timing, it is necessary to develop alternative techniques to extract the action potentials from the noisy neurogram. Developing a reliable method for detecting and extracting action potentials from a noisy raw sympathetic signal and applying such a method to retrieve action potential content in real MSNA signal are major objectives of this thesis.

In the subsequent sections we review 1) the microneurography for recording of the MSNA signal, 2) the traditional analysis of the MSNA signal, 3) the limitation and drawbacks of this analysis and 4) an alternative method to overcome these limitations followed by the objectives

of this thesis.

1.1 Microneurography: a direct method to assess autonomic function

Post-ganglionic efferent sympathetic nerve traffic to muscle and skin vascular beds can be measured directly using the microneurography which involves inserting metal microelectrodes percutaneously into mixed peripheral nerves [7]. Efferent sympathetic nerve activity is carried by unmyelinated “C” fibres whose conduction velocities are about 1 m/s [11]. Since the unmyelinated nerve fibres tend to be grouped in bundles it is possible to insert the tip of an electrode in their vicinity and record their activity.

Sympathetic nerve traffic, dependent on the goal of the study, can be recorded from any human mixed nerve that is accessible to a recording electrode. The peroneal (fibular) nerve is used widely for measuring nerve traffic to a skeletal muscle vascular bed. Fig. 1.1 shows the position of the peroneal nerve. The sympathetic nerve activity can be recorded from bundles of either skin or muscle nerve fibers. The muscle bundles in the peroneal nerve contain sensory nerves from muscle spindles, efferent motor nerves and efferent sympathetic nerves. The neural activity recorded from efferent sympathetic nerves innervating the vessels in the muscle is called muscle sympathetic nerve activity (MSNA). This signal is defined as “multi-unit” in that several axons are recorded from simultaneously. Bursts of sympathetic activity in muscle nerves are tightly linked to the cardiac cycle [7] whereas those directed to skin are not.

Typically, recordings of MSNA are obtained using a 200 μm diameter, 35 mm long tungsten microelectrode tapering to an uninsulated 1 to 5 μm tip. This electrode is inserted percutaneously into the nerve just posterior to the fibular head. A reference electrode is positioned subcutaneously 1-3 cm from the recording site. Fig. 1.2 shows the position of recording electrode, reference electrode and pre-amplifier. An MSNA site is confirmed by manually manipulating the microelectrode until a characteristic pulse-synchronous burst pattern is observed. Satisfac-

tory recordings of MSNA are usually defined by (1) heart pulse synchronicity (2) increases in response to breath-holding (3) facilitation during Valsalva straining and suppression during the hypertensive overshoot after release and (4) no change during tactile or auditory stimulation [8].

The recorded neural signal is usually amplified with gain ~ 75000 , bandpass filtered (700-2000 Hz), rectified and integrated (resistance-capacitance integrator circuit, time constant 0.1 s). These processes can be implemented using custom-made or commercially available hardware (e.g., one source is nerve traffic analysis system model 662C-3, Bioengineering of University of Iowa, Iowa City, IA). Fig. 1.3 shows these signal conditioning steps during recording of the MSNA signal. A single-unit sympathetic nerve activity can be recorded with the same technique described above. The only difference is that the microelectrode must have a much higher impedance so that it can limit the area from which the neural activity is recorded [14].

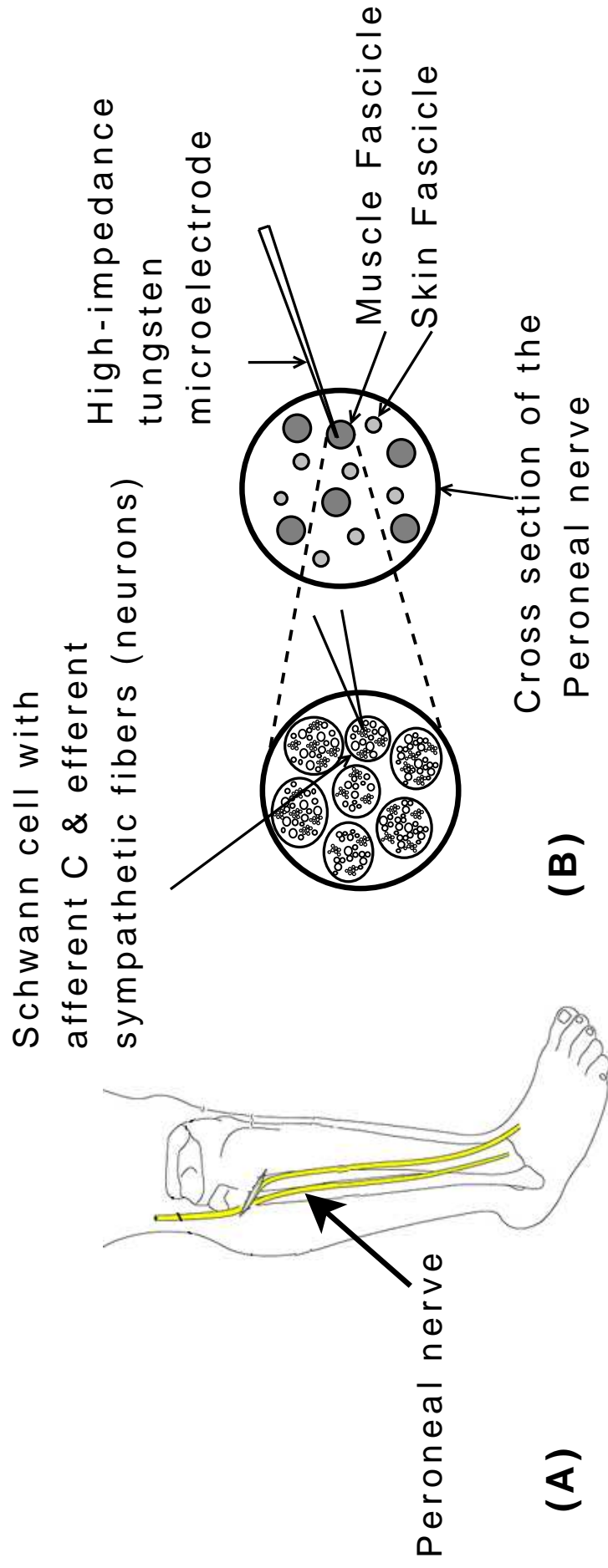


Figure 1.1: The peroneal nerve. (A) The anatomical position of the Peroneal nerve. (B) Schematic representation of a microelectrode inserted into a human peripheral nerve for sympathetic recordings. The nerve contains bundles of sympathetic nerves that target blood vessels in muscle or skin, Adapted from [12, 13]

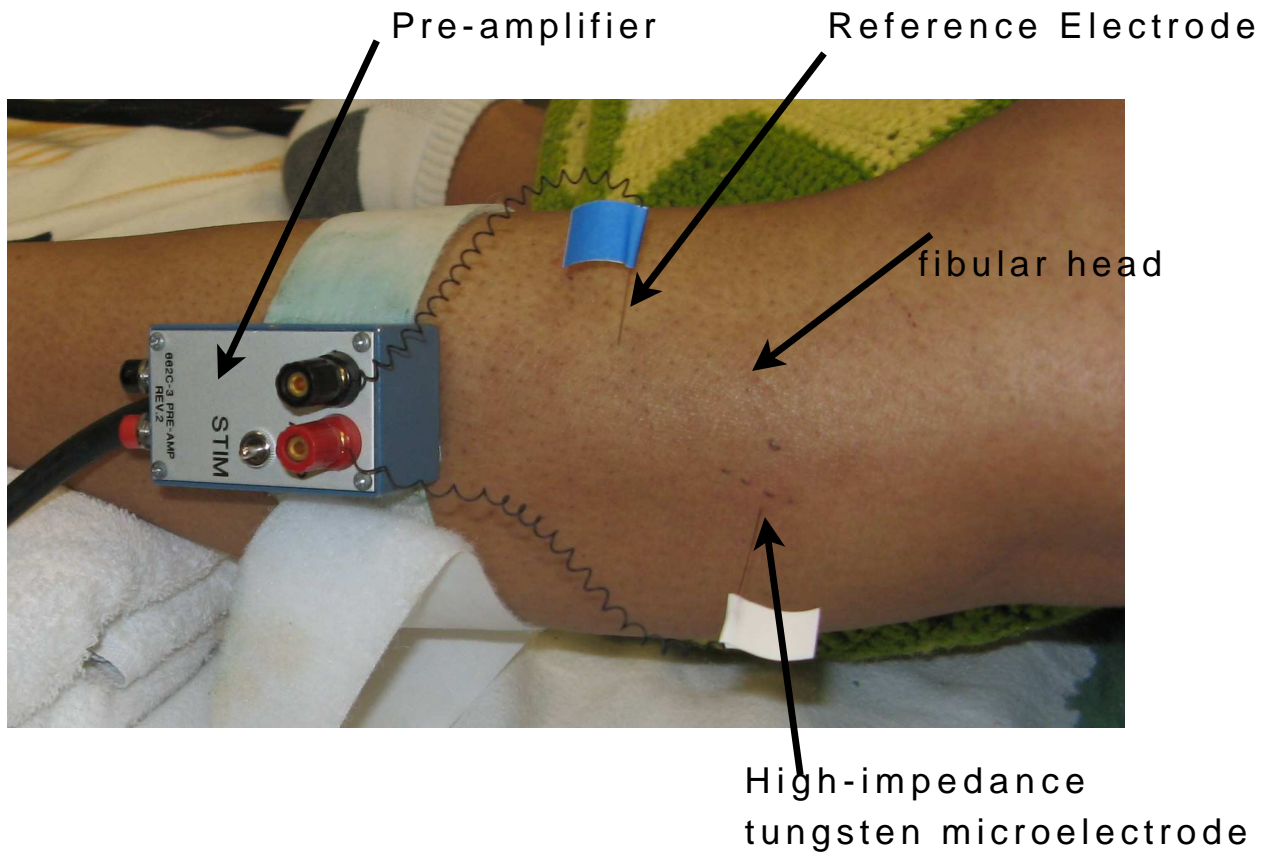


Figure 1.2: The technique of microneurography. Position of recording electrode, reference electrode, fibular head and pre-amplifier during Microneurography.

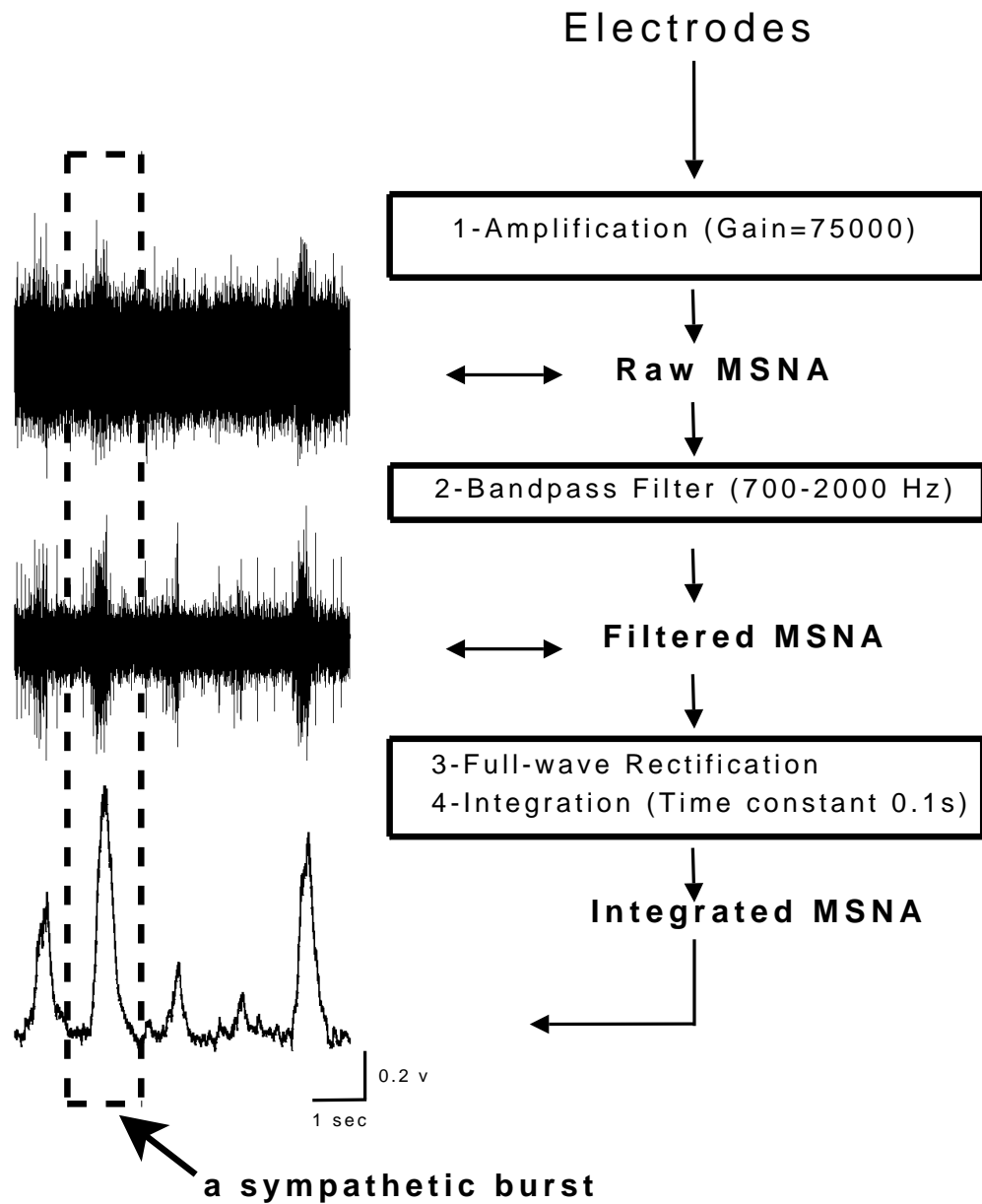


Figure 1.3: Common signal conditioning steps during recording of muscle sympathetic nerve activity. The recorded raw neurogram is amplified, band-pass filtered and integrated. A sympathetic burst is shown with a dashed rectangle.

1.2 Integrated MSNA burst Analysis

1.2.1 General quantification

An important but problematic feature of the MSNA signal is that it is dominated by high levels of environmental and bioelectric background noise that produce a low signal-to-noise neurogram. Traditionally, due to relatively poor signal-to-noise aspects of this neurogram, analysis of this multi-fiber recording from human peripheral nerves has been constrained to the integrated neurogram signal through band-pass filtering, rectification and integration as mentioned above. These steps reduce background noise and provide a quantitative measure of sympathetic outflow.

The amount of integrated neural activity is often quantified both as number of bursts per 100 heartbeats (burst incidence) and burst per min (burst frequency). Also, the total MSNA activity can be described as the product of burst incidence/burst frequency \times averaged burst area/amplitude (in arbitrary unit) [15]. Figure 1.4 shows these traditional quantification of MSNA signal. Sundolf and Wallin [15] showed that the burst frequency is highly repeatable between recording sessions for the same individual.

The amplitude of a given sympathetic burst is a function of the number and size of action potentials present in the recorded signal. However, measures of burst amplitude/area are difficult to compare between individuals because the burst areas/amplitudes are highly dependent on the proximity of the electrode tip to the group of post-ganglionic sympathetic axons from which the recording is made. Attempts have been made to quantify burst amplitude by normalizing burst amplitude/area to the largest burst in a recording and calculating the distribution of burst amplitudes [15, 16]. Although these techniques have been relatively successful in identifying differences in overall burst intensity across subjects [17, 18] the information content extracted from these approaches is still relatively limited. However, it might be useful for calculating burst amplitude changes by normalizing them within a given recording session.

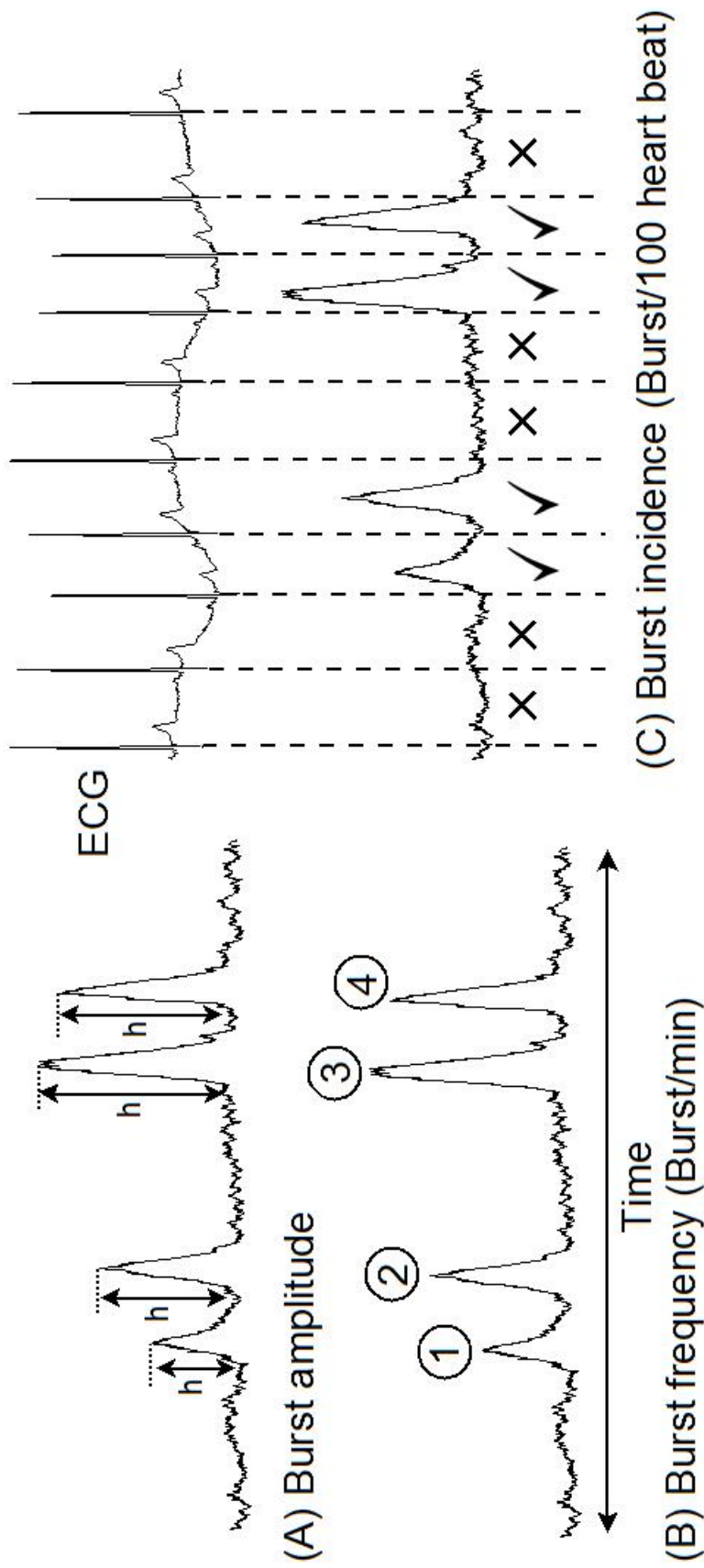


Figure 1.4: General methods of quantifying integrated MSNA signal. (A) Burst amplitude is determined from the peak burst heights across bursts (h). (B) Burst frequency is calculated by identifying the number of bursts (e.g. 1, 2, 3 and 4 above) occurring within a specific of time (t). (C) Burst incidence is the number of bursts occurring over 100 consecutive heart beats.

1.2.2 Integrated burst reflex latency

The MSNA signal consists of pulse synchronous bursts of action potentials that occur during temporary reduction in blood pressure and vanish during transient elevations of blood pressure [8, 9]. The inverse relationship between MSNA and blood pressure is due to arterial baroreflex modulation of sympathetic vasoconstrictor outflow.

The baroreflex begins with stretch sensitive cells known as baroreceptors. These are sensory receptors found in the wall of blood vessels in the region of the carotid sinus, aorta, heart, and lungs. These receptors are sensitive to vascular stretch induced by blood pressure and send coded nerve impulses concerning the blood pressure fluctuations to the nucleus of the tractus solitarius (NTS) in the medulla [10]. The NTS sends excitatory messages to the caudal ventrolateral medulla (CVLM), activating the CVLM. The activated CVLM then sends inhibitory messages to the rostral ventrolateral medulla (RVLM), thus inhibiting the RVLM. The RVLM is the primary regulator of the sympathetic nervous system, sending excitatory messages to the sympathetic preganglionic neurons located in the intermediolateral nucleus of the spinal cord. Therefore, when the baroreceptors are activated (by an increased blood pressure), the NTS activates the CVLM, which in turn inhibits the RVLM, thus inhibiting the sympathetic branch of the autonomic nervous system leading to a decrease in blood pressure (i.e., vasodilation). The NTS additionally activates Nucleus Ambiguus increasing parasympathetic activity resulting in a reduction of heart rate and cardiac contractility. The parasympathetic excitation mainly works to further reduce the heart rate until blood pressure returns to a normal level. The decrease in the cardiac output and peripheral resistance causes a reduction in the blood pressure. Likewise, low blood pressure causes an increase in sympathetic tone via “disinhibition” (i.e., activation) of the RVLM, leading to vasoconstriction.

There is a delay between the detection of blood pressure reduction by baroreceptors and the occurring of sympathetic bursts (see Fig. 1.5), termed “reflex latency”. Reflex latency is often determined using the approach introduced by Fagius and Wallin [11] and is based upon the time delay between the peak of the burst (the highest point of the integrated MSNA burst) and the

R-wave related to the burst (generally the R-wave occurrence of the previous cardiac cycles); see Fig. 1.6. Reflex latency is a convenient indirect measurement of conduction velocity in pre and post-ganglionic sympathetic fibres [11]. The reflex latency measurements can be used for comparison between individual sympathetic bursts or across individuals for different purposes.

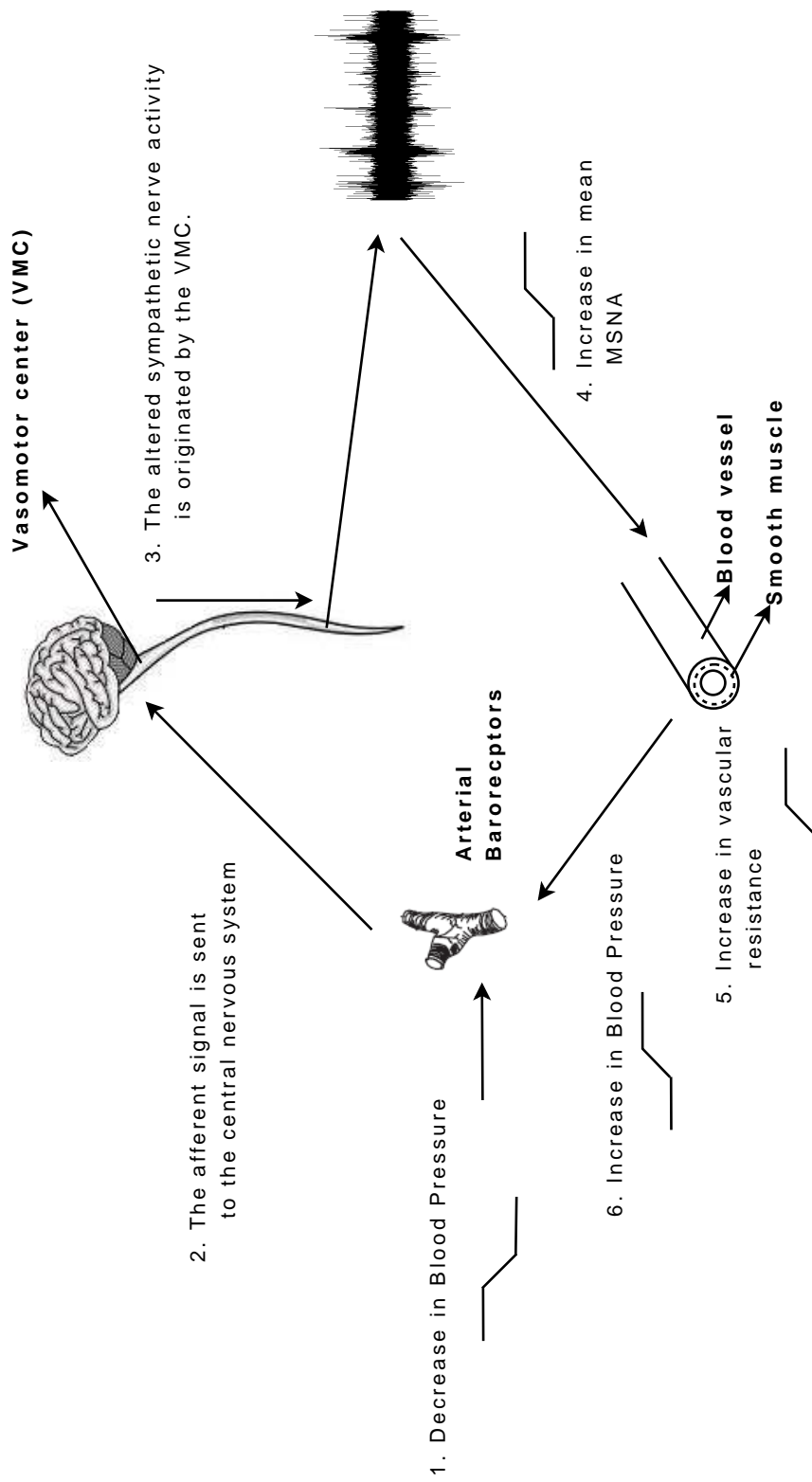


Figure 1.5: The schematic representation of inverse relationship between muscle sympathetic nerve activity and blood pressure fluctuations. Notice a reduction in the blood pressure is detected by baroreceptors and the MSNA will be increased eventually using baroreflex.

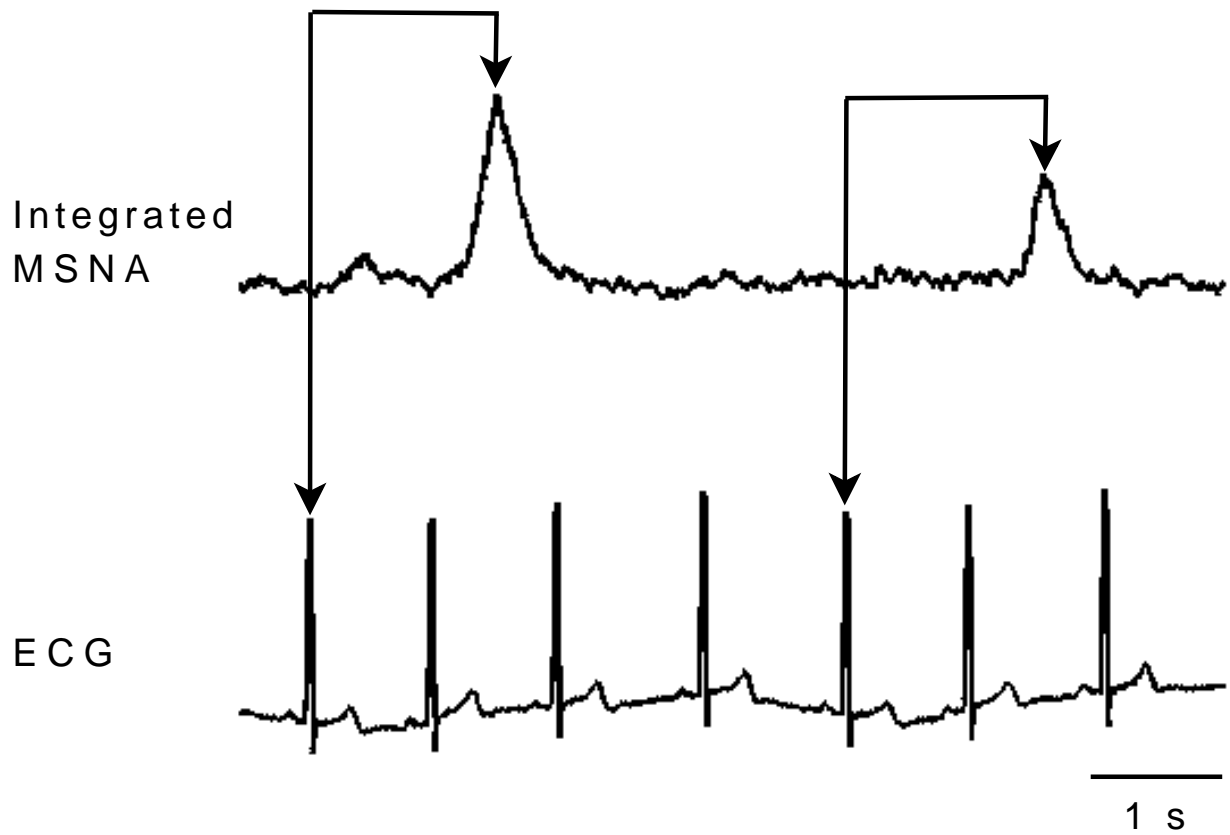


Figure 1.6: The reflex latency. Examples for finding reflex latency for individual bursts in relation to preceding R-waves.

1.2.3 Baroreflex pressure threshold and baroreflex sensitivity analyses

In general, the sympathetic bursts occur more frequently during spontaneous transient blood pressure reductions than during transient increases in blood pressure (see Fig. 1.7). It has been shown that there is a close negative correlation between the occurrence of a sympathetic burst and diastolic blood pressure and a low correlation to systolic blood pressure [9]. To study the effects of spontaneous temporary blood pressure fluctuations, researchers have investigated the correlation between the diastolic blood pressure of individual heart beats to the probability of occurrence of a sympathetic burst (baroreflex pressure threshold) and to the amplitude of the occurring bursts (baroreflex sensitivity) [9, 19, 20].

Baroreflex threshold diagram: Diastolic pressures of individual heart beats are grouped in intervals of 1 mmHg and for each interval burst incidence (i.e., occurrence of sympathetic bursts in 100 heart beats) is calculated and plotted against the mean of the pressure interval. It is common to calculate the threshold (T_{50}) value which is defined as the diastolic pressure at which 50% of the diastolic blood pressures are associated with a burst. The variability of the threshold is defined as the slope of the regression line [9]. Fig. 1.8A shows an example of a baroreflex threshold diagram from a female participant.

Baroreflex sensitivity diagram: Baroreflex sensitivity is evaluated in a linear regression analysis of individual sympathetic burst amplitude or area versus the diastolic blood pressure during the cardiac interval corresponding to the burst. The sensitivity is defined as the slope of the regression line. An example of baroreflex sensitivity analysis is shown in Fig. 1.8B.

It has been shown that the baroreflex threshold diagram is a robust measure of baroreflex function and it is highly reproducible. In contrast, the strength of a sympathetic burst is only weakly coupled to diastolic pressure and this relationship is not an appropriate tool for analysis of baroreflex function [19].

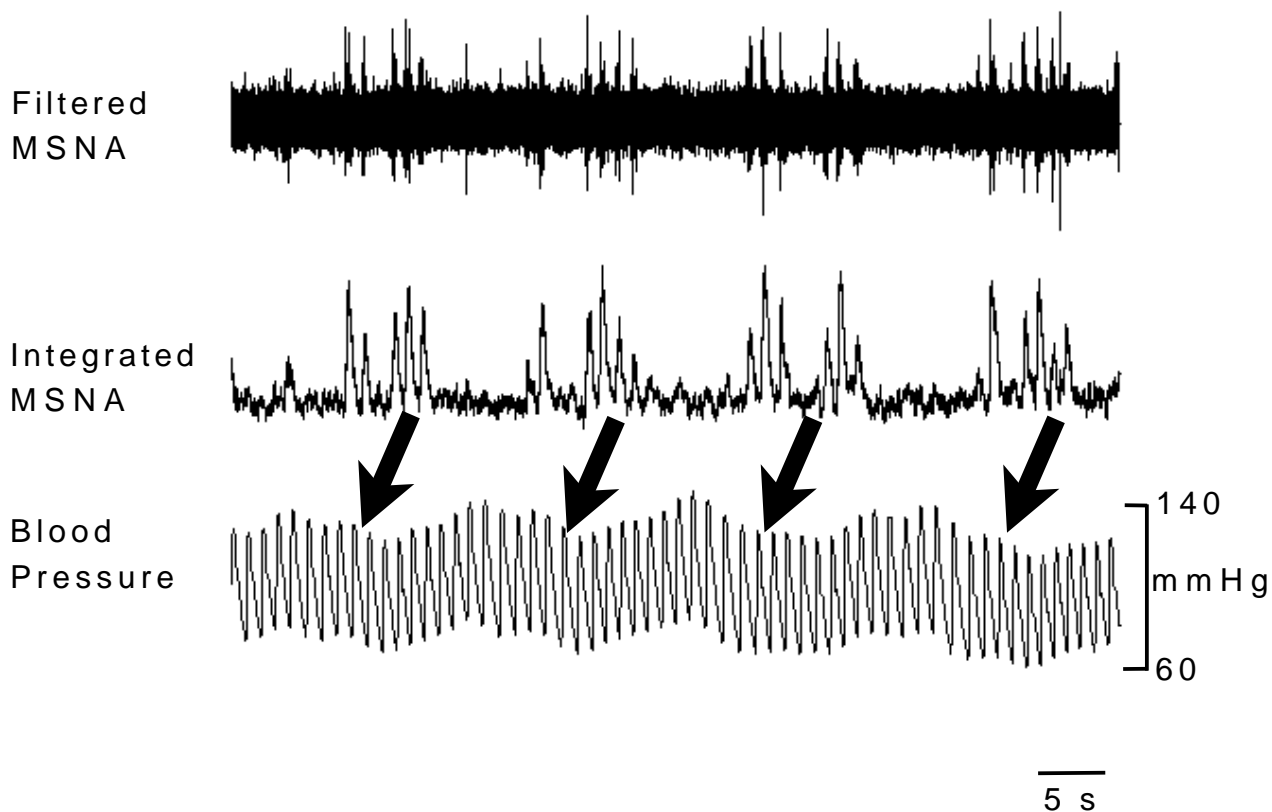


Figure 1.7: The relationship between variations in blood pressure and MSNA. This representative example shows that more bursts occurring during decreasing than during increasing blood pressure. Arrows indicate sequences of bursts and corresponding blood pressure beats.

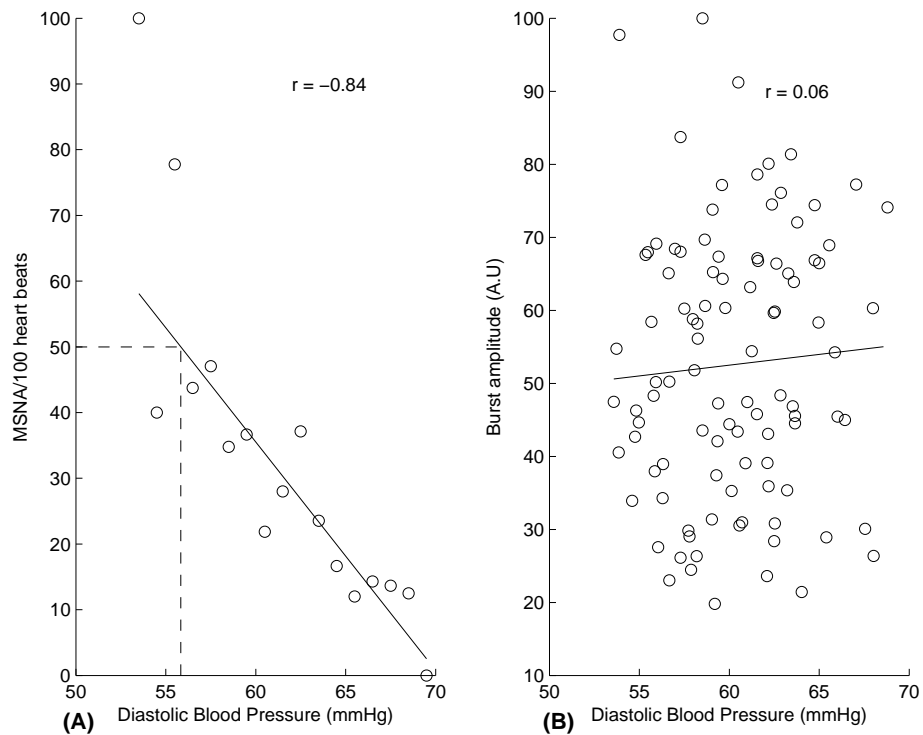


Figure 1.8: The baroreflex threshold and sensitivity diagrams. (A) Example of a baroreflex threshold diagram from a female participant. The individual circles represent the mean diastolic blood pressure in each 1-mmHg blood pressure bin. For each of these bins the percentage of heart beats associated with a burst is plotted against the mean of the pressure in that bin. The dotted line represents the diastolic blood pressure associated with 50% bursts (T_{50}). In this particular female the (T_{50}) is 55.83 mmHg. (B) Example of a baroreflex sensitivity diagram, the amplitude of individual bursts is plotted against the corresponding diastolic blood pressure for that burst. Burst amplitudes are normalized (100 means the maximum burst amplitude).

1.3 Drawbacks and limitations of the integrated burst analysis

Although the information extracted from the integrated MSNA signal is useful and important, this traditional analysis (i.e., integrating the raw MSNA signal) removes important information regarding action potential content of the raw MSNA signal. The raw MSNA signal contains spikes (action potentials) that represent the discharge pattern of individual neurons within the recording field of the microelectrode tip. Detail of coding patterns in the action potentials should, in theory, provide information about recruitment strategies used by the central nervous system to achieve the spontaneous activity and stress responses. For instance, Wallin et al [21], in the absence of action potential analysis, hypothesized the presence of multiple populations of post-ganglionic axons; however, to test this hypothesis, it is necessary to assess action potential content of the multi-fibre recording for variations in the number of active action potentials, morphology and timing.

Additionally, in some certain physiological conditions such as very low pulse pressures or intense stress, integrating the raw MSNA signal is not able to provide a good integrated MSNA signal for traditional analysis. Fig. 1.9 demonstrates this point where the integrator produces burst fusing pattern during severe apnoea. Such fusions represent a challenge to traditional burst detection and quantification and shows the need for alternative method for studying the raw MSNA signal.

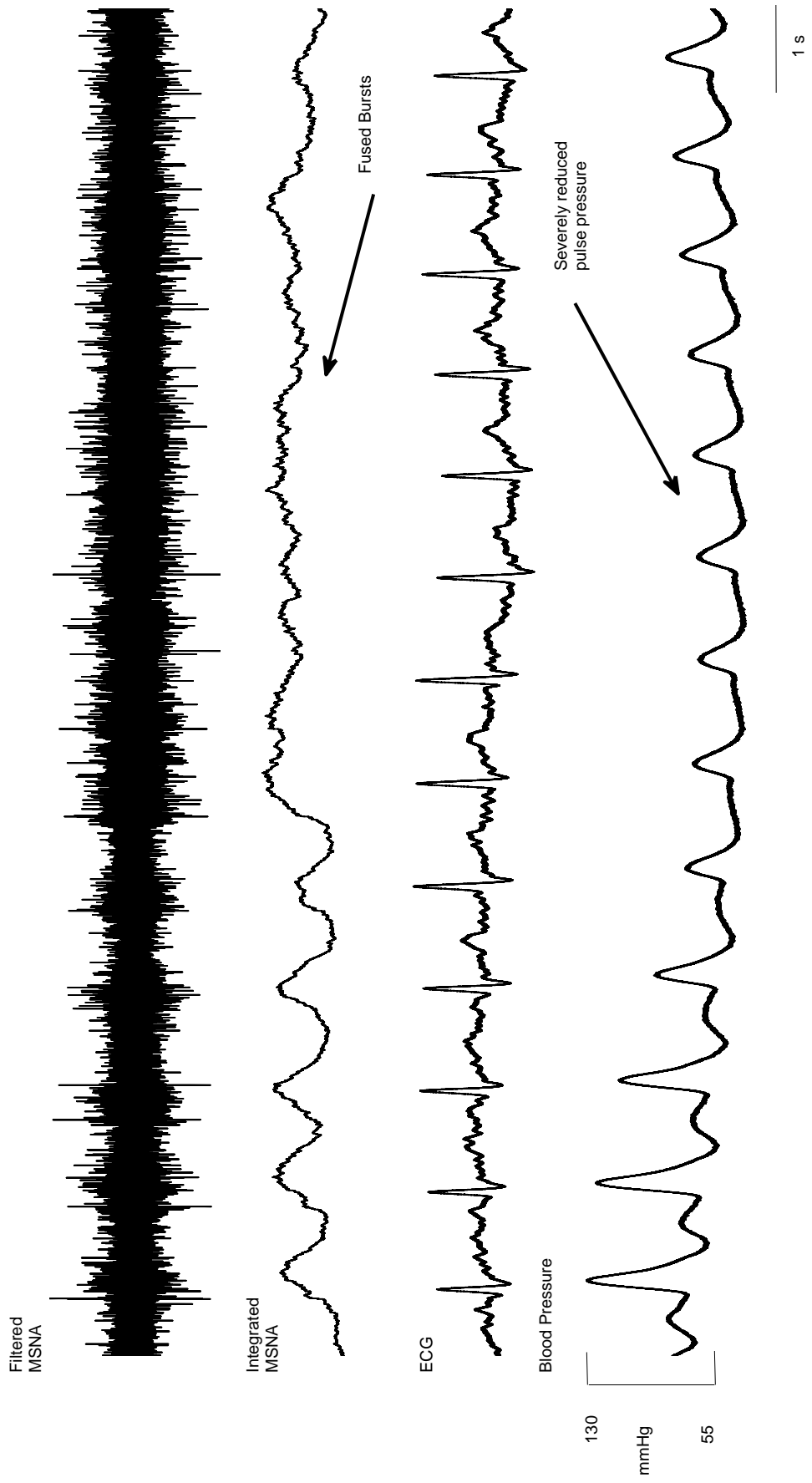


Figure 1.9: The fused burst patterns. A representative example of fused bursts of muscle sympathetic nerve activity.

1.4 Spike Detection in human MSNA signal

An alternative method for analyzing the MSNA signals is to develop a method to separate the action potentials from the background noise in the raw MSNA signal and to study their morphology, latency (i.e., conduction velocity) and their relationship with the sympathetic bursts. Fig. 1.10 shows a general idea of the spike detection concept in human MSNA recordings. Since all studies of action potential content of the extracellular recordings of the MSNA start from the shape and location of individual action potentials within sympathetic bursts, it is necessary to precisely detect and localize the occurrence of action potential within sympathetic bursts. Action potential detection in human MSNA signal is challenging because the spikes in extracellular sympathetic recordings are contaminated with high level of background or environmental noises.

Spike detection in noisy extracellular recordings is a classical problem because of its practical importance to experimental neuroscience. There are different algorithms for spike detection and classification from multi-unit but non-sympathetic neural recordings [see 22–25]. The most common spike detection tool is the time-amplitude window discriminator techniques [26–29] where a threshold can be set automatically (e.g., as a multiple of the estimated noise standard deviation). Signals that pass the defined threshold are identified as action potential. However, the threshold is a conservative choice that is not able to capture low amplitude spikes in the MSNA signal and it produces considerable false positive alarms. Other detection methods include power or energy detection [30–32] where the instantaneous power of the signal is calculated using a moving window and compared with a threshold estimated from the standard deviation of the noise power. In general, the performance of the power detector methods are better than that of amplitude thresholding but their performance decreases during low signal-to-noise ratio (SNR) signals.

The other techniques are automated wavelet-based methods that have been implemented to detect and classify neural recordings [33–38]. The general idea of wavelet-based spike detection is that a nerve signal containing a train of action potentials but contaminated with noise

is decomposed by the wavelet transform into a set of time-scale and time-translated version of a particular template called “mother wavelet” to provide a resemblance index (i.e., wavelet coefficient) between the signal of interest (e.g., action potentials) and the mother wavelet. If the index is “large” the resemblance is strong and if the index is small, the resemblance is weak . Therefore, the mother wavelet should be similar to the signal under interrogation. For detection purposes, the wavelet coefficients related to action potentials and noise portions can be separated using wavelet de-noising techniques [39, 40].

Based on our knowledge, there are only three methods available that have been applied for action potential detection from raw MSNA signal. Two of these methods are wavelet-based techniques [41, 42]. Both of these methods have shown remarkably better performance than the time-amplitude discriminator and have been successful for action potential detection. The other spike detection approach that has been applied to sympathetic recordings [43] uses a mixture probabilistic model for identifying spikes. Although this method provides good spike counting accuracy, it does not provide any information about spike morphology and it is computationally expensive. Because of the non-stationary nature of the human MSNA signal, the wavelet-based methods can be a proper choice to handle this problem as it has been used previously [41, 42].

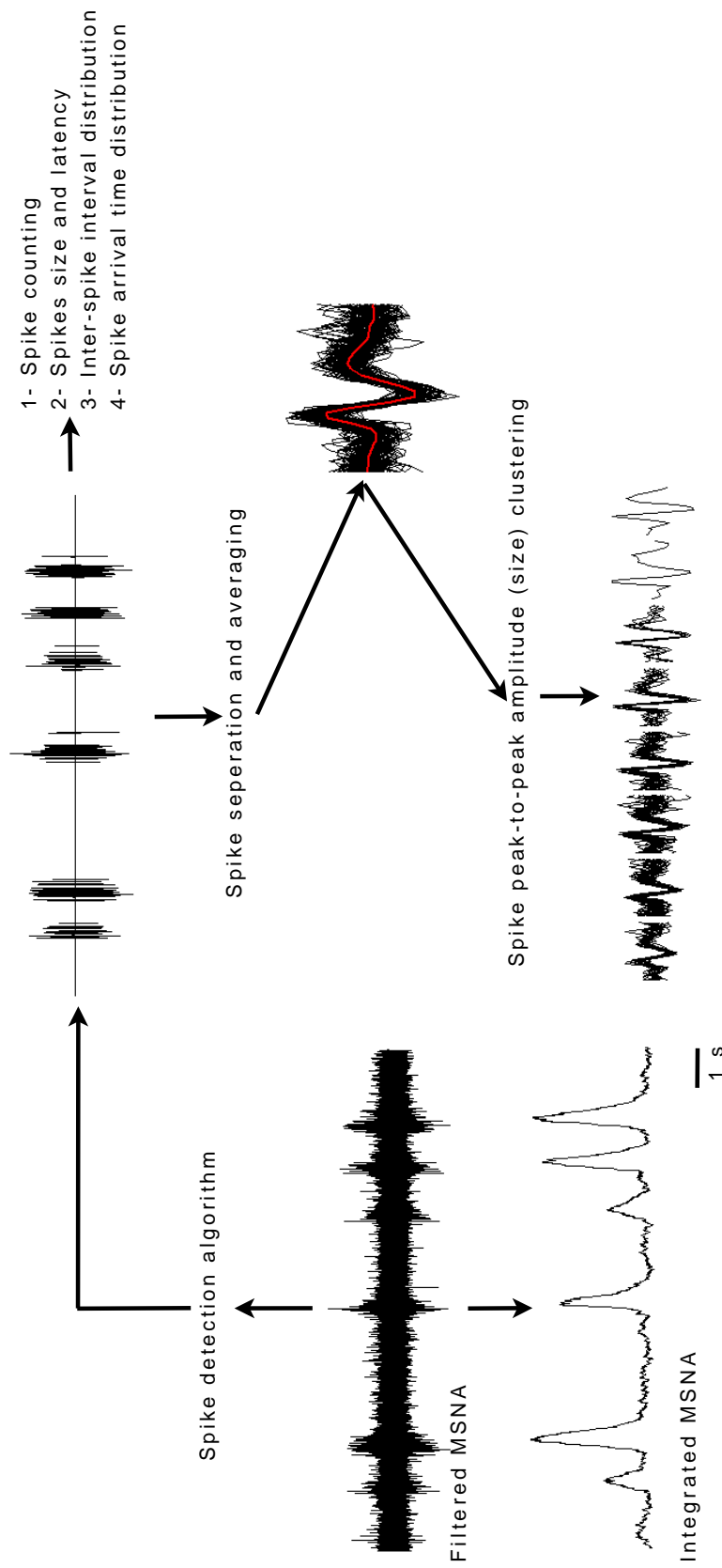


Figure 1.10: General concept of spike detection and classification.

1.5 Objective and Outline of this thesis

There are two main objectives of the research presented in this thesis. The first purpose was to develop a reliable action potential detection and classification method to accurately and robustly detect and localize the occurrence of individual action potentials in extracellular sympathetic recordings obtained from humans. The second purpose was to apply this new action potential detection method to real sympathetic signals and to directly study recruitment patterns of multi-fiber post-ganglionic sympathetic neural recordings during baseline and orthostatic stress of lower body negative pressure (LBNP). The organization of the thesis and a brief summary of each chapter is as follows:

Chapter 2 provides a general background of wavelet analysis of sympathetic neural signals. The application and performance of the discrete wavelet transform (DWT) and stationary wavelet transform (SWT) for detection of spikes in human raw MSNA signal is reviewed in this chapter. A method for finding an actual mean action potential template after bandpass filtering and before amplification of the raw MSNA signal is presented in this chapter. Also, this chapter demonstrates the classification of sympathetic action potentials based on their morphology.

Chapter 3 proposes a novel method for improving the performance of the previous wavelet-based techniques for detecting spikes in sympathetic recordings. The new method is based on the design of a mother wavelet that is matched to an actual mean action potential template extracted from a real raw MSNA signal. To detect action potentials, the new matched wavelet is applied to the MSNA signal using a continuous wavelet transform following a thresholding procedure and finding of a local maxima that indicates the location of action potentials. The performance of the proposed method versus two previous wavelet-based approaches is evaluated using 1) real MSNA recorded from seven healthy participants during LBNP protocol and, 2) simulated MSNA. To this end this chapter also presents a new method to model a simulated MSNA signal based on statistical properties of the MSNA signal derived from the detection method provided here. The problem of action potential summation in multi-fiber recordings is also discussed in this chapter and the performance of the new method in detecting overlapped

spikes is evaluated.

Chapter 4 employs the novel action potential detection technique presented in chapter 3 to study the relationship between the recruitment of sympathetic action potentials and the size of integrated sympathetic bursts in human muscle sympathetic nerve activity. Due to the lack of action potential content and analysis of sympathetic recordings little is known about the recruitment pattern of sympathetic neurons during baseline and different physiological conditions. This chapter aims to examine recruitment characteristics of post-ganglionic sympathetic neurons to test the hypothesis that sympathetic neurons follow a size principle in their recruitment patterns.

Chapter 5 summarizes this thesis with some concluding remarks and presentation of possible work in the future.

1.6 Contributions of the author

Chapter 2 was presented at

- **A. Salmanpour**, L. J. Brown and J. K. Shoemaker, “Detection and Classification of Raw Action Potential Patterns in Human Muscle Sympathetic Nerve Activity,” *30th Annual International conference of the IEEE Engineering in Medicine and Biology Society (IEEE EMBS)*, Vancouver, BC, Canada, pp. 2928-2931, 2008.

and

- **A. Salmanpour**, L. J. Brown and J. K. Shoemaker, “Performance Analysis of Stationary and Discrete Wavelet Transform for Action Potential Detection from Sympathetic Nerve Recordings in Humans,” *30th Annual International conference of the IEEE Engineering in Medicine and Biology Society (IEEE EMBS)*, Vancouver, BC, Canada, pp. 2928-2931, 2008.

Chapter 3 was published in *Journal of Neuroscience Methods*

- **A. Salmanpour**, L. J. Brown, J. K. Shoemaker, “Spike detection in human muscle sympathetic nerve activity using a matched wavelet approach,” *Journal of Neuroscience Methods*, vol. 193, pp. 343-355, 2010.

It was also presented at

- **A. Salmanpour**, L. J. Brown and J. K. Shoemaker, “Detection of Single Action Potential in Multi-unit Postganglionic Sympathetic Nerve Recordings in Humans: A Matched Wavelet Approach,” *IEEE International Conference on Acoustic, Speech, and Signal Processing (IEEE ICASSP)*, Dallas, Texas, USA, pp. 554-557, 2010.

Chapter 4 was submitted to *Journal of Neurophysiology*

- **A. Salmanpour**, L. J. Brown, C. D. Steinback, C. W. Usselman, R. Goswami and J. K. Shoemaker, “Relationship between size and latency of action potentials in human muscle sympathetic nerve activity,” *Journal of Neurophysiology*

In addition to the scientific work listed above, the author has contributed to the following papers that are connected to this thesis in various degrees. The first two papers mentioned below are the direct result of using and applying the spike detection software developed here to study action potential content in different physiological conditions:

- CD Steinback, **A. Salmanpour**, T. Breskovic, Z. Dujic, and J. K. Shoemaker, “Sympathetic neural activation: an ordered affair,” *Journal of Physiology*, vol. 588, pp. 4825-4836, 2010.
- T Breskovic, CD Steinback, **A Salmanpour**, Z Dujic, and JK Shoemaker, “Recruitment pattern of sympathetic neurons during functional residual capacity and total lung capacity apnea in breath hold divers and controls”, submitted to *Experimental Physiology*.
- M Zamir, R Goswami, L Liu, **A Salmanpour** and JK Shoemaker, “Myogenic activity in autoregulation during low frequency oscillations”, *Auton Neurosci* (2010), doi:10.1016/j.autneu.2010.07.029.

References

- [1] B. G. Wallin, W. Delius, and K. E. Hagbarth, "Sympathetic activity in peripheral nerves of normo- and hypertensive subjects," *Clin. Sci. Mol. Med. Suppl*, vol. 45, pp. 127-30, 1973.
- [2] B. G. Wallin, W. Delius, and K. E. Hagbarth, "Comparison of sympathetic nerve activity in normotensive and hypertensive subjects," *Circ. Res. Suppl*, vol. 33, pp. 9-21, 1973.
- [3] B. G. Wallin and G. Sundlof, "A quantitative study of muscle nerve sympathetic activity in resting normotensive and hypertensive subjects," *Hypertension*, vol. 1, pp. 67-77, 1979.
- [4] A. Malliani and M. Pagani, "The role of the sympathetic nervous system in congestive heart failure," *Eur Heart J*, vol. 4, pp. 49-54, 1983.
- [5] G. Grassi, G. Seravalle, B. M. Cattaneo, G. B. Bolla, A. Lanfranchi, M. Colombo, C. Giannattasio, A. Brunani, F. Cavagnini, and G. Mancia, "Sympathetic activation in obese normotensive subjects," *Hypertension*, vol. 25, pp. 560-563, 1995.
- [6] G. Grassi, B. M. Cattaneo, G. Seravalle, M. Colombo, F. Cavagnini, and G. Mancia, "Obesity and the sympathetic nervous system," *Blood Press Suppl*, vol. 1, pp. 43-46, 1996.
- [7] K. E. Hagbarth and A. B. Vallbo, "Pulse and respiratory grouping of sympathetic impulses in human muscle nerves," *Acta physiol scand*, vol. 74, pp. 96-108, 1968.
- [8] W. Delius, K. E. Hagbarth, A. Hongell, and B. G. Wallin, "General characteristics of sympathetic activity in human muscle nerves," *Acta Physiol Scand*, vol. 84, pp. 65-81, 1972.
- [9] G. Sundlof and B. G. Wallin, "Human muscle nerve sympathetic activity at rest, relationship to blood pressure and age," *J Physiol* vol. 274, pp. 621-637, 1978.

- [10] R. M. Berne and M. N. Levy, *Physiology*. St. Louis, MO: Mosby, 1998.
- [11] J. Fagius and B. G. Wallin, "Sympathetic reflex latencies and conduction velocities in normal man," *J Neurol Sci* vol. 47, pp. 433-448, 1980.
- [12] B. G. Wallin, "Sympathetic Microneurography," in *Primer on the Autonomic Nervous System*, second ed. Elsevier:Oxford, pp. 224-227, 2004.
- [13] V. G. Macefield, M. Elam, B. G. Wallin, "Firing properties of single postganglionic sympathetic neurones recorded in awake human subjects," *Auton Neurosci-Basic*, vol. 95, pp. 146-159, 2002.
- [14] V. G. Macefield and B. G. Wallin, "Firing properties of single vasoconstrictor neurones in human subjects with high levels of muscle sympathetic activity," *J Physiol*, vol. 516, pp. 293-301, 1999.
- [15] G. Sundolf and B. G. Wallin. "The variability of muscle nerve sympathetic activity in resting recumbent man," *J Physiol*, vol. 272, pp. 383-397, 1977.
- [16] B. G. Wallin, R. G. Victor and A. L. Mark. "Sympathetic outflow to resting muscles during static handgrip and postcontraction muscle ischemia," *Am. J. Physiol*, vol. 256, pp. H105-H110, 1989.
- [17] Y. B. Sverrisdottir, B. Rundqvist, M. Elam. "Relative burst amplitude in human muscle sympathetic nerve activity: a sensitive indicator of altered sympathetic traffic," *Clin. Auton. Res*, vol. 8, pp. 95-100, 1998.
- [18] Y. B. Sverrisdottir, B. Rundqvist, G. Johannsson, M. Elam. "Sympathetic neural burst amplitude distribution: a more specific indicator of sympatho-excitation in human heart failure," *Circulation*, vol. 102, pp. 2076-2081, 2000.
- [19] P. Kienbaum, T. Karlsson, Y. B. Sverrisdottir, M. Elam, B. G. Wallin, "Two sites for

- modulation of human sympathetic activity by arterial baroreceptors?," *J Physiol*, vol. 531, pp. 861-869, 2001.
- [20] E. C. Hart, M. J. Joyner, B. G. Wallin, T. Karlsson, T. B. Curry and N. Charkoudian, "Baroreflex control of muscle sympathetic nerve activity: a nonpharmacological measure of baroreflex sensitivity," *Am J Physiol Heart Circ Physiol*, vol. 298, pp. H816-H822, 2010.
- [21] B. G. Wallin, D. Burke and S. Gandevia, "Coupling between variations in strength and baroreflex latency of sympathetic discharges in human muscle nerves," *J Physiol*, vol. 474, pp. 331-338, 1994.
- [22] M. Abeles, M. H. Goldstein, "Multispikes train analysis," *Proceedings of The IEEE*, vol. 65, pp. 762-773, 1977.
- [23] X. Yang, S. A. Shamma, "A totally automated system for the detection and classification of neural spikes," *IEEE Trans Biomed Eng* vol. 35, pp. 806-816, 1988.
- [24] A. F. Atiya, "Recognition of multiunit neural signals," *IEEE Trans Biomed Eng*, vol. 39, pp. 723-729, 1992.
- [25] M. Lewicki. "A review of methods for spike sorting: the detection and classification of neural action potentials." *Comput Neural Syst*, vol. 9, pp. R53-R78, 1998.
- [26] M. J. Bak and E. M. Schmidt, "An improved time-amplitude window discriminator," *IEEE Trans. Biomed. Eng*, vol. 24, pp. 486-489, 1977.
- [27] W. Wiemer, D. Kaack, P. Kezdi, and H. Klatt, "Peak discrimination as a method for quantitative evaluation of neural activity by computer," *Med. Biol. Eng.*, vol. 13, pp. 337-357, 1975.
- [28] C. Pouzat, O. Mazor, G. Laurent, "Using noise signature to optimize spike sorting and to assess neuronal classification quality," *J Neurosci Meth* vol. 122, pp. 43-57, 2002.

- [29] T. Borghi, R. Gusmeroli, A.S. Spinelli, G. Baranauskas, "A simple method for efficient spike detection in multiunit recordings," *J Neurosci Meth* vol. 163, pp. 176-180, 2007.
- [30] K. D. Harris, D. A. Henze, J. Csicsvari, H. Hirase, and G. Buzsaki, "Accuracy of tetrode spike separation as determined by simultaneous intracellular and extracellular measurements," *J. Neurophysiol.*, vol. 84, pp. 4014-14, 2000.
- [31] I. N. Bankman, K. O. Johnson, and W. Schneider, "Optimal detection, classification, and superposition resolution in neural waveform recordings," *IEEE Trans. Biomed. Eng.*, vol. 40, pp. 836-841, 1993.
- [32] K. H. Kim and S. J. Kim, "Neural spike sorting under nearly 0-dB signal-to-noise ratio using nonlinear energy operator and artificial neural network classifier," *IEEE Trans. Biomed. Eng.*, vol. 47, pp. 1406-1411, 2000.
- [33] J. C. Letelier, P. P. Weber. "Spike sorting based on discrete wavelet transform coefficients," *J Neurosci Methods*, vol. 101, pp. 93-106, 2000.
- [34] K. H. Kim, S. J. Kim, "A wavelet-based method for action potential detection from extracellular neural signal recording with low signal-to-noise ratio," *IEEE Trans. Biomed. Eng.*, vol. 50, pp. 999-1011, 2003.
- [35] H. Nakatani, T. Watanabe, N. Hoshimiya, "Detection of nerve action potentials under low signal-to-noise ratio condition," *IEEE Trans. Biomed. Eng.* vol. 48, pp. 845-849, 2001.
- [36] K. G. Oweiss, D. J. Anderson, "Spike sorting: a novel shift and amplitude invariant technique," *Neurocomput*, vol. 44-46, pp. 1133-9, 2002.
- [37] Z. Nenadic and J.W. Burdick, "Spike Detection Using the Continuous Wavelet Transform," *IEEE Trans Biomed Eng*, vol. 52, pp. 74-87, 2005.
- [38] L. Citi, J. Carpaneto, K. Yoshida, K. P. Hoffmann, K. P. Koch, P. Dario, "On the use

of wavelet denoising and spike sorting techniques to process electroneurographic signals recorded using intraneural electrodes,” *J Neurosci Methods*, vol. 172, pp. 294-302, 2008.

- [39] D. L. Donoho DL, “Ideal spatial adaptation by wavelet shrinkage,” *Biometrika*, vol. 81, pp. 425-455, 1994.
- [40] D. L. Donoho, “De-noising by soft-thresholding,” *IEEE Trans Inf Theory*, vol. 41, pp. 613-627, 1995.
- [41] A. Diedrich, W. Charoensuk, R. J. Brychta, A. C. Ertl and R. Shiavi, “Analysis of raw microneurographic recordings based on wavelet de-noising technique and classification algorithm: Wavelet analysis in microneurography,” *IEEE Trans. Biomed. Eng.*, vol. 50, pp. 41-50, 2003.
- [42] R. J. Brychta, R. Shiavi, D. Robertson, A. Diedrich, “Spike detection in human muscle sympathetic nerve activity using the kurtosis of stationary wavelet transform coefficients,” *J Neurosci Meth* vol. 160, pp. 359-367, 2007.
- [43] O. T. Can, J. A. Taylor, A. Ler, M. A. Cohen, “Detection of Multifiber Neuronal Firings: A Mixture Separation Model Applied to Sympathetic Recordings,” *IEEE Trans Biomed Eng.*, vol. 56, pp. 147-158, 2009.

Chapter 2

Spike detection using stationary and discrete wavelet transform from sympathetic nerve recordings in humans

2.1 Introduction

Estimation of autonomic responses to stress in humans is most directly assessed through microneurographic measures of peripheral sympathetic nerve activity [1]. Using this technique, multi-fibre recordings of sympathetic nerve activity can be assessed from a superficial nerve using methods developed by Hagbarth and Vallbo [2] and used frequently in our laboratory [3–6]. Historically, previous studies in microneurographic recordings from humans has emphasized the summation of the bursts per unit time either with or without inclusion of the size or area of each burst in the integrated signal. This approach provides an estimate of total sympathetic outflow and its bursty pattern. However, there is much signal content lost in the integration process. As shown in Fig. 2.2, the raw signal contains spikes (action potentials) that, in theory, represent the discharge pattern of individual neurons within the recording field of the microelectrode tip. For two main reasons our laboratory is pursuing the analysis and quantification of

this raw sympathetic neurogram. First, we are interested in the relationship between discharge pattern and neurotransmitter release. Sympathetic neurons directed to the vasculature in skeletal muscle release multiple vasoconstricting neurotransmitters, namely, ATP, norepinephrine and neuropeptide Y. It is proposed that it is the frequency content of the neural discharge that determines neurotransmitter release patterns [7]. While contentious [8], this hypothesis will require much closer attention to the discharge patterns of the original nerve signal. As the number of neurons contributing to the efferent discharge will vary with each burst, it is necessary to examine the neural content of each burst. Whereas some information can be gleaned from the discharge patterns of single neurons followed over time [9], the examination of neuronal populations and recruitment patterns requires a different approach of separating signal and noise components, exposing the multiple action potentials in real time.

The second reason for our investigation is an interest in the loss of information that occurs in the integration process due to an inherent low signal to noise aspect of the signal. Detail of coding patterns in the single action potentials should, in theory, provide information about recruitment strategies used by the central nervous system to achieve the spontaneous activity and stress responses. However, this high frequency content of the signal is lost in the integrated signal. Additionally, the low signal-to-noise aspect of this signal combines with the sensitivity settings of the integrator to lose some action potential data. Fig. 2.2 demonstrates this point where the integrated signal fails to expose neural activity that is present in the raw signal. The integration process incorporates both signal and noise in the neurogram and can, on some occasions, obscure burst activity. Only by adequate de-noising of the raw signal can such bursts be detected.

As it is apparent from Fig. 2.2 the amplified and filtered MSNA are contaminated with high environmental and bioelectric background noise. Therefore, one of the primary steps in action potential detection from the filtered MSNA signal is removing this background noise. The action potentials then can be identified using a simple peak detection scheme from the de-noised signal. A common noise removal approach involves applying signal averaging to the

MSNA signal [3]. In theory this approach can reduce background noise by \sqrt{n} , but temporal sensitivity is lost in the process. Recently, wavelet-based de-noising techniques have been applied to reduce noise in the filtered muscle sympathetic nerve activity [12–15]. However, improvements to the wavelet-based de-noising techniques are required as the signal and noise share similar characteristics, minimizing the effectiveness of the approach. Wavelet transform represents a signal as a weighted sum of temporally scaled and shifted versions of a “mother” wavelet function. If the signal is deterministic, it will contribute significantly only to a few coefficients describing the wavelet representation of the signal, while the noise will contribute uniformly to all coefficients. Ideally, the mother wavelet function exactly matches the neuronal signal so that a single coefficient describes the signal.

In this paper, we compare the performance of stationary wavelet transform (SWT) and discrete wavelet transform (DWT) in detecting filtered action potentials in MSNA recordings. Two thresholding and noise estimation techniques will be examined based on the method developed by Donoho [22] and modified by Diedrich [12]. We also propose a detection method for finding a typical action potential waveform; moreover, the result of action potential shape classification is explained.

This paper is organized as follows: Section 2 reviews wavelet-based de-noising techniques used in the experiments, section 3 discusses the method for recording and detecting action potentials and the method for generating simulated MSNA, section 4 shows comparison results between SWT and DWT and discusses the achieved results based on the proposed method, and section 5 concludes the paper.

2.2 Background

2.2.1 Discrete Wavelet Transform (DWT)

A fast wavelet decomposition and reconstruction algorithm was developed by Mallat [16]. The Mallat algorithm for discrete wavelet transform (DWT) consists a set of quadrature mirror

filters (QMF), h_0 (low-pass filter) and h_1 (high-pass filter). The filters, h_0 and h_1 , are related to the mother wavelet, $\psi(x)$, and the scaling function, $\phi(x)$, in the time domain as follows:

$$\begin{aligned}\Phi(x) &= 2 \sum_{k=-\infty}^{k=\infty} h_0(k)\Phi(2x - k) \\ \Psi(x) &= 2 \sum_{k=-\infty}^{k=\infty} h_1(k)\Phi(2x - k)\end{aligned}\tag{2.1}$$

In the frequency domain (2.1) becomes

$$\begin{aligned}\Phi(\omega) &= H_0\left(\frac{\omega}{2}\right)\Phi\left(\frac{\omega}{2}\right) \\ \Psi(\omega) &= H_1\left(\frac{\omega}{2}\right)\Phi\left(\frac{\omega}{2}\right)\end{aligned}\tag{2.2}$$

In this thesis, we use ‘‘Symlet 7’’ as the mother wavelet. Fig. 2.1 (A-F) shows the ‘‘Symlet 7’’ wavelet function, the corresponding scaling function, decomposition and reconstruction high-pass and low-pass filters (Matlab, the Mathworks, Inc), respectively.

The DWT decomposition process can be computed by (2.3) and (2.4).

$$cA_{j+1}^{DWT}(k) = \sum_n h_0(n - 2k)cA_j^{DWT}(n)\tag{2.3}$$

$$cD_{j+1}^{DWT}(k) = \sum_n h_1(n - 2k)cD_j^{DWT}(n)\tag{2.4}$$

Briefly, the DWT consists of $\log_2(N)$ stages at most to decompose a signal f of length N . Starting from $cA_0^{DWT} = f$, the first step produces two sets of coefficients: approximation coefficients cA_1^{DWT} , and detail coefficients cD_1^{DWT} . These coefficients are computed by convolving f with the low-pass filter (h_0) for approximation, and with the high-pass filter (h_1) for detail, followed by down-sampling by factor 2. The next step splits the approximation coefficients cA_1^{DWT} in two parts using the same scheme, replacing f by cA_1^{DWT} and producing cA_2^{DWT} and cD_2^{DWT} , and so on. Note that the DWT algorithm segments the frequency content of the cA_j^{DWT} approximately in half in each level of decomposition. The inverse DWT (IDWT) reconstructs cA_j^{DWT} from cA_{j+1}^{DWT} and cD_{j+1}^{DWT} using inverting the decomposition step by inserting zeros (Up-sampling by factor two) and convolving the results with the appropriate reconstruction filters,

$f_0 = h_0(-n)$ and $f_1 = h_1(-n)$, and summing. The IDWT is computed by (2.5)

$$cA_j^{DWT}(k) = \sum_n h_0(k - 2n)cA_{j+1}^{DWT}(n) + \sum_n h_1(k - 2n)cD_{j+1}^{DWT}(n) \quad (2.5)$$

The original signal (f) can be recovered by iteratively continuing the IDWT algorithm.

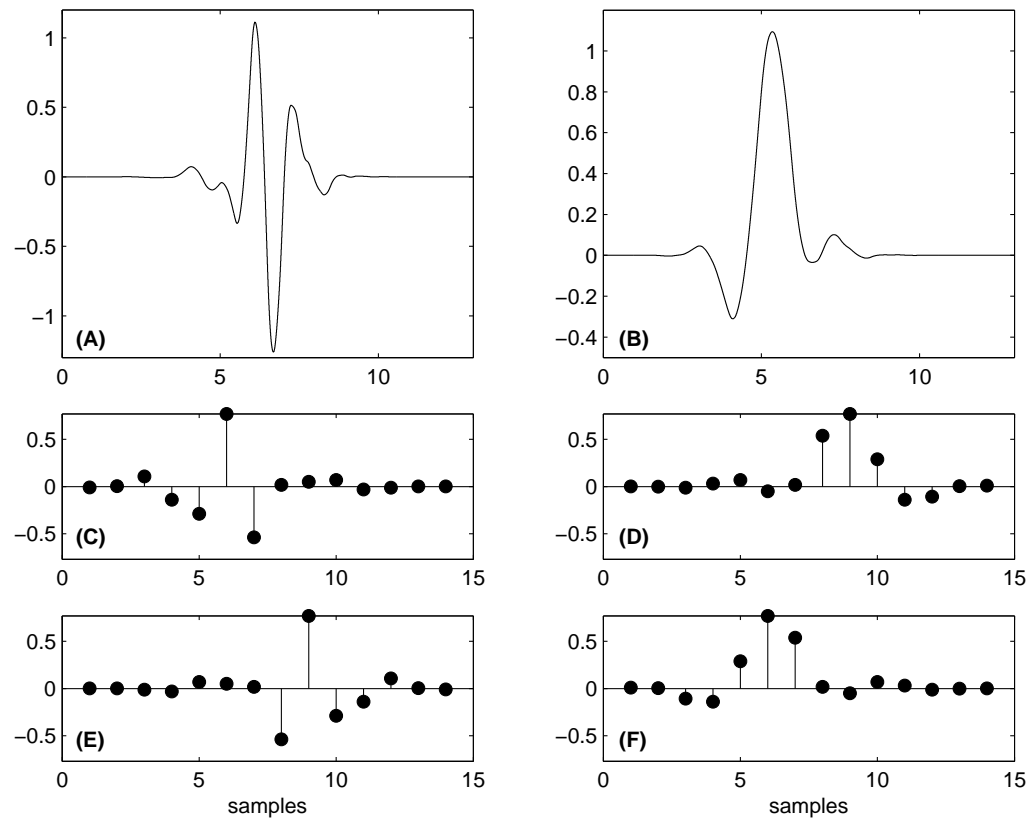


Figure 2.1: (A) The Symlet 7 wavelet function. (B) The scaling function corresponding to Symlet 7. (C) Decomposition high-pass filter h_1 . (D) Decomposition low-pass filter h_0 . (E) Reconstruction high-pass filter f_1 . (F) Reconstruction high-pass filter f_0 .

2.2.2 Stationary or Undecimated Wavelet Transform (SWT)

One of the major problems of the DWT is that this transform is not time-invariant which means that shifts in the input signal will produce different set of the DWT coefficients. In order to resolve this problem, the Stationary Wavelet Transform (SWT) has been introduced [17] which is time-invariant. The SWT can be obtained by omitting the decimation and up-sampling the low-pass and high-pass filters for the next level of processing from the Mallat algorithm [16, 17]. The SWT decomposition process can be computed by (2.6) and (2.7)

$$cA_{j+1}^{SWT}(k) = \sum_n h_{0j}(n-k)cA_j^{SWT}(n) \quad (2.6)$$

$$cD_{j+1}^{SWT}(k) = \sum_n h_{1j}(n-k)cA_j^{SWT}(n) \quad (2.7)$$

Note that the approximation and detail coefficients at level j are both of size N , the signal length, and a set of level dependent low-pass h_{0j} and high-pass h_{1j} filters, which simply are h_0 and h_1 filters with up-sampling by two in each level of decomposition, are used in the SWT algorithm. The cA_j^{SWT} coefficients can be recovered from cA_{j+1}^{SWT} and cD_{j+1}^{SWT} by convolving each approximated and detailed coefficients with a set of level dependent reconstruction filters. This process is called inverse SWT (ISWT) and is shown as follows:

$$cA_j^{SWT}(k) = \sum_n h_{0j}(k-n)cA_{j+1}^{SWT}(n) + \sum_n h_{1j}(k-n)cD_{j+1}^{SWT}(n) \quad (2.8)$$

The main drawbacks of the SWT algorithm is that this algorithm is computationally expensive. For further discussion about the differences between DWT and SWT please refer to [17–20].

2.2.3 Wavelet-Denoising: Thresholding and Noise Estimation

Wavelet Denoising includes thresholding of the detailed coefficients computed by DWT or SWT. A level dependent noise estimation threshold, T_j has usually been used in the case of colored noise and can be computed based on the technique developed by Donoho [21, 22] as follows:

$$T_j^S = \sigma_j \sqrt{2 \log_e(N)} \quad (2.9)$$

Equation (2.9) is called regular or standard thresholding method. In (2.9) N is the length of the input signal and σ_j is the standard deviation of the colored gaussian noise. σ_j can be calculated for each level of decomposition as follows:

$$\sigma_j = \frac{\text{median}(|cD_j - \overline{cD_j}|)}{0.6745} \quad (2.10)$$

where 0.6745 is the 75th percentile of the standard normal distribution [21, 22] and cD_j are the detail coefficients for level j computed by SWT or DWT. The detail coefficients are thresholded by a hard thresholding procedure as follows

$$cD'_j = \begin{cases} cD_j & \text{if } |cD_j| > T_j^S \\ 0 & \text{if } |cD_j| \leq T_j^S \end{cases} \quad (2.11)$$

Finally, IDWT or ISWT uses the thresholded detail coefficients, cD'_j , with corresponding approximated coefficients, cA_j , to build a denoised version of the input signal.

2.3 Materials and Methods

2.3.1 Data acquisition and recording conditions

MSNA was recorded from the peroneal nerve of three healthy subjects (two males, one female, 27 ± 2 yrs). Briefly, for peroneal nerve recordings, a 200 μm diameter, 35 mm long tungsten

microelectrode tapering to an uninsulated 1 to 5 μm tip was inserted transcutaneously into the peroneal nerve just posterior to the fibular head. A reference electrode was positioned subcutaneously 1-3 cm from the recording site. Neurograms were measured with a nerve traffic analysis system (662C-3, Bioengineering of University of Iowa, Iowa City, IA). Fig. 2.3 illustrates of the nerve traffic analysis system (662C-2). The neural signal was preamplified with a gain of 1000 and further amplified with a gain of 75. This neuronal activity was then band-pass filtered (bandwidth of 700-2,000 Hz) and finally filtered MSNA was rectified and integrated (see Fig. 2.2). Integration is accomplished with a leaky integrator typically set with a 0.1 s time constant. All signals were digitized with a data acquisition system (Powerlab software, AD Instruments Inc.) at a sampling rate that varied from 100 Hz for the rectified and integrated neurogram to 10 kHz for the amplified and filtered neurogram.

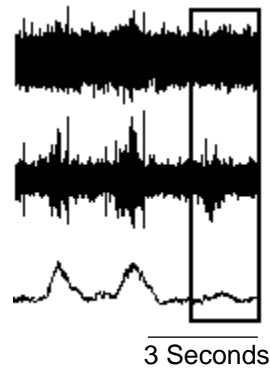


Figure 2.2: The raw and integrated MSNA signals. Original data of the amplified neurogram (top panel), the filtered neurogram (middle panel) and the integrated neurogram (bottom panel). Area inside rectangle shows an obvious burst of action potentials in the filtered neurogram (middle panel) that is lost during integration (bottom panel).

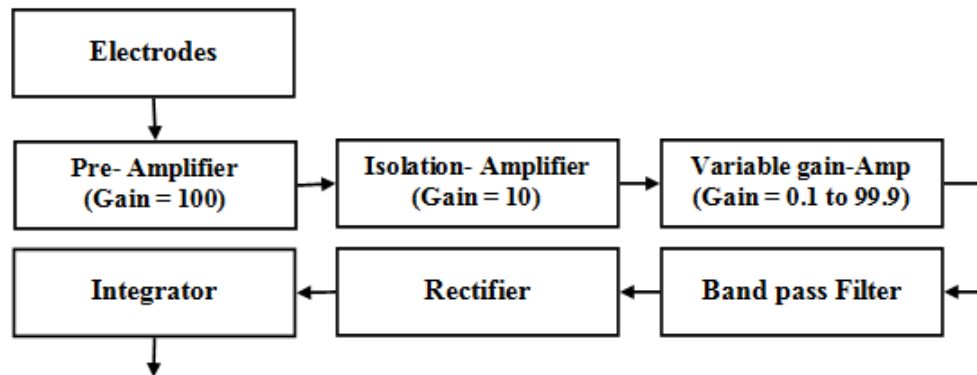


Figure 2.3: The block diagram of the Iowa nerve traffic analysis system 662C-3.

2.3.2 Proposed method for action potential detection

The proposed method for detection of averaged action potential from filtered MSNA involves a three-step process: 1) Wavelet-Denoising using stationary wavelet transform (SWT), 2) Peak detection using a thresholding procedure and action potentials separation, and 3) Averaging.

The stationary or undecimated wavelet transform (SWT) has the advantage of translation invariance and its performance was compared against the DWT method. The SWT method can be obtained by omitting the decimation and up-sampling the filters for the next level of processing from Mallat algorithm [16, 17]. The SWT was chosen considering its potential benefit in more exact action potential waveform estimation. One de-noising technique was used based on the method developed by Donoho [21, 22] and modified by Diedrich [12] and involved thresholding of the detail coefficients. A simple peak detection algorithm was then applied to the de-noised signal to detect action potentials and finally taking an average of all identified waveforms, an average action potential pattern was computed.

2.3.3 The method for generating simulated MSNA

In order to compare different action potential detection algorithms, simulated MSNA with varying noise levels was generated. Simulated signals were constructed with averaged action potentials extracted from long extracellular MSNA recordings during baseline and lower-body negative-pressure (LBNP, -10, -20, -40 and -60 mmHg) in three healthy subjects. A noise analysis was done before generating simulated MSNA. A 10s noise signal was extracted from each recording after held inspiration reflex (neural silence). The power spectral density (PSD) of the noise was estimated by Welch's method [25]. The result is shown in Fig. 2.4. The amplitude distribution of the noise was computed and fitted with a Gaussian distribution. Since the length of the noise was not long enough $\sim 10s$ for an appropriate simulation, a band-pass filter was designed based on the Kaiser window method with a center pass band frequency of 1 kHz and subsequently applied to a sequence of Gaussian white noise 60s in length. The PSD of the simulated noise after band-pass filtering approximated that of the recorded noise (Fig. 2.4).

Finally, We generated 60s of the simulated MSNA, 30s for the base-line and 30s for (LBNP -60 mmHg), (see Fig. 2.5). Each segment was assigned a mean burst rate of 30 bursts/min, (22 bursts/min for base-line, 38 bursts/min for LBNP -60 mmHg) and 15 spikes/burst. The signal to noise ratio (SNR) was defined as the ratio between the absolute peak amplitude of the action potential and the standard deviation of the noise as defined in [12, 13]. The SNR of the simulations was changed from 1 (poor SNR) to 6 (high SNR) with a step size of 0.5. Fig. 2.5 shows a simulated MSNA with $SNR = 3$.

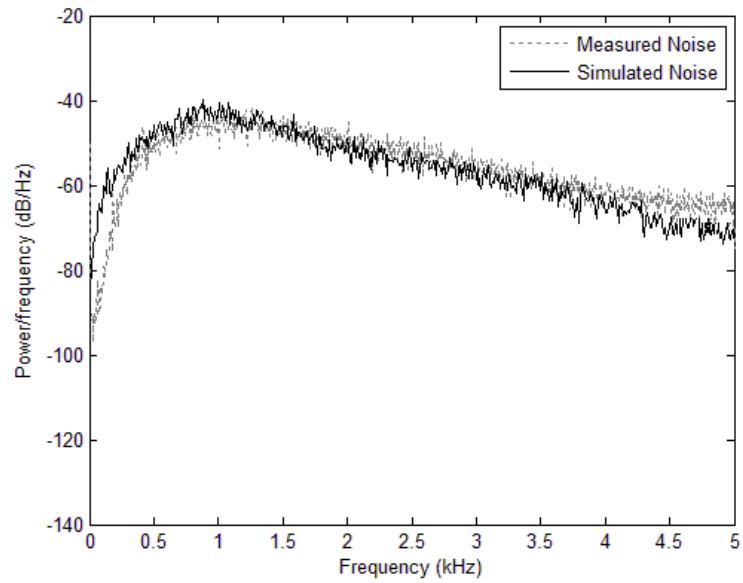


Figure 2.4: The power spectral density (PSD) of the measured and simulated noise

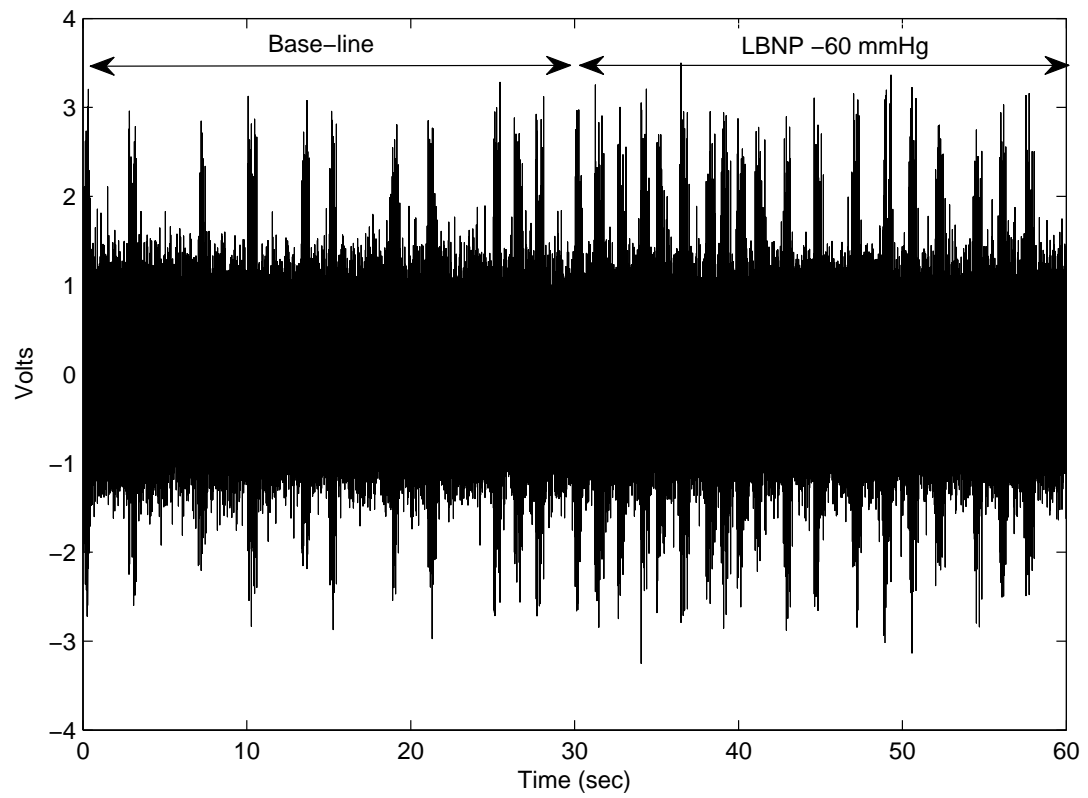


Figure 2.5: Simulated bursts of action potentials with SNR=3.

Several wavelet-based action potential detection algorithms were applied to the simulated MSNA signals. Two de-noising techniques were examined, 1) the standard thresholding method developed by Donoho [21, 22] and explained in (2.9) and (2.10), and 2) the modified thresholding method introduced by Diedrich [12] which simply multiplies a correction factor, k , in (2.9) for threshold calculation. This correction factor was fixed at 0.8 during all simulation. The three wavelet algorithms each using different de-noising methods, were selected as follows: the SWT with modified threshold (SWTM) [12], the DWT with standard wavelet threshold (DWTS) and DWT with modified threshold (DWTM) [12]. Performance evaluation was repeated 50 separate times for each SNR. The performance of each method was quantified using the percent of correctly detected action potentials (PCD), the percent of false positive alarms (PFP) and the percent of false negative alarms (PFN). The definition of the PCD, PFP and PFN are as follows:

$$PCD = \frac{N_{CD}}{N_{AP}} \times 100; \quad (2.12)$$

$$PFP = \frac{N_{FP}}{N_{CD} + N_{FP}} \times 100; \quad (2.13)$$

$$PFN = \frac{N_{FN}}{N_{AP}} \times 100; \quad (2.14)$$

where N_{CD} is the number of correctly detected action potentials, N_{AP} is the number of action potentials inserted into the simulation, N_{FP} is the number of false positive alarms and N_{FN} is the number of missed action potentials.

2.4 Results

2.4.1 Comparison between DWT and SWT

The detection performance of each of the three methods is displayed in Fig. 2.6. It can be seen that the SWTM results in a higher PCD and lower PFN for the $SNR \geq 3$ and lowest PFP for all SNRs. The DWTM acts similarly to SWTM in PCD and PFN for $SNR \leq 2.5$ and its PFP is the

highest for SNR between 2.5 and 4. The DWTS has the lowest PCD and the highest PFP for $SNR > 4$ and its PFN is the lowest during all SNRs. As result, the SWTM has the highest PCD and lowest PFP during all simulation and its PFN is the lowest for $SNR > 3$. Therefore, the SWT with Modified threshold method is the appropriate choice for action potential detection in human MSNA based on our experiment.

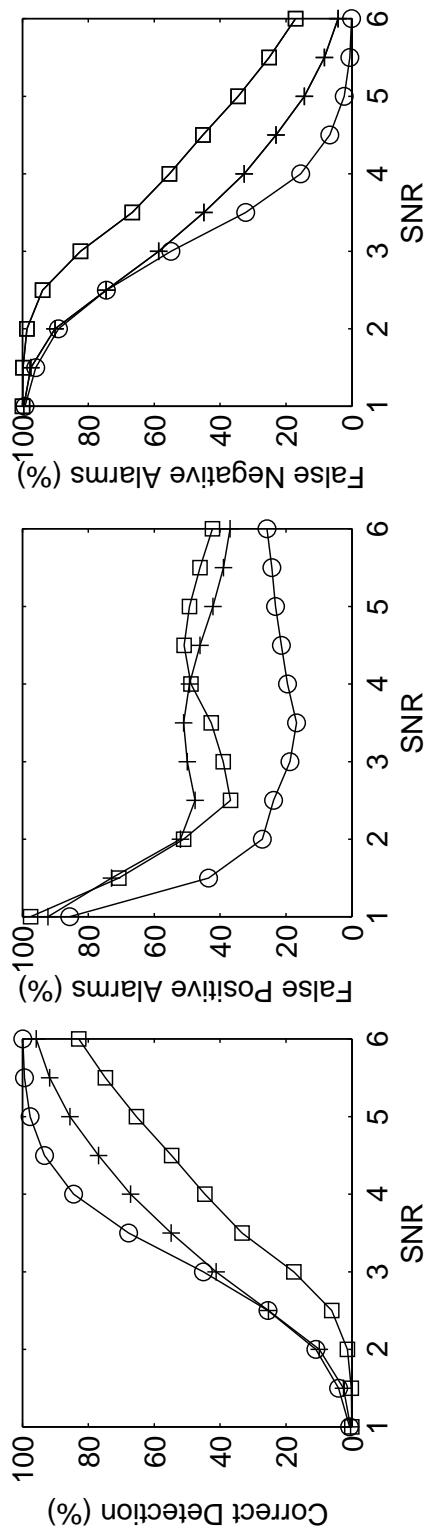


Figure 2.6: Mean results for simulations with varied noise levels. The simulations tested the SWT decomposition with Modified Threshold (circle), DWT with Modified Threshold (plus) and DWT with Standard Threshold (square)

2.4.2 An averaged action potential after band-pass filtering

In this section, we explain the method that has been used to find the averaged action potential after bandpass filtering. After recording the MSNA signals and converting them to the MATLAB file format, we selected bursts in the baseline and high activity sections. For the first subject, we found 152 bursts in long MSNA recordings. Then, we applied Stationary Wavelet Transform (SWT) with “Symlet 7” as mother wavelet, a decomposition level of 5, a hard thresholding procedure and a modified threshold level [12], to remove background noise in each burst. After removing the background noise, the peak detection algorithm was applied to find the negative peaks of the action potentials. Then, a discriminator algorithm separated each action potential by putting the peak of each action potential in the center of a predefined window. A 32 point window length (3.2 msec) was chosen on the basis that this duration is long enough to represent the human action potential. Fig. 2.7 shows the complete process for finding the averaged action potential. After finding the averaged action potential for subject 1, the same procedure was repeated to investigate the averaged action potential for subject 2 and subject 3. Fig. 2.8 shows the action potential waveforms for all three subjects. The three averaged action potentials are the same. Table 2.1 shows some statistical information about the number of bursts and the number of detected action potentials for each subject.

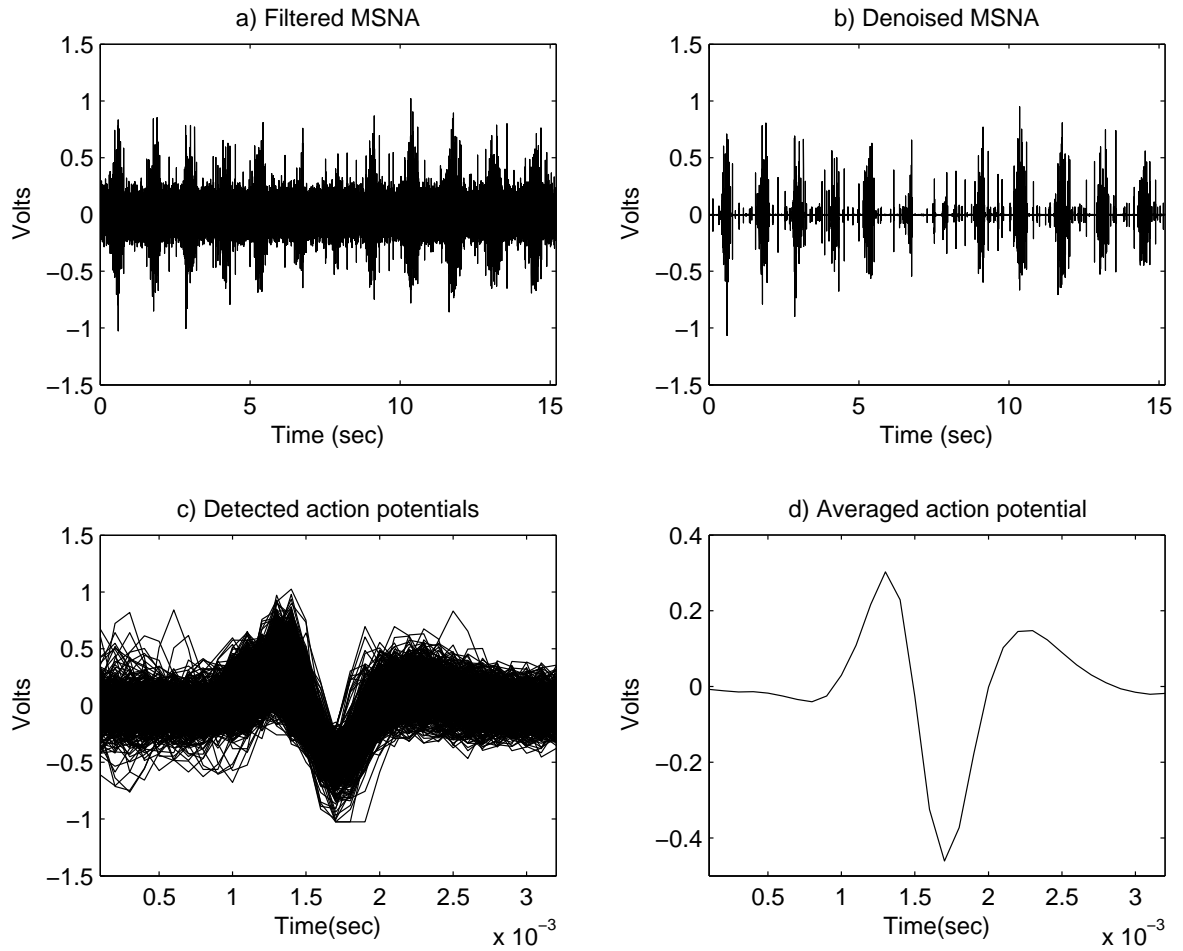


Figure 2.7: The complete process for finding the averaged action potential after bandpass filtering.

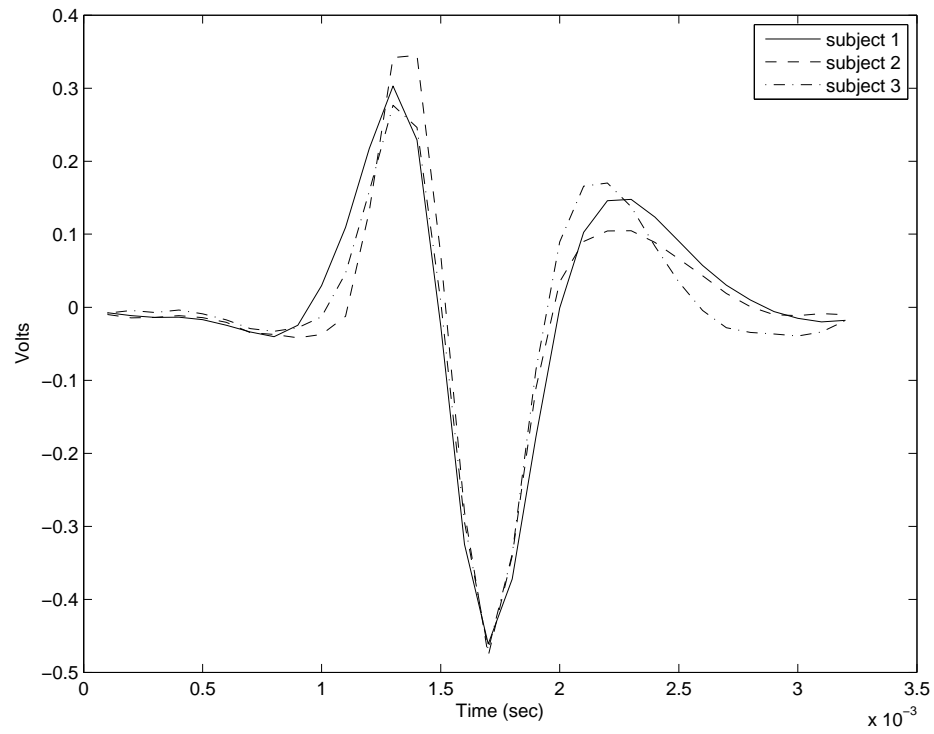


Figure 2.8: Averaged action potentials for all subjects after bandpass filtering.

Table 2.1: some statistical information about each subject

| Subject | No.Burst | No. of detected APs |
|---------|----------|---------------------|
| 1 | 152 | 1590 |
| 2 | 112 | 1085 |
| 3 | 94 | 541 |

2.4.3 An averaged action potential before pre-Amplification

After finding the averaged action potential patterns after the bandpass filter and confirming them for all subjects, the averaged patterns were determined for the signal before the bandpass filter (after variable gain-amp) and before the pre-amplifier. In order to examine the effect of the bandpass filter on the action potential's shape. To this end, the delay created by the bandpass filter was computed. Then after de-noising the filtered MSNA signal and finding the negative peaks as explained in the previous section, an algorithm corrected each peak's location with respect to the bandpass filter's delay to find the exact position of the peak before the bandpass filter. Once the position of the detected peaks was computed, a discriminator algorithm separated each action potential by putting the new peak of each action potential in the center of a predefined window. Taking an average of all detected waveforms, an averaged action potential pattern was computed, representing the action potential shape before the bandpass filter. As we mentioned earlier, the second goal of this part of the paper was to propose a method which could be used to find an averaged action potential from the MSNA signal before the pre-amplifier. In other words, we wanted to discover the raw pattern which comes through the electrodes. In order to do this, first we computed the total transfer function for all of the amplifiers (Pre-amplifier, Isolation-amplifier and Variable-gain amplifier) after the electrodes. The transfer functions for pre-amplifier isolation-amplifier and variable-gain amplifier were calculated theoretically using the circuit diagram provided by Bioengineering of University of Iowa for nerve traffic analysis system model 662C-3. The transfer functions were also calculated experimentally and they were similar to those calculated theoretically. Therefore, the theoretical transfer functions were used for the rest of the analysis in this section. Then by taking the discrete Fourier transform (DFT) of the averaged pattern before the bandpass filter and multiplying it by the inverse of the total transfer function of the amplifiers, the DFT of the averaged pattern before the pre-amplifier can be found. By taking the inverse DFT of this averaged pattern, the real action potential can be computed in the time domain. The process of finding a mean action potential template before pre-amplification is illustrated in Fig. 2.9. Fig.

2.10 shows the raw action potentials before the pre-amplifier. By comparing Fig. 2.8 and Fig. 2.10, it can be seen that the fundamental shape of the action potentials have not been changed by bandpass filtering. It is also worthwhile to compare the raw action potential waveform, Fig. 2.10, with an ideal action potential waveform which is shown in Fig. 2.11, [11]. An ideal action potential can be described by an exchange of ions across the neuron membrane [11]. As it is apparent the results in Fig. 2.10 are similar to an ideal action potential waveform in Fig. 2.11.

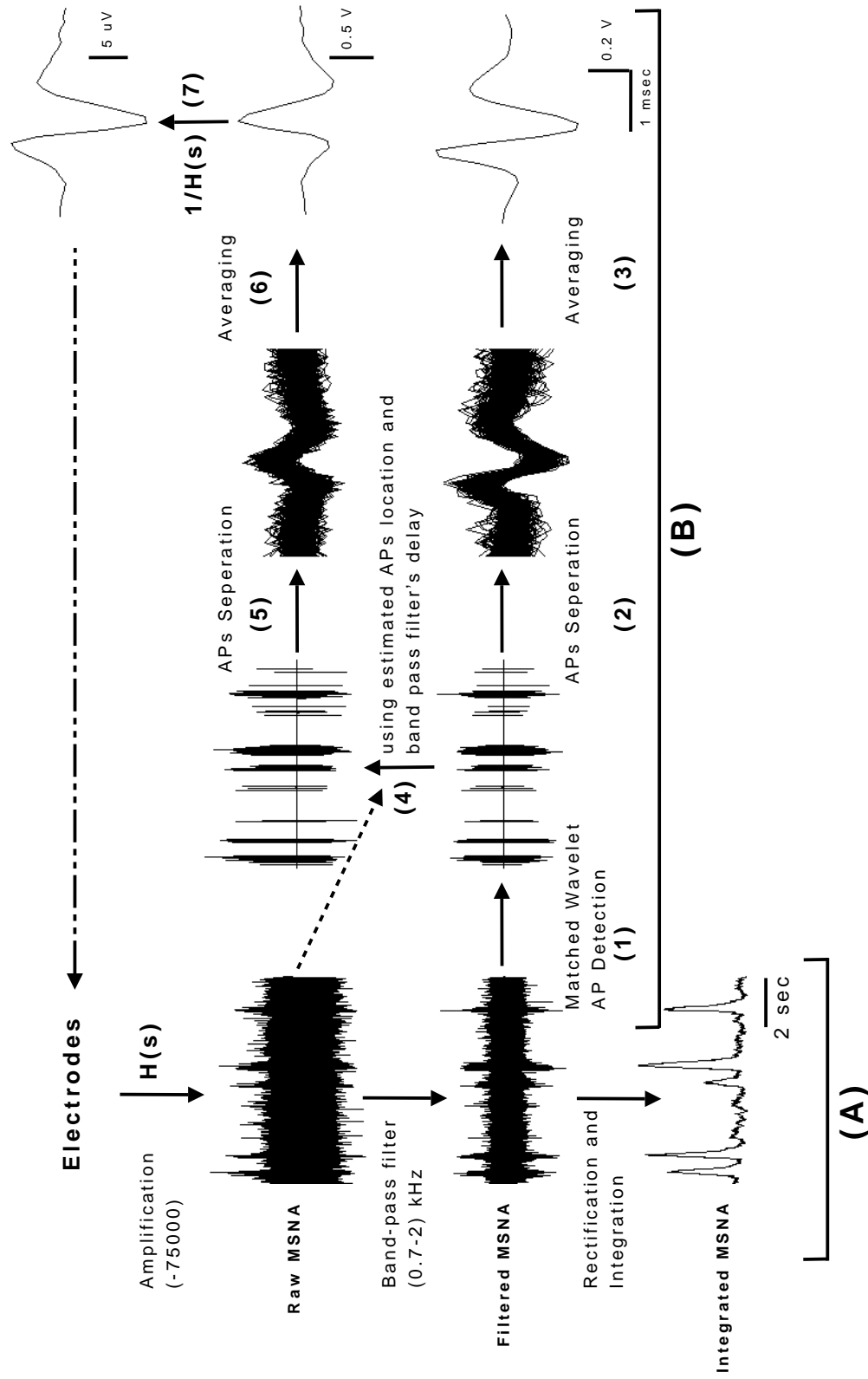


Figure 2.9: Illustration of the method for finding mean AP template before the bandpass filter and after electrodes, (A) Representative examples of the multi-unit raw, filtered and integrated MSNA. (B) step (1): applying matched wavelet AP detection method to the filtered MSNA signal, step (2) separating of the detected APs by using estimated locations and windowing, step (3) averaging the separated APs (mean AP template after band pass filter), step (4) extracting APs from the signal before band pass filter by using the estimated APs location, band pass filter's delay and windowing, step (5) same as 2, step (6) averaging the separated APs (mean AP template before band pass filter), step (7) inverse filtering provides a mean AP template after electrodes.

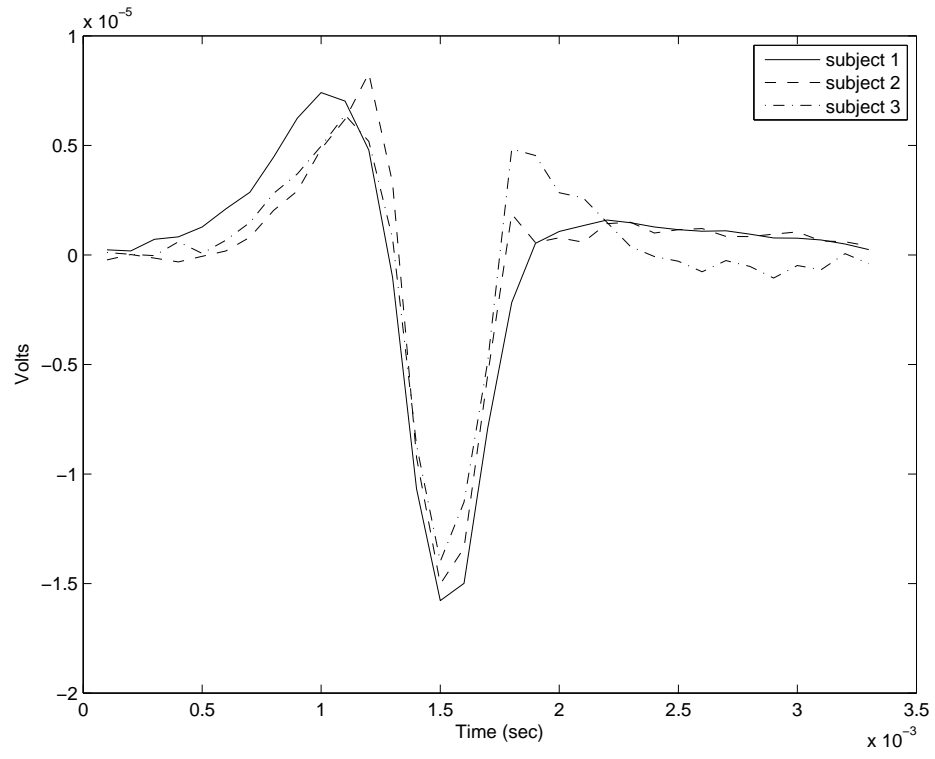


Figure 2.10: Averaged action potentials for all subjects before pre-amplification (after electrodes).

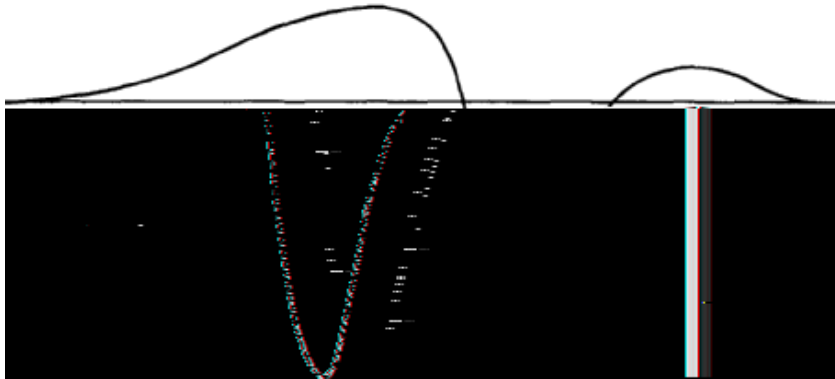


Figure 2.11: An ideal action potential waveform.

2.4.4 Action potential classification

In this section, we show and discuss the results of a classification algorithm which has been applied to all detected action potentials. After detecting all action potentials after bandpass filtering as described before, a matrix M_{mn} was formed, where m is the total number of detected action potentials and n is the length of each action potential. Then k-means clustering method [23], which uses one minus the sample correlation between points to measure distance between them, was applied to matrix M_{mn} to find different clusters. The classification algorithm found that almost all detected action potentials could be classified by one of 3 major classes. These classes were found in all subjects. Fig. 2.12 shows the 3 classes found in the detected action potentials after bandpass filtering (upper panel) and the corresponding action potentials before the pre-amplifier as described earlier. From a physiological point of view, clusters 1 and 2 can be described based on positive and negative ion discharges in the human nerves. However, cluster 3 may reflect a) action potentials distant from the electrode tip, or b) a superposition of the two action potentials firing in sequence. Further analysis needs to be done to verify these hypotheses. Distributions of action potentials among different subjects are shown in Table 2.2. It can be seen that the majority of the action potentials can be classified as class 1 and class 2. There are fewer action potentials in class 3 for the subject 1 than the same class in the subject 2 and 3.

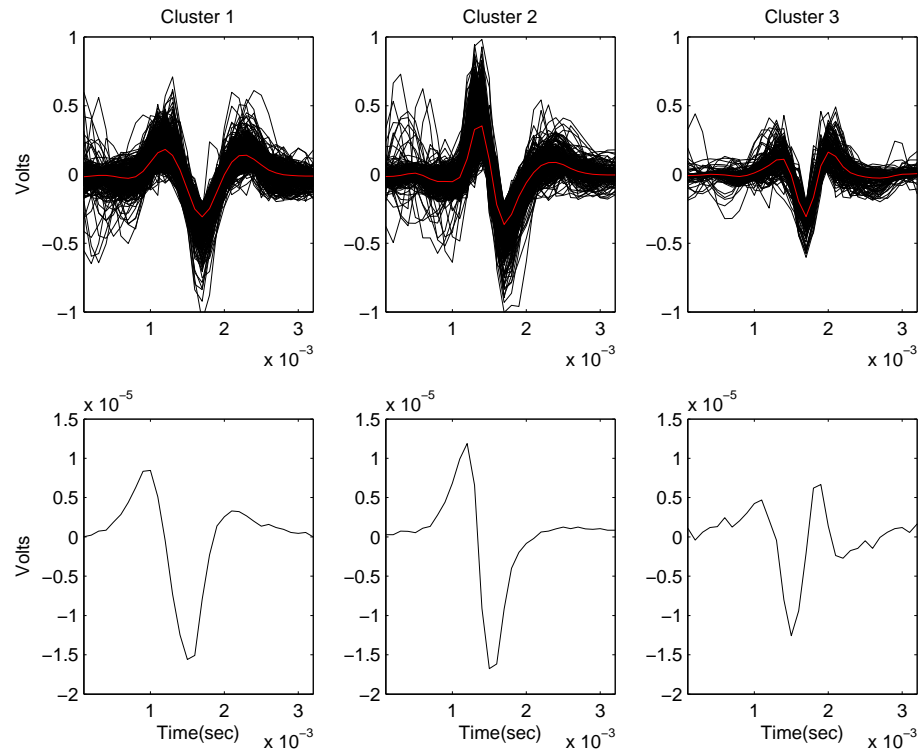


Figure 2.12: Classification of action potential waveforms. (upper panel) Major action potential waveforms classified in the filtered MSNA and (lower panel) the averaged action potential patterns before pre-amplification(after the electrodes).

Table 2.2: Distributions of 3 classes found from all 3 subjects

| Subject | Class 1 | Class 2 | Class 3 |
|---------|---------|---------|---------|
| 1 | 50% | 40.57% | 9.43% |
| 2 | 28.85% | 50.69% | 20.46% |
| 3 | 35.30% | 41.40% | 23.29% |

2.5 Conclusion

In this paper we have presented an approach for action potential detection in raw and filtered MSNA recordings. The performance of the discrete and stationary wavelet transform in detecting action potentials from extracellular sympathetic nerve recordings in humans was investigated in this paper. Two de-noising techniques (Standard [21, 22] and Modified [12] thresholding methods) were examined. The averaged action potential templates were computed from MSNA collected from three healthy subjects and were used to generate a simulated MSNA based on a new method. The performance of three wavelet-based action potential detectors were quantified in detecting action potentials from a simulated MSNA with varying noise levels using PCD, PFP and PFN . Results showed that the SWT with modified threshold method performed well for the SNR above 3.5 in terms of PCD and PFN and its PFP was lowest during all SNRs. The SWT method was applied to real MSNA signal for finding averaged action potential patterns and the effect of band-pass filtering was examined on action potential waveforms. Similar action potential patterns were identified from three healthy subjects. The classification algorithm found three major physiologically reasonable positive classes in all subjects.

In conclusion, the stationary wavelet transform with modified de-noising technique is a useful method to investigate sympathetic nerve activity and to study the action potential's discharge behavior in humans.

References

- [1] B. G. Wallin, "Peripheral sympathetic neural activity in conscious humans," *Ann. Rev. Physiol.*, vol. 50, pp. 565-576, 1988.
- [2] A. B. Vallbo, K. E. Hagbarth, H. E. Torebjork, and B. G. Wallin, "Somatosensory, propri-

- oceptive, and sympathetic activity in human peripheral nerves,” *Physiological Reviews.*, vol. 59, pp. 919-957, 1979.
- [3] J. K. Shoemaker, M. D. Herr, L.I. Sinoway, “Dissociation of muscle sympathetic nerve activity and leg vascular resistance in humans.,” *AM. J. Physiol*, vol. 279, pp. H1215-H1219, 2000.
- [4] J. K. Shoemaker, D. D. O’Leary, and R. L. Hughson, “PET(CO(2)) inversely affects MSNA response to orthostatic stress,” *Am. J. Physiol Heart Circ. Physiol.*, vol. 281, no. 3, p. H1040-H1046, Sept. 2001.
- [5] D. S. Kimmerly and J. K. Shoemaker, “Hypovolemia and MSNA discharge patterns: assessing and interpreting sympathetic responses,” *American Journal of Physiology-Heart and Circulatory Physiology.*, vol. 284, no. 4, p. H1198-H1204, Apr. 2003.
- [6] D. S. Kimmerly, D. D. O’Leary, and J. K. Shoemaker, “Test-retest repeatability of muscle sympathetic nerve activity: influence of data analysis and head-up tilt,” *Auton. Neurosci.*, vol. 114, no. 1-2, pp. 61-71, July. 2004.
- [7] J. M. Lundberg, A. Franco-Cereceda, Y. P. Lou, A. Modin, and J. Pernow, “Differential release of classical transmitters and peptides,” *Adv. Second Messenger Phosphoprotein Res.*, vol. 29, pp. 223-234, 1994.
- [8] W. P. De Potter, L. Dillen, W. Annaert, K. Tombeur, R. Berghmans, and E. P. Coen, “Evidence for the co-storage and co-release of neuropeptide Y and noradrenaline from large dense cored vesicles in sympathetic nerves of the bovine vas deferens,” *Synapse*, vol. 2, no. 2, pp. 157-162, 1988.
- [9] V. G. Macefield and B. G. Wallin, “Firing properties of single vasoconstrictor neurones in human subjects with high levels of muscle sympathetic activity.,” *J. Physiol.*, vol. 516, pp. 293-301, 1999.

- [10] A. L. Hodgkin, "The ionic basis of electrical activity in nerve and muscle," *Biol. Rev.* vol. 26 pp. 339-409, 1951.
- [11] C. Gold, D. A. Henze, C. Koch and G. Buzsaki, "On the Origin of the Extracellular Action Potential Waveform: A Modeling Study," *J Neurophysiol* vol. 95, pp. 3113-3128, 2006.
- [12] A. Diedrich, W. Charoensuk R. J. Brychta A. C. Ertl and R. Shiavi, "Analysis of raw microneurographic recordings based on wavelet de-noising technique and classification algorithm: Wavelet analysis in microneurography", *IEEE Trans. Biomed. Eng.*, vol. 50, no. 1, pp. 41-50, Jan. 2003.
- [13] R. J. Brychta, R. Shiavi, D. Robertson, A. Diedrich "Spike detection in human muscle sympathetic nerve activity using the kurtosis of stationary wavelet transform coefficients," *J. Neurosci. Meth.*, vol. 160, pp. 359-367, 2007.
- [14] R. J. Brychta, S. Tuntrakool, M. Appalsamy, N. R. Keller, D. Robertson, R. Shiavi and A. Diedrich, "Wavelet methods for spike detection in mouse renal sympathetic nerve activity," *IEEE Trans. Biomed. Eng.*, vol. 54, no. 1, pp. 82-93, Jan. 2007.
- [15] Q. Zhang, Y. Liu, L. Brown, and J. K. Shoemaker, "Challenges and opportunities in processing muscle sympathetic nerve activity with wavelet denoising techniques: detecting single action potentials in multiunit sympathetic nerve recordings in humans," *Auton. Neurosci.*, vol. 134, no. 1-2, pp. 92-105, July. 2007.
- [16] S. G. Mallat, "A theory for multiresolution signal decomposition: the wavelet representation," *IEEE Trans. Pattern Anal. Mach. Intell.*, vol. 11, no. 7, pp. 674-693, Jul. 1989.
- [17] S. G. Mallat, "Zero-crossings of a wavelet transform," *IEEE Trans. Inf. Theory.*, vol. 37, no. 4, pp. 1019-1033, Jul. 1991.
- [18] R. R. Coifman and D. L. Donoho, "Translation-invariant de-noising," in *Lecture Notes in Statistics.*, vol. 103, pp. 125-150, 1995.

- [19] J. Liang and T. W. Parks, "A translation-invariant wavelet representation algorithm with applications," *IEEE Trans. Signal Process.*, vol. 44, no. 2, pp. 225-232, Feb. 1996.
- [20] J. Pesquet, H. Krim and H. Carfantan, "Time-invariant orthonormal wavelet representations," *IEEE Trans. Signal Process.*, vol. 44, no. 8, pp. 1964-1970, Aug. 1996.
- [21] D. L. Donoho, "Ideal spatial adaptation by wavelet shrinkage," *Biometrika.*, vol. 81, no. 3, pp. 425-455, 1994.
- [22] D. L. Donoho, "De-noising by soft-thresholding," *IEEE Trans. Inf. Theory*, vol. 41, no. 3, pp. 613-627, May. 1995.
- [23] G. A. F Seber, *Multivariate Observations*. New York: Wiley, 1984.
- [24] I. Johnstone and B. Silverman, "Wavelet threshold estimators for data with correlated noise," *J. Roy. Statist. Soc. Series B Methodological.*, vol.59, pp. 319-351, 1997.
- [25] P. D. Welch, "The use of fast fourier transform for the estimation of power spectra: A method based on time averaging over short modified periodograms," *IEEE Trans. Audio Electroacoust.*, vol. AU-15, pp.70-73, June 1967.

Chapter 3

Spike detection in human muscle sympathetic nerve activity using a matched wavelet approach

3.1 Introduction

Sympathetic nerve activity plays an essential role in the normal regulation of blood pressure in humans [1] and in the etiology and progression of many chronic diseases. Thus, the evaluation of sympathetic activity has become an important research topic in cardiovascular studies in normal and pathological conditions, such as heart failure [2–4] and hypertension [5, 6].

Sympathetic outflow associated with blood pressure regulation can be recorded by direct measurement using the microneurographic technique which involves the insertion of a tungsten microelectrode with a tip of 1 to 5 μm into a peripheral nerve (usually the peroneal nerve) [7]. The neural activity recorded from a nerve bundle innervating the vessels in the muscle is called muscle sympathetic nerve activity (MSNA). This signal is defined as “multi-fibre” in that several axons are recorded from simultaneously. A general characteristic of the MSNA signal is spontaneous burst activity of action potentials separated by silent periods. An important but

problematic feature of this MSNA signal is that it is dominated by high levels of environmental and bioelectric background noise that produce a low signal-to-noise neurogram.

Traditionally, analyzing of the MSNA signal involves three steps, namely, bandpass filtering (\sim bandwidth of 700-2,000 Hz), rectification and integration (typically, with a time constant 0.1 s). These steps reduce background noise and provide a quantitative measure of sympathetic outflow. The strength of sympathetic activity is then expressed both as number of bursts/100 heartbeats (burst incidence) and burst/min (burst frequency). Moreover, the total MSNA activity can be described as (burst incidence or burst frequency \times averaged burst area).

However, one of the drawbacks of this traditional processing of the human MSNA signal is that the integration process loses considerable neurophysiologic information. For instance, information regarding action potential content (i.e., number of action potentials/burst, action potential morphology and inter-spike intervals) is lost during integration. This is problematic because the ability to test specific hypotheses regarding post-ganglionic sympathetic neuronal recruitment requires information on action potentials as individuals and/or, as a population. For example, to examine the presence of multiple populations of post-ganglionic axons, as proposed by Wallin et al [8], and their timing, it is necessary to assess the action potential content of the multi-fibre recording for variations in action potential frequency, morphology and timing. Major challenges in this objective are to separate the action potential signal from the background noise and to sort them into different classes.

Methods that achieve detection and sorting of spikes from multi-unit but non-sympathetic neural recordings have been studied extensively [see 9–11, 14]. The spike detection has been addressed in some neural recordings (e.g., motor unit action potential, myoelectric signals, radial nerve recordings and etc) and spike classification or sorting has been used [10, 11, 15, 16]. Nonetheless, the detection of spikes in the MSNA signal remains problematic because of the high level of background noise (i.e., low signal-to-noise ratio (SNR)).

Recently, automated wavelet-based methods have been implemented to detect and classify neural recordings [17–22]). The general idea of wavelet analysis of neural signals is that a

nerve signal containing a train of action potentials but contaminated with noise is decomposed by the wavelet transform into a set of time-scale and time-translated version of a particular template called “mother wavelet” to provide a resemblance index (i.e., wavelet coefficient) between the signal of interest (e.g., action potentials) and the mother wavelet. If the index is “large” the resemblance is strong and if the index is small, the resemblance is weak. Therefore, the mother wavelet should be similar to the signal under interrogation. For detection purposes, the wavelet coefficients related to action potentials and noise portions can be separated using wavelet de-noising techniques [23, 24].

Application of wavelet analysis to the MSNA signal was introduced by Diedrich et al [25] in an attempt to reduce noise and detect action potentials in the filtered MSNA signal. Their method involved applying a discrete wavelet transform (DWT) with “Symlet 7” as a mother wavelet to the MSNA signal. The denoised MSNA signal was constructed by the thresholding of detailed coefficients using a denoising technique. Subsequently, action potentials were identified in the denoised MSNA signal by applying a simple peak detection scheme. This wavelet method was modified by the same group [26] to use a stationary wavelet transform (SWT) instead of the DWT along with kurtosis of wavelet coefficients for better estimation of the threshold. We have also used this SWT method for action potential detection [27, 28]. However, the retrieval rate of action potentials with this method is relatively low (approximately 70% when SNR is 3 (see section 3.2.5 for SNR definition)) and aberrant waveforms are observed. A different group has used a mixed separation model applied to human MSNA recordings [29]. This approach accurately assesses action potential firing patterns (inter-spike interval, spike rate) but provides minimal information on action potential morphology. Indices of the action potential morphology, such as size and width, provide important information on the neural axon characteristics.

Unfortunately, the wavelet approach has not been optimized to maximize its ability to detect action potentials particularly with respect to the best choice of “mother wavelet”. Matlab’s “Symlet 7” mother wavelet, being the best fit of choice in the library of options, was selected in

the previous studies via visual judgement. However, the “Symlet 7” is not directly derived from an actual action potential waveform. As a result, action potentials detected from the wavelet technique with a non-matched mother wavelet (Symlet 7 in this case) may be distorted, producing the aberrant waveforms mentioned above. On the other hand, the decomposition of a signal in the presence of noise using a wavelet matched to the signal should produce a sharper and higher peak in the wavelet domain (i.e., time-scale domain) as compared to non-matched wavelets, enhancing the ease of thresholding and detection of the wavelet coefficients thereby maximizing detection probability and minimizing false alarms.

Methods for optimizing the wavelet have been proposed [30–33]. These methods propose a signal-dependent selection of the mother wavelet based on an optimization criterion. Other techniques have used the theory of a matched filter to design a wavelet matched to a specific signal for detection purpose [34–39]. These methods have improved event detection in comparison with methods that use non-matched wavelets.

Therefore, the primary objective of this paper was to enhance the wavelet-based approach for detection of action potentials in MSNA recordings by designing a matched wavelet from an actual mean action potential waveform. Our algorithm uses a continuous wavelet transform (CWT) with the matched wavelet to convert the filtered MSNA signal to a matched wavelet base. In this domain, we expect to see sharper peaks in the location of each action potential. By applying a threshold, estimated from the wavelet coefficients, the wavelet coefficients related to action potentials can be separated from the background noise. Finally, by searching for local maxima, the exact location of each action potential can be determined and then extracted from the original filtered MSNA signal. The preliminary results of the new action potential detection algorithm based on matched wavelet were originally reported in [40].

The reason for using CWT is that this transform uses only a family of wavelets. Since we design a new mother wavelet in this chapter, it is easier to use CWT directly. However, it is also possible to use SWT method, but a pair of quadrature mirror filters need to be constructed from the new matched wavelet and corresponding scaling function [37].

because a wavelet was designed directly from an actual action potential waveform

3.2 Materials and Methods

The methods aim to develop a spike detection algorithm by designing a matched wavelet using real recordings of the MSNA data, to evaluate the spike detection algorithm using a simulated MSNA signal and then to apply the new spike detection method to real MSNA data.

3.2.1 Data acquisition and recording conditions

The MSNA data were recorded from seven individuals (two males, five females, 23 - 30 years). All participants were healthy as determined by a medical questionnaire and family history. The experimental procedures were approved by the Health Sciences Research Ethics Board at The University of Western Ontario and all participants provided informed written consent before participating in the study.

Recordings of MSNA were obtained from the peroneal nerve using a 200 μm diameter, 35 mm long tungsten microelectrode tapering to an uninsulated 1 to 5 μm tip. This electrode was inserted percutaneously into the nerve just posterior to the fibular head. The nerve contains bundles of sympathetic nerves that target blood vessels in muscle or skin (see Fig. 3.1A). A reference electrode was positioned subcutaneously 1-3 cm from the recording site. An MSNA site was confirmed by manually manipulating the microelectrode until a characteristic pulse-synchronous burst pattern was observed. The burst pattern was such that it did not produce skin paresthesias and increased in response to voluntary apnea but not during arousal to a loud noise [7]. Neurograms were measured with a nerve traffic analysis system (662C-3, Bioengineering of University of Iowa, Iowa City, IA). The neural signal was preamplified with a gain of 1000 (using preamplifier and isolation amplifier, gain=100 and 10, respectively) and further amplified with a gain of 75 (using a variable gain amplifier gain=0.1-99). This neuronal activity was then band-pass filtered (bandwidth of 700-2,000 Hz) and the filtered MSNA was rectified and

integrated. Integration is accomplished with a leaky integrator set with a 0.1 s time constant (see Fig. 3.1B). All signals were digitized with a data acquisition system (PowerLab software, ADInstruments Inc.) at a sampling rate that varied from 100 Hz for the rectified and integrated neurogram to 10 kHz for the amplified and filtered neurogram.

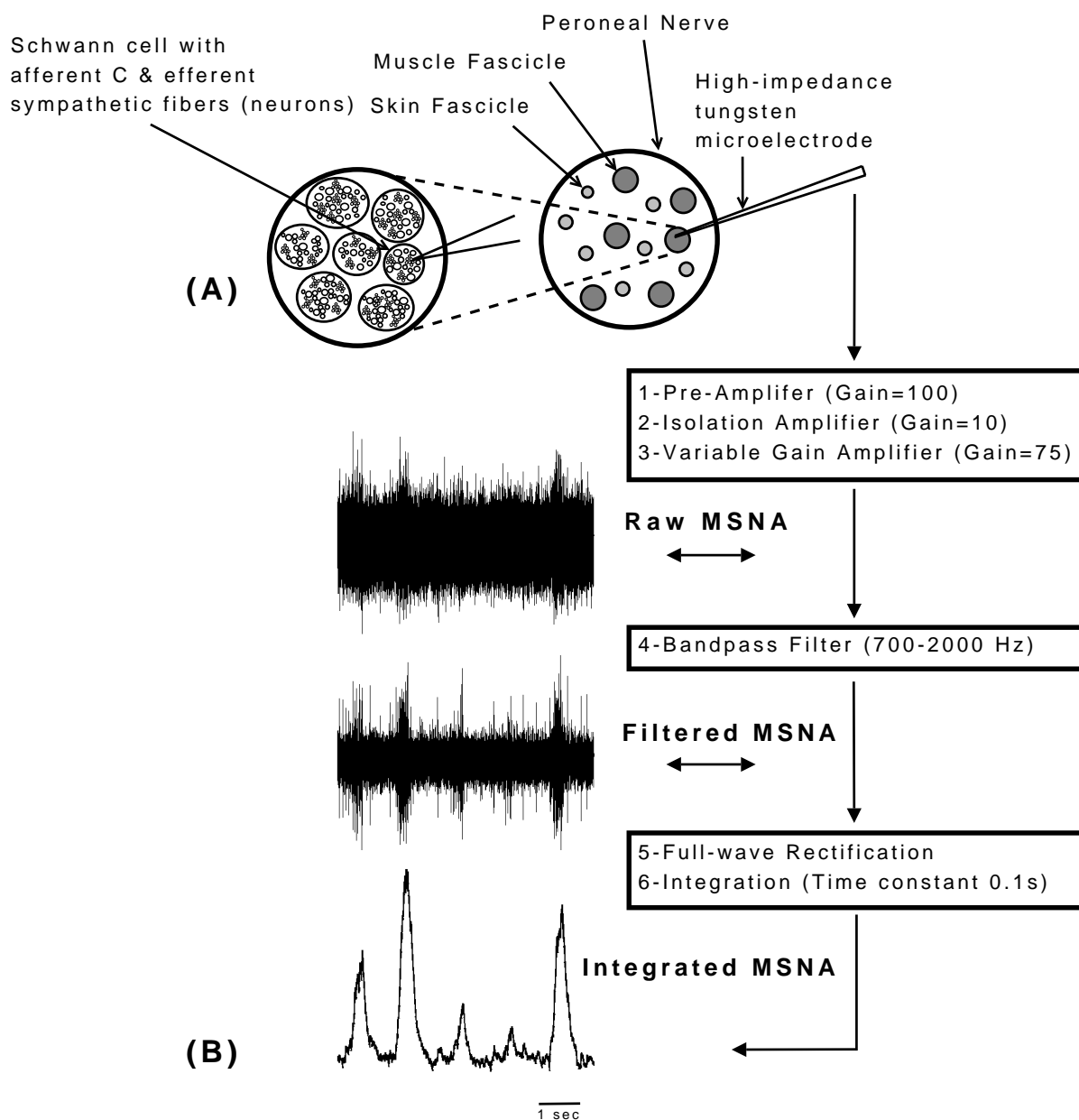


Figure 3.1: The cross-section of the peroneal nerve and common signal conditioning of the MSNA signal. (A) Schematic representation of a microelectrode inserted into a human peripheral nerve for sympathetic recordings. The nerve contains bundles of sympathetic nerves that target blood vessels in muscle or skin, Adapted from [41, 42]. (B) Representative examples of the raw, filtered and integrated muscle sympathetic nerve activity.

3.2.2 Action potential detection using a matched wavelet

Our action potential detection algorithm involves five main stages: a) designing a wavelet matched to a mean action potential template constructed using spike templates extracted from several real raw MSNA signals, b) performing wavelet transform of the filtered MSNA signal using the matched wavelet, c) separating the wavelet coefficients related to action potentials and noise using wavelet thresholding techniques, d) estimating the location of individual action potentials, and e) separating action potentials from the original filtered MSNA signal using locations determined in step d).

This algorithm does not sort spikes from different axons, but it attempts to identify the exact location of action potentials embedded in high levels of noise which is the most challenging task in the MSNA recordings. However, once detected individual action potentials can be clustered in terms of their peak-to-peak amplitude or classified using different approaches (e.g., K-means clustering). The task of clustering and characterizing action potentials is beyond the scope of this study.

To design a wavelet matched to the mean action potential template, we use theoretical works proposed by Chapa and Rao [37]. They showed that there is a solution for matching both the amplitude and phase of the wavelet spectrum to that of the signal of interest in the frequency domain while ensuring the necessary conditions for an orthonormal multi-resolution analysis (MRA). Moreover, the resulting wavelet looks like the signal of interest and it is bandlimited. The decomposition of the filtered MSNA signal into the matched wavelet basis is then accomplished using a continuous wavelet transform (CWT) with the matched wavelet. In the wavelet domain, the wavelet coefficients (i.e., resemblance index) are considerable in the presence of action potentials and negligible for noise segments. These wavelet coefficients related to action potentials and noise portions can be separated using wavelet thresholding techniques. After the wavelet thresholding stage, a wavelet coefficient of maximum magnitude can be considered as the maximum correlation between the matched wavelet and the signal. As a result, by finding the local maxima in the wavelet coefficients associated to action potentials

(e.g., after thresholding), the location of individual action potentials can be determined. Finally, the action potentials are extracted from the original filtered MSNA signal using the estimated locations. In this way, the amplitude and morphology of each extracted action potential remains unaltered. Each step will be explained in subsequent sections.

3.2.3 Wavelet decomposition using continuous wavelet transform with matched wavelet

The continuous wavelet transform (CWT) of an arbitrary function $f(x)$ is a projection of that function onto the wavelet basis and is given by the following expression

$$W_f(a, b) = \int_{-\infty}^{\infty} f(x) a^{-\frac{1}{2}} \psi\left(\frac{x-b}{a}\right) dx. \quad (3.1)$$

where $a > 0$ represents the scale and b is the translation. One can choose dyadic scales and translations from a discrete set $\{a_j = 2^j; b = k2^j; j, k \in \mathbf{Z}\}$. The mother wavelet is $\psi = \psi_{1,0}$. The matched wavelet, designed in this study, is a discrete function (i.e., $\psi(k) = \psi(k\Delta x)$). A discrete approximation of the CWT can be implemented by replacing integration with summation in (3.1). The steps for the translation parameter, b , are equal to the original signal step and can be calculated by the sampling frequency of the signal $f_s(kHz)$ and its duration $T(s)$, simply, $b \in \{0, 1, \dots, T f_s\}$ which provides the finest translation steps possible. Also, because of the advantage of designing a matched wavelet to the mean action potential template (see section 3.2.4), there is no need to use multiple scales for (a) in (3.1). Indeed, for the first scale $a = 1$ (i.e., matched mother wavelet), the projection of any arbitrary action potential onto the matched wavelet will be maximum. This is the major difference between our approach and previous approaches that use multiple scales for the CWT [21] or multiple decomposition levels for the DWT or SWT [25, 26].

After applying the CWT with matched wavelet to the signal of interest (i.e., the filtered MSNA signal), a new representation of the signal is obtained based on its wavelet coefficients,

where only a few wavelet coefficients will be maximum corresponding to action potentials and other coefficients related to noise will be negligible. In order to separate these coefficients, a thresholding procedure that uses the standard deviation of the noise needs to be calculated. Several methods for finding such a threshold and estimating the noise level were proposed previously [23, 24, 43]. In the case of colored noise, the standard deviation of the noise (i.e., σ_j) changes in each level of decomposition; therefore, a level-dependent estimate of the σ_j is required (Eq. 3.2)

$$\sigma_j = \text{median}(|W(a_j, b) - \overline{W(a_j, b)}|)/0.6745 \quad (3.2)$$

where $W(a_j, b)$ are the wavelet coefficients for scale j (i.e., $j = 0$ in this chapter) computed by CWT and matched wavelet. Equation (3.2) is then used in the calculation of the standard colored noise threshold [43]

$$T_j = \sigma_j \sqrt{2 \log_e(N)} \quad (3.3)$$

In (3.3) N is the length of the input signal. A modified form of Eq. (3.3) has improved the detection performance in human MSNA signal ([25]). This modified threshold is called modified colored noise threshold (T_j^M) and is shown in Eq. (3.4)

$$T_j^M = 0.8\sigma_j \sqrt{2 \log_e(N)} \quad (3.4)$$

The wavelet coefficients are later thresholded by a hard thresholding procedure as follows

$$W' = \begin{cases} W(a_j, b) & \text{if } |W(a_j, b)| > T_j^M \\ 0 & \text{if } |W(a_j, b)| \leq T_j^M \end{cases} \quad (3.5)$$

After thresholding, the location of action potentials (i.e., action potential arrival times) needs to be determined. The maximum correlation between each action potential and the matched wavelet basis function corresponds to a wavelet coefficient of maximum magnitude. Therefore, finding the largest suprathreshold wavelet coefficient can be taken as a good approx-

imation to the occurrence time of the action potentials.

Finally, the action potential waveforms are obtained from the original MSNA signal by putting the estimated location of action potentials in the center of a predefined window. The width of the window can be chosen by the user; usually, a 32 point window length (i.e., 3.2 ms at a 10-KHz sampling rate) is chosen on the basis that this duration is long enough to represent the human action potential.

3.2.4 Matching a wavelet to the mean action potential template

The design of a new mother wavelet requires a mean action potential template. We assume that the shape of post-ganglionic action potentials is similar across axons and individuals with only the amplitude of the action potentials differing among axons and across the subjects as this feature is determined by axonal size and distance from the recording electrode. We also assume that overlap between action potentials can occur but the probability of the overlapping spikes is relatively low in the MSNA recordings; this issue will be addressed using a simulation in section 3.2.7 and section 3.3.3.

We divided the subjects under study in two different groups. We used MSNA data from the first group (five subjects) for building our main mother wavelet template. In contrast, the MSNA data from the second group (two subjects) was used to build a simulated MSNA data for evaluation of our action potential detection algorithm. To build the mean action potential template the ten largest sympathetic bursts (i.e., largest amplitude) were chosen from each of five participants in the first group during supine rest. To build the new matched wavelet it was necessary to find a sufficient number of action potentials from real recordings. To do so, the methods described previously [27] which incorporated a wavelet approach was used based on the SWT method with “Symlet 7” as the mother wavelet followed by peak detection to identify the locations of action potentials. The action potentials were then extracted from the original raw MSNA signal using estimated locations and a window of 3.2 ms in length. To ensure that distinct and non-overlapping (non-summated) action potentials were used in the average

template, all action potentials with an inter-spike interval of ≤ 1.4 ms were excluded.

Finally, the mean action potential template was constructed by averaging all detected non-overlapping action potentials in ten bursts for each participant. Each mean action potential was normalized (i.e., $\|S_i\|_2 = 1$ where S_i is a mean action potential vector). The mean action potential templates were then averaged over five participants to build one mean action potential template. In total, 900 action potentials were incorporated in the averaged template. Note that this procedure for building the mean action potential template was done “once and for all” for this group of individuals. The design of the matched wavelet was based on this mean action potential template and was used for all analyses in this study. Fig. 3.2 shows the detected action potentials for each individual (upper panel) and the normalized mean action potential template for each subject (lower panel).

The extracellular action potential in human MSNA is triphasic and templates similar to those produced in the current study have been shown in [25, 26, 44, 45]. Also, the action potential morphology was not noticeably different between individuals (see Fig. 3.2). Therefore, this average action potential was considered suitable for application to building a template that could be used across all tests in this report; if any variations occurred, they were incorporated into the very template used to study the participants in this study. The matched wavelet for the mean action potential template was designed using the method described in (3.5).

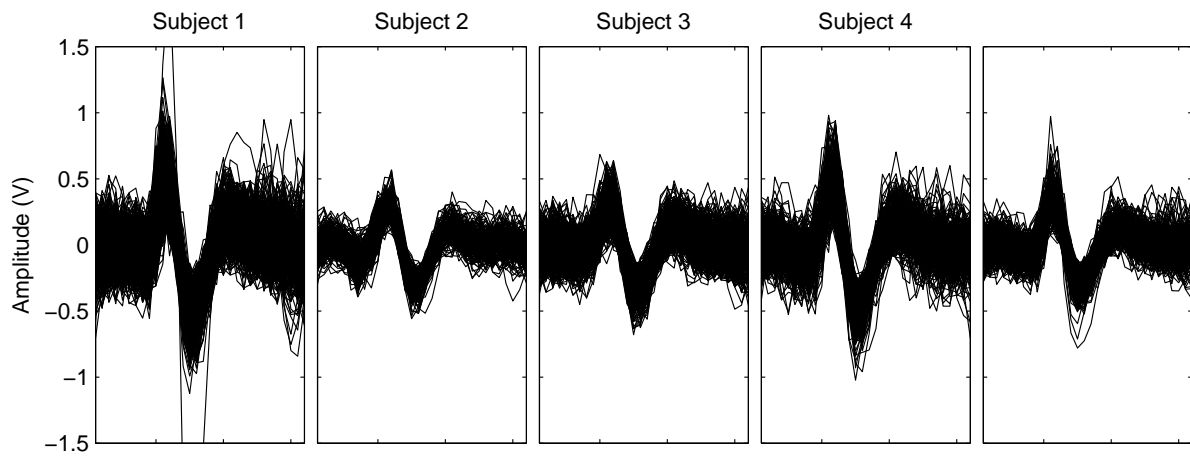


Figure 3.2: Detected and mean action potential templates in five subjects. Each column shows all detected action potentials in each subjects (upper panel) and the mean action potential template (lower panel). Notice that the action potential morphology is not significantly different between individuals. A mean action potential template across five subjects is constructed by averaging all five mean action potential templates shown in the lower panel.

3.2.5 A new method for generating simulated MSNA signal

To properly test the detection performance of the new action potential detector, a simulated MSNA signal was generated and its content was assessed. The simulated MSNA signal was generated by extracting action potential templates from the real MSNA signal and inserting them randomly into noise (with varying levels) in burst fashion.

Data segments, 60 s in length, were extracted from the MSNA signal (both integrated and filtered MSNA) in the first group from each individual during baseline activity. The inter-burst interval distribution was calculated based on the location of each burst of the integrated neurogram (i.e., the centers of the burst) for each of the participant and averaged over five participants (see Fig. 3.3A). The inter-spike interval and within-burst spike distribution were estimated and averaged over five participants (see Fig. 3.3B and 3.3C, respectively). These data formed the parameters from which the simulated MSNA was generated.

Three different simulated signals, each 60 s in length, with different mean burst rate (i.e., bursts/min) and spike rate (i.e., spikes/min) were constructed using the two mean action potential templates extracted from the two remaining subjects using our previous approach [27] as explained in section 3.2.4. The two templates are shown in Fig. 3.3I.

The process of generating a simulated signal is as follows: First, the position of each burst was assigned randomly according to estimated inter-burst distribution and a fixed burst duration of 0.8 sec. Three different mean burst rates were used; first simulation (10 bursts/min), second simulation (30 bursts/min) and third simulation (45 bursts/min). Second, the two mean spike templates (derived from the second group) were randomly inserted into bursts based on the estimated spike arrival time distribution and the inter-spike interval distribution. Two different mean action potential templates were used in our simulations to ensure that the new algorithm is not sensitive to a particular waveform shape. Different spike rates were used for each simulation where 100 spikes/min, 600 spikes/min and 1350 spikes/min were used for the first, second and third simulation, respectively. The neural noise was generated and added to each of the simulated signals.

In order to build a noise signal with the same characteristics of the real neural noise, a linear prediction coefficient (LPC) method [46] was applied to a segment of real neural noise (e.g., a 10-sec segment after the cessation of a breath hold) (Fig. 3.3D) to estimate filter coefficients of an autoregressive (AR) model (Fig. 3.3E). Then, the resulting AR filter with order 150 was applied to a sequence of Gaussian white noise, 60 s in length, with varying noise levels. After AR filtering, the power spectral density (PSD) and normalized autocorrelation function of the simulated noise were shown to be very similar to those of the extracted real neural noise (Fig. 3.3F and 3.3G, respectively). Both real and simulated noises showed the Gaussian probability density distribution (Fig. 3.3H).

The SNR was defined as the ratio between the absolute peak amplitude of the action potential and the standard deviation of the noise [21, 25, 47]. The SNR of the simulations was changed from 1 to 5 with a step size of 0.5. To provide some feeling for the noise level, Fig. 3.4 shows a segment of a simulated burst with 20 action potentials at two different SNRs.

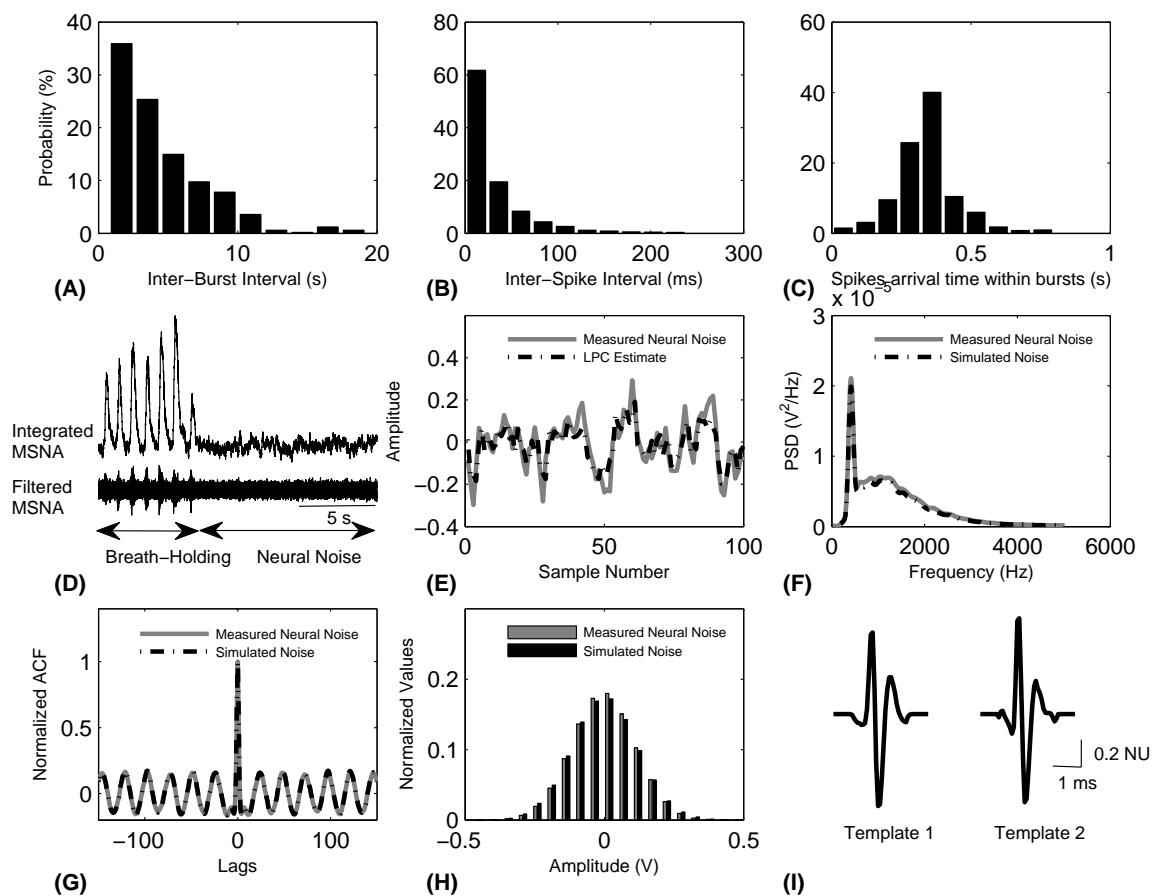


Figure 3.3: Illustration of the simulation components. (A) Inter-burst interval distribution. (B) Inter-spike interval distribution. (C) Distribution of spikes arrival time within bursts. (D) Representative examples of the integrated and filtered MSNA signal during and after breath-holding, the segment after breath-holding is assumed to be neural noise. (E) The output of the linear prediction filter coefficients (LPC) (black) vs. measured neural noise (gray). (F) The power spectral density (PSD) of the measured (gray) and simulated noise (black). (G) The normalized autocorrelation function of the measured (gray) and simulated noise (black). (H) Histogram of the measured neural noise (gray) vs. simulated noise (black). (I) Two templates that were used for simulation.

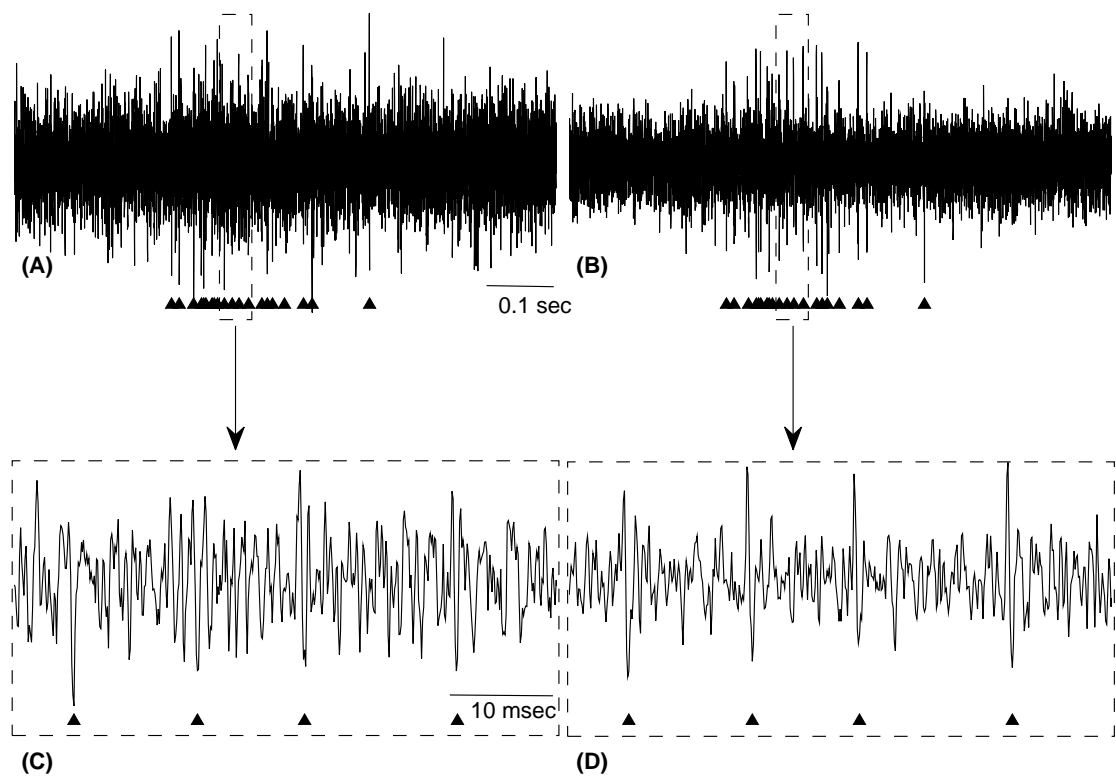


Figure 3.4: A simulated burst at two different SNRs. (A) A simulated burst with 20 action potentials at SNR=3, the black triangles indicate the location of the action potentials. (B) The same simulated burst at SNR=4. (C) and (D) Two enlarged portions of the signal in A and B (shown with rectangles). Compare the level of noise samples and amplitudes of action potentials.

3.2.6 Evaluation of detection performance using simulated data

The matched wavelet spike detector (MWD) method using a modified colored noise threshold (Eq. (3.4)) as a threshold estimator was compared against two common wavelet-based spike detection algorithms. The two wavelet algorithms were as follows: 1) the stationary wavelet transform with modified colored noise threshold (SWT, Eq. (3.4)) [26, 27]. Notice that a kurtosis method has been used for better estimation of the wavelet threshold [26]. We found the kurtosis method to be computationally expensive for the purpose of the current study. Therefore, the SWT method was used with a modified threshold for comparison here. However, the kurtosis method can give a better threshold. 2) The discrete wavelet transform with modified colored noise threshold (DWT) [25]. Both SWT and DWT used “Symlet 7” as the mother wavelet, decomposition level of 5 and hard thresholding. Both SWT and DWT methods showed a better detection performance than the unsupervised amplitude discriminator [48]. Therefore, the detection using an amplitude discriminator will not be a subject of further investigation.

The performance of the MWD versus the SWT and DWT was quantified using the percentage of correct detection of action potentials (PCD) and the percentage of false positive alarms (PFP). In other literature the PCD and PFP are known as sensitivity and false discovery rate, respectively. The definition of the PCD and PFP are as follows:

$$PCD = \frac{N_{CD}}{N_{AP}} \times 100; \quad (3.6)$$

$$PFP = \frac{N_{FP}}{N_{CD} + N_{FP}} \times 100; \quad (3.7)$$

where N_{CD} is the number of correctly detected action potentials, N_{AP} is the number of action potentials inserted into the simulation and N_{FP} is the number of false positive alarms. Performance evaluation was repeated 50 separate times for each SNR and simulation.

3.2.7 Performance evaluation of the algorithm on overlapping spikes

A consequence of multi-fibre neural recordings, where multiple action potentials are firing within a short period of time (e.g., 0.8 sec), is the probability that overlapping spikes may occur and summate. This eventuality would reduce the number of counted spikes and modify the amplitude of the detected action potential. To our knowledge, none of the studies reporting spike detection methods applied to MSNA signal have dealt with the issue of overlapping spikes. Here, we evaluate the performance of our MWD method on the detection of overlapping spikes. The details of this simulation were based on known discharge properties of human MSNA. In the MSNA signal, bursts of sympathetic activity in muscle nerves are tightly linked to the cardiac cycle. Macefield and Wallin [45] showed that in the recordings of single post-ganglionic sympathetic axons in young and healthy human subjects, the mean firing frequency (i.e., the mean of the inverse of all inter-spike intervals) was only 0.33 Hz and the firing probability (i.e., the percentage of heart beats during which single units fired,) was 35%. These numbers changed slightly during different pathological disorders or physiological stresses [3, 42, 45]. These authors concluded that, in younger healthy individuals, single muscle sympathetic neurons usually fire once during sympathetic bursts both in subjects with a high and in subjects with a low number of bursts at rest. Thus, it is reasonable to model action potentials as occurring independently of each other.

Based on the Macefield's results [45], an experiment was conducted to find the probability of overlapping spikes in a simulated MSNA signal. In our simulation, we used thirty spikes in each MSNA burst (this number (i.e., 30 spikes) was used based on preliminary results in our lab that shows the number of spikes per bursts can be in the range of 5 to 45 spikes/burst). The shape and amplitude of these thirty spikes were similar and the duration of each spike was fixed at 3.2 ms. Each spike fired independently at the mean frequency rate and firing probability mentioned above. The multi-fibre signal was constructed by adding the activity of the all spikes. Then, the probability of overlapping spikes (i.e., the time difference between the arrival times of the two spikes ≤ 2 ms) and the probability of the complete overlap (i.e., the

time difference between the arrival times of the two spikes ≤ 0.3 ms) were calculated. The simulation was repeated 100,000 times.

We also tested the performance of our algorithm on overlapping spikes using a simulated signal. Using the two spike templates extracted from two subjects (see Fig. 3.3I), we generated a simulated signal with 32 overlapping spikes. The time difference between the arrival time of these two spikes was altered from 3.2 ms (i.e., no overlap) to 0 (i.e., complete overlap). The neural noise was generated and added to the simulated signal with the method explained in section (3.2.5) and the simulated signal underwent spike detection.

3.2.8 Validation using lower body negative pressure protocol

We applied the new MWD method for detecting spikes in actual recordings of MSNA data. Using the method described in section (3.2.1), MSNA recordings during baseline, -40 and -60 mmHg of lower-body negative-pressure suction (LBNP) were recorded in the same seven healthy participants. LBNP was used to increase the sympathetic activity via baroreflex unloading. Data segments, each 60 s in length, were extracted from base-line and each level of LBNP. The activity in the integrated MSNA was quantified by counting the number of bursts per minute (burst rate) and burst area rate. For the same time segments, the matched wavelet designed in section 3.3.1 was used for spike detection and the spike rate (spikes/min) was calculated in each physiological state (e.g., baseline, -40 and -60 LBNP). The spike rate was compared to burst rate and burst area rate using linear regression. The Pearson correlation coefficient (r) was used to quantify the goodness of fit.

3.3 Results

3.3.1 Matching a wavelet to the mean action potential template

The results of matching the magnitude spectra and group delay of the wavelet to that of a mean action potential template are shown in Fig. 3.5B and 3.5C, respectively. Notice that the matched wavelet magnitude spectra and group delay matches the mean action potential magnitude spectra and group delay very well in the passband. The matched wavelet and the mean action potential template are shown in Fig. 3.5D; the matched wavelet is very similar to the mean action potential template and does have the required structure of a wavelet. Please compare the new designed matched wavelet to the “Symlet 7” shown in chapter 2.

The matched wavelet using the CWT method was applied to the real MSNA signal using the technique described in section 3.2.3. The result of detecting action potentials in one burst of MSNA signal is shown in Fig. 3.6 (A-F). Notice the sharp and tall wavelet coefficient peaks (near to one) around several action potentials labeled by an expert user and compare it with other wavelet coefficients related to the noise (see Fig. 3.6C). As mentioned in section 3.2.3 the location of these action potentials can be determined by finding the largest suprathreshold wavelet coefficient after wavelet thresholding (see Fig. 3.6D, filled circles). Finally, action potentials are extracted using estimated locations centered into a 32 point window from the original filtered MSNA signal. It can be observed that spikes with different amplitudes were extracted using the new method (see Fig. 3.6E).

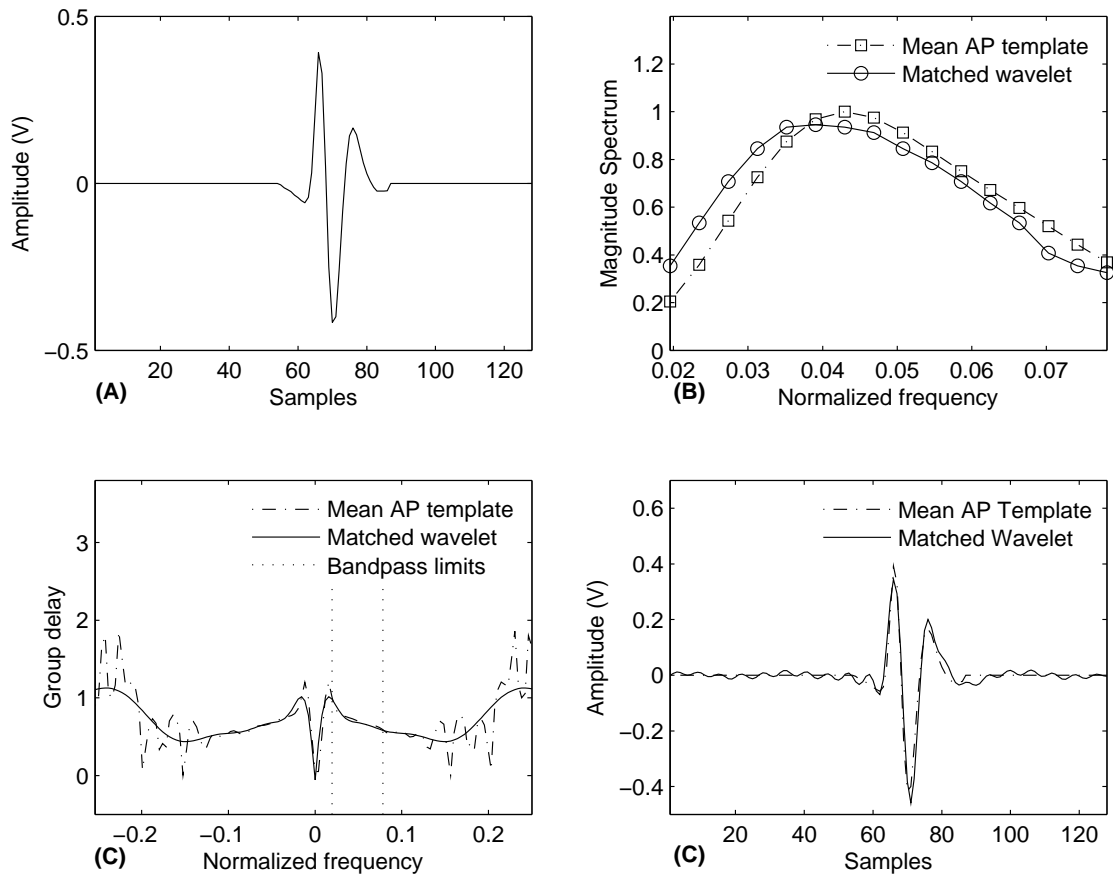


Figure 3.5: Designing a wavelet match to the mean action potential template, (A) An actual mean action potential template. (B) Spectrum amplitude match in the passband. matched wavelet (circle-solid line) versus mean action potential template (square-dash dotted line) (C) Matched wavelet group delay (solid line) versus mean action potential group delay (dash dotted line) (vertical dotted lines show passband). (D) Matched wavelet versus mean action potential template.

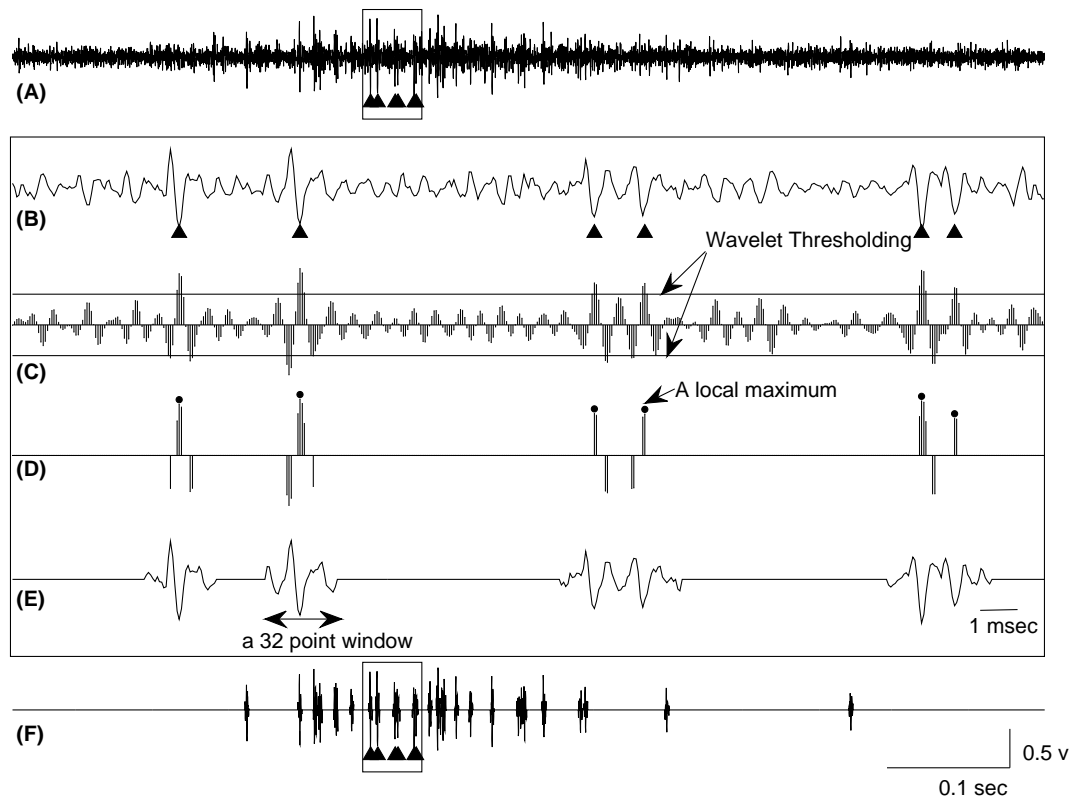


Figure 3.6: Performance of the new action potential detection method on the real MSNA signal. (A) One burst of MSNA (0.8 sec). (B) An enlarged portion of the signal in A (shown with a rectangle) where several action potentials are labeled using triangles by an expert user. (C) Wavelet coefficients using matched wavelet, horizontal lines show the wavelet thresholds estimated from the wavelet coefficients. Notice to the sharp and tall peaks (near to one) around labeled action potentials. (D) The wavelet coefficients related to the labeled action potentials after wavelet thresholding. The local maxima shows the location of the action potentials (shown with filled circles). (E) These action potentials are extracted from B by using the estimated location centered at a 32 points window. (F) All extracted action potentials from A.

3.3.2 Evaluation of detection performance using simulated data

Mean results for the simulations with varied noise levels are displayed in Fig. 3.7. Of note, the MWD produced a higher the percentage of correct detection (PCD) of action potentials and lowest the percentage of false positive alarms (PFP) for all SNRs in three simulations. The DWT has the lowest PCD and highest PFP during all simulation which confirms previous results [28, 47]. While the SWT has a comparable PFP to the MWD for the $\text{SNR} > 3$, its PFP increases rapidly as the SNR decreases.

Major improvements in all three simulations are observed with the MWD, and these include the lowest false positive alarms ($3 \pm 2\%$), a $94 \pm 2\%$ decrease in PFP compared to DWT, a $50 \pm 41\%$ decrease in PFP compared to SWT, a $83 \pm 97\%$ increase in PCD compared to the DWT and a $44 \pm 55\%$ increase in PCD compared to the SWT. These numbers are averaged values that were calculated for all SNRs with three simulations per SNR.

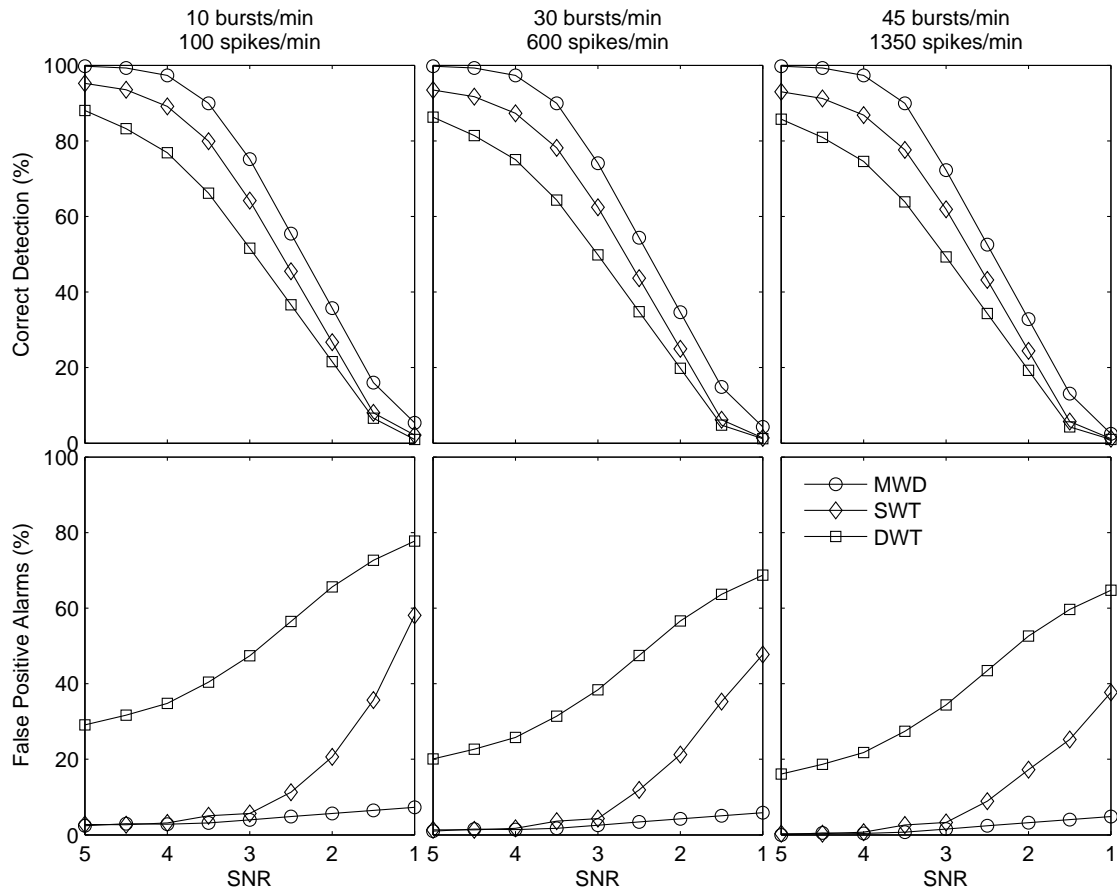


Figure 3.7: Mean results for simulations with varied noise levels, mean burst rate and action potential rate. The simulations tested the performance of DWT decomposition with modified thresholds, SWT decomposition with modified thresholds and the new matched wavelet detector (MWD). Each point on each curve represents the mean result of 50 simulations.

3.3.3 Performance evaluation of the algorithm on overlapping spikes

Based on the simulation explained in section 3.2.7, it was observed that overlap occurred when two action potentials fired within ≤ 2 ms. The probability of this timing was around 3%. However, this overlap seldom included complete overlap and two action potentials were still counted. The probability of complete overlap (i.e., time difference less than or equal to 0.3 ms) was 0.28%. Therefore, the probability of the overlapping spikes in the MSNA signal is low - but it can happen.

We found that if the time difference between the arrival times of the two spikes (i.e., the time duration between the two negative peak values of dominant spikes) is 0.3 ms or less, the MWD method detects the overlap spike as one spike. Notice that in this scenario, two spikes almost have complete overlap (i.e., synchronized firing) and produce a compound spike whose amplitude is larger than the original spikes. At 0.4 ms, 0.5 ms and 0.6 ms time difference, the method sometimes finds one spike and sometimes fails to detect any spikes. For the time difference between arrival times equal to 0.7 ms or above, our method found two spikes for each overlapping spikes in the most cases.

Fig. 3.8 demonstrates the performance of the MWD on the five overlapping spikes. Fig. 3.8A shows the original two dominant spikes marked as (1) and (2) where each spike fires five times. The form of five overlapping spikes (i.e., the sum of the two dominant spike trains in Fig. 3.8A) is shown in Fig. 3.8B. The time duration between the two negative peak values of dominant spikes is 1.4 ms, 1.2 ms, 0.8 ms, 0.5 ms and 0.1 ms for the overlap spikes marked as (s1) to (s5), respectively. It can be seen that when two original spikes are superimposed, the resultant spike shape changes. For instance, spike (s5) is the result of two spikes firing simultaneously producing a compound spike with larger amplitude. In contrast, in the case of spike (s4), two spikes almost cancel each other and produce a superimposed spike with a smaller amplitude. The overlapping spike trains with additive neural noise are shown in Fig. 3.8C (The SNR is 4). Fig. 3.8D shows the estimated locations of overlap spikes (i.e., the local maxima of wavelet coefficients after thresholding). Notice that the MWD detects the original

locations of spikes for the overlap spikes of s_1 , s_2 and s_3 . For spikes (s_4) and (s_5) only one spike is detected (i.e., the MWD misses one spike).

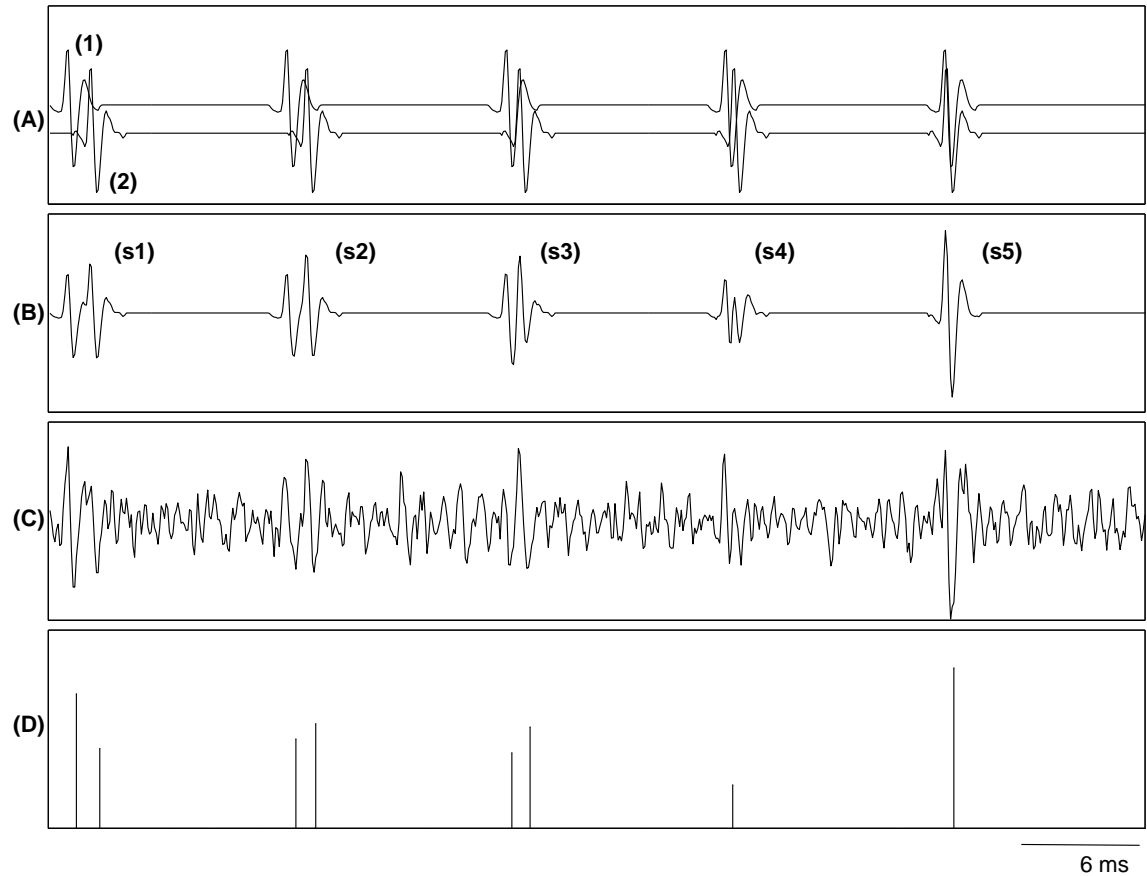


Figure 3.8: Performance of the MWD method to the overlapping spike signal. (A), (B) and (C) Show the original spike signals, their sum and the signal with simulated noise, respectively and (D) Shows the detected spike events. Notice that the MWD detects two spikes for the overlap spikes s1, s2 and s3 but it only detects one spike for overlap spikes s4 and s5 (i.e., it misses one spike.)

3.3.4 Validation using lower body negative pressure protocol

Fig. 3.9 illustrates individual data reflecting a good correlation between the number of bursts per minute and the number of detected spikes per minute (Fig. 3.9A, $r=0.86$) and burst area rate (Fig. 3.9B, $r=0.89$) for seven healthy subjects. Notice the increase in both the average burst rate and spike rate (Fig. 3.9C) and burst area rate (Fig. 3.9D) as the LBNP level was increased and the sympathetic nervous system was activated for each subject.

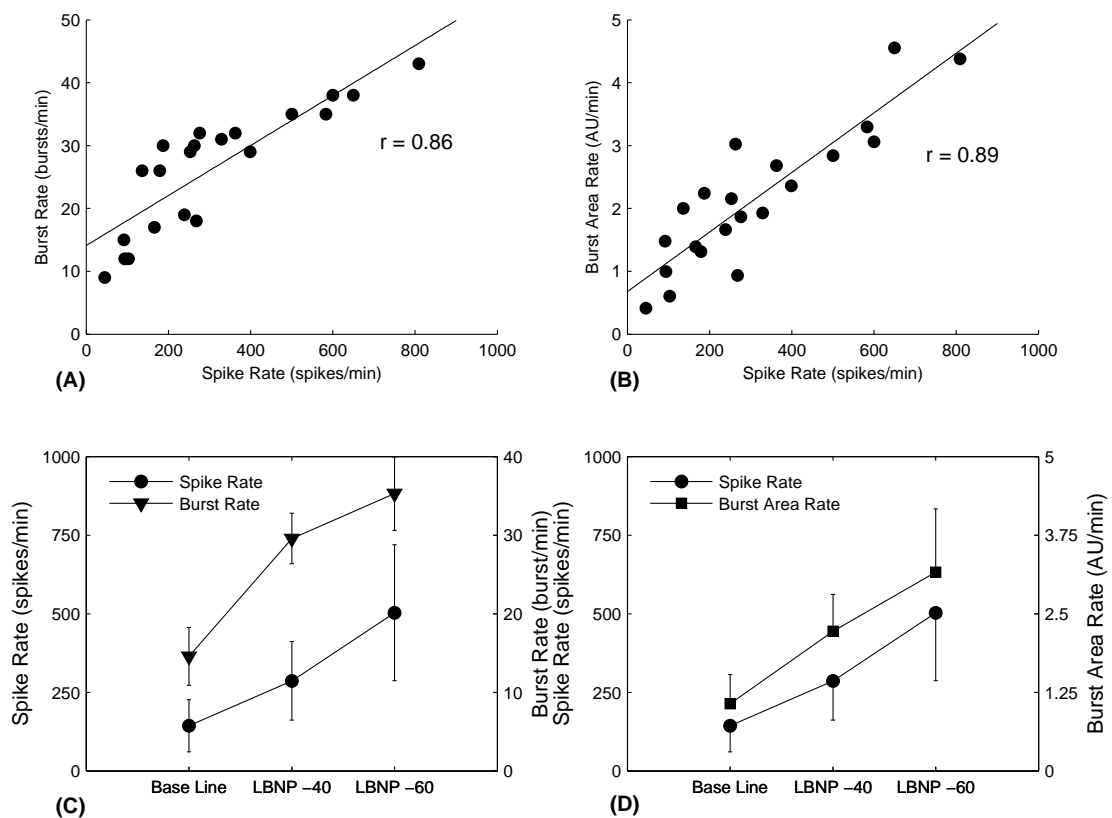


Figure 3.9: Comparison of spike detection and burst parameters during a lower body negative pressure (LBNP) protocol. (A) mean spike rate vs. mean burst rate. (B) mean spike rate vs. mean burst area rate. The mean spike rate demonstrates the same general increasing pattern as the mean burst rate (C) and mean burst area rate (D) as LBNP level is increased.

3.4 Discussion

A new method for detecting action potentials in human muscle sympathetic nerve activity was presented in this paper. The novelty of this method was based on designing a wavelet matched to an actual mean action potential template in order to improve the detection performance of wavelet based techniques. Also, a new method was introduced for simulating artificial MSNA data using statistical properties of the actual MSNA recordings. The performance of the new action potential detection method was compared with two commonly accepted wavelet-based methods (the DWT and SWT with “Symlet 7” as the mother wavelet) using the simulated MSNA data. The new method improved detection performance over the DWT and the SWT methods in terms of an increase in correctly detected action potentials and a considerable reduction in false positive alarms. These features produce an analytical approach that is appropriate for studying human MSNA signal. We also tested the performance of the MWD method on overlapping spikes. It was observed that if the time difference between the arrival times of the two spikes is ≥ 0.7 ms, the MWD method detects the overlap spike as two spikes.

In this study, we have improved our spike detection model by optimizing the mother wavelet for wavelet analysis of human MSNA signal. We used a modified threshold during performance analysis for all the new and two previous methods. This modified threshold is not an optimized choice and better wavelet threshold estimator such as Bayesian methods [49–51] or kurtosis methods [26] can be used; these may provide an improved threshold and, therefore, enhanced performance. Nonetheless, the current study has produced major improvements provided by the matched wavelet approach and has left the problem of determining an optimized threshold for future study.

Since, all MSNA data in our study were recorded with one device (e.g., nerve traffic analysis system (662C-3, Bioengineering of University of Iowa, Iowa City, IA)), only one mother wavelet was designed from five healthy subjects and was used during performance analysis and evaluation of the new method. However, any new hardware or filter software may change the measured action potential waveforms. The advantage of the method proposed here is that

the MWD can be designed for each independent study or laboratory. Spike templates for constructing the new mother wavelet can be either extracted and averaged manually or extracted using the method explained in (3.2.4). The procedure for designing a mother wavelet explained in section (3.5) can be used for matching the new wavelet. A numerically fast implementation of the matching algorithm can be found in the original paper [see 37]. Alternatively, if the frequency response of the new hardware is available, then filtering the matched wavelet designed in this paper by ratio of the frequency response of the new and old hardware can provide the new matched wavelet template.

While designed for human sympathetic action potentials, an advantage of this new method is that it may be applicable for spike detection in other extracellular recordings (e.g., renal sympathetic nerve activity (RSNA) in rats) without any major assumption. The only requirement is a mean action potential template for the target signal and the rest of the algorithm should work in the same way. However, this has not yet been investigated.

In conclusion, the proposed matched wavelet action potential detector has provided a methodological advance that exposes spikes in sympathetic neurograms obtained from humans. Potentially, this MWD is a powerful method to expose action potentials and, thereby, enable studies that aim to understand recruitment strategies used by the sympathetic nervous system, how these strategies are controlled and how they are mechanistically involved in cardiovascular control or pathology.

Acknowledgments

The authors gratefully acknowledge Craig Steinback, Charlotte Willemina Usselman, Ruma Goswami, Yingchun Liu and Maria Frances for preparing the real MSNA data. This work was supported by research grants from the Natural Sciences and Research Council of Canada (NSERC) and the Canadian Institutes of Health Research (CIHR) to K. Shoemaker.

3.5 Appendix A: Algorithms for designing a matched wavelet

3.5.1 Wavelet analysis and pattern detection

In a wavelet decomposition, a signal, $f(x)$, is decomposed into a sum of weighted wavelets [52, 53].

$$f(x) = \sum_{j=0}^{\infty} \sum_{k=-\infty}^{\infty} d_k^j \psi_{j,k}(x) \quad (3.8)$$

where the wavelet coefficients can be calculated as follows

$$d_k^j = \langle f(x), \psi_{j,k}(x) \rangle \quad (3.9)$$

where $\langle \cdot, \cdot \rangle$ stands for the inner product and the wavelets, $\psi_{j,k}(x) = 2^{-j/2} \psi(2^{-j}x - k)$, have the properties of the mother wavelet function, $\psi(x) = \psi_{0,0}(x)$.

In theory of signal detection, one approach for using the wavelet coefficients to detect patterns in a signal is designing a wavelet that matches the signal of interest. Then, one may look for the maximum energy coefficient in the wavelet coefficients at each scale to find the location of patterns.

The projection equation for the wavelet coefficients, given in (3.9), is an inner product summation (in the discrete case) and can be rewritten in the frequency domain applying Parseval's identity [54]

$$d_k^j = \langle f(x), \psi_{j,k}(x) \rangle = \langle F(\omega), \Psi_{j,k}(2^j \omega) \rangle \quad (3.10)$$

where $\Psi_{j,k}(2^j \omega) = 2^{j/2} e^{-i2^j \omega k} \Psi(2^j \omega)$, is the Fourier transform of $\psi_{j,k}(x)$. The energy of d_k^j at a particular scale, j_0 , and translation, k_0 , is given by its squared magnitude

$$|d_{k_0}^{j_0}|^2 = |\langle F(\omega), \Psi_{j_0, k_0}(2^{j_0} \omega) \rangle|^2 \quad (3.11)$$

Applying the Cauchy-Schwarz inequality to the right side of (3.11) gives

$$\begin{aligned} |\langle F(\omega), \Psi_{j_0, k_0}(2^{j_0}\omega) \rangle|^2 &\leq \\ \langle F(\omega), F(\omega) \rangle \langle \Psi_{j_0, k_0}(2^{j_0}\omega), \Psi_{j_0, k_0}(2^{j_0}\omega) \rangle \end{aligned} \quad (3.12)$$

where the equality holds for

$$F(\omega) = K\Psi_{j_0, k_0}(2^{j_0}\omega) \quad (3.13)$$

where both F and Ψ are complex spectra. Therefore, $|d_{k_0}^{j_0}|^2$ is maximized when the complex frequency spectrum of ψ_{j_0, k_0} is identical to that of $f(x)$. Rewriting (3.13) in terms of amplitude and phase gives

$$|F(\omega)|e^{i\theta_F(\omega)} = K2^{j_0/2}|\Psi(2^{j_0}\omega)|e^{i(\theta_\Psi(2^{j_0}\omega)-2^{j_0}\omega k_0)} \quad (3.14)$$

where $\theta_F(\omega)$ and $\theta_\Psi(\omega)$ are the phase of $F(\omega)$ and $\Psi(\omega)$, respectively. This result provides the need for a wavelet matched to a signal of interest in both magnitude and phase.

3.5.2 Conditions for an orthonormal multiresolution analysis

A special case of wavelet analysis is orthonormal multiresolution analysis (MRA), where the following condition is satisfied [54]:

$$\begin{aligned} \langle \phi_{j,k}, \phi_{j,m} \rangle &= \delta_{k,m} \\ \langle \phi_{j,k}, \psi_{j,m} \rangle &= 0 \\ \langle \psi_{j,k}, \psi_{j,m} \rangle &= \delta_{j,l} \cdot \delta_{k,m} \end{aligned} \quad (3.15)$$

where $\delta(\cdot)$ denotes the Kronecker delta function, $\phi(x) = \phi_{0,0}(x)$ is called the scaling function and $\phi_{j,k}(x) = 2^{-j/2}\phi(2^{-j}x - k)$. The wavelets and the scaling functions form an orthonormal basis for continuous functions [54].

3.5.3 Matching discrete spectrum magnitude

Matching the spectrum magnitude of the wavelet to that of the signal of interest is implemented in the discrete domain and begins by taking the Fourier transform of (3.15) (first line) which gives the Poisson summation,

$$\sum_{m=-\infty}^{\infty} |\Phi(\omega + 2\pi m)|^2 = 1. \quad (3.16)$$

Equation (3.16) is a key for finding a wavelet that satisfies (3.15). The only requirement is to find the scaling function from the wavelet. A relationship between the scaling function and the wavelet function can be found by using a pair of quadrature mirror filters, h (lowpass filter) and g (high pass filter) as suggested by Mallat [52]. The following condition of the Fourier transform of h and g must be satisfied [52, 53].

$$|H(\omega)|^2 + |G(\omega)|^2 = 1 \quad (3.17)$$

The filters, h and g , are related to the mother wavelet, $\psi(x)$, and the scaling function, $\phi(x)$, in the frequency domain as follows:

$$\begin{aligned} \Phi(\omega) &= H\left(\frac{\omega}{2}\right)\Phi\left(\frac{\omega}{2}\right) \\ \Psi(\omega) &= G\left(\frac{\omega}{2}\right)\Phi\left(\frac{\omega}{2}\right) \end{aligned} \quad (3.18)$$

Let $\Phi(k\Delta\omega)$ and $\Psi(k\Delta\omega)$ be the sampled scaling function and wavelet spectra, respectively, with the sampling frequency $\Delta\omega = \pi/2^l$. From (3.18) and (3.17) the following closed form solution for finding the scaling function from the wavelet function can be found [37]:

$$|\Phi\left(\frac{\pi k}{2^l}\right)|^2 = \sum_{p=0}^l |\Psi\left(\frac{\pi k}{2^{p-1}}\right)|^2 \quad (3.19)$$

By replacing (3.19) into the Poisson summation (3.16), the necessary and sufficient condition on Ψ (Fourier transform of the wavelet) that guarantees an orthonormal MRA can be derived

as follows [37]:

$$\sum_{m=-\infty}^{\infty} \sum_{p=0}^l Y\left(\frac{2^l}{2^p}(k + 2^{l+1}m)\right) = 1 \quad (3.20)$$

where $Y(k) = |\Psi(k\Delta\omega)|$ contains the samples of spectrum of the wavelet. To find a closed form solution in (3.20), the band of the wavelet was limited to the $2\pi/3 \leq |\omega| \leq 8\pi/3$ (wavelet pass-band) [37], and so the argument of the (3.20) is limited to $2^{l-1}/3 < |\frac{2^l}{2^p}(k + 2^{l+1}m)| < 2^{l+2}/3$. Because of designing real wavelet, the spectra of the wavelet is only matched for positive frequency indices, k , in the passband (i.e., $|\Psi(k\Delta\omega)| = |\Psi(-k\Delta\omega)|$). The conditions in (3.20) generate a set of L linear equality constrains in $Y(k)$ of the form

$$\sum_{i=1}^L \alpha_{ik} Y(k) = 1 \quad k = \{\lceil 2^l/3 \rceil, \dots, \lfloor 2^{l+2}/3 \rfloor\} \quad (3.21)$$

and in vector notation as

$$\mathbf{A}\mathbf{Y} = \mathbf{1} \quad (3.22)$$

where $\mathbf{A} = \{\alpha_{ik}\}$ and $\mathbf{1}$ is a vector of 1's with length L .

Let $\mathbf{W} = |F(k\Delta\omega)|^2$ and $\mathbf{Y} = |\Psi(k\Delta\omega)|^2$ be vectors containing the samples of spectrum of the desired signal and the matched wavelet in the passband, respectively. The problem of finding the optimal wavelet power spectrum amplitude with respect to the desired input spectrum amplitude is given as follows

$$\min_{\mathbf{Y}} \left\{ \frac{(\mathbf{W} - \mathbf{Y})^T (\mathbf{W} - \mathbf{Y})}{\mathbf{W}^T \mathbf{W}} \right\} \quad (3.23)$$

and satisfying the equality constrains (3.22).

3.5.4 Matching discrete spectrum phase

The first half of the problem shown in (3.14) has been solved, the next set of equations provides a closed form solution for finding group delay (negative derivative of the phase) of the matched wavelet from the group delay of the signal of interest. By repeated substitutions of

the equations in (3.18) and assuming $G(\omega) = e^{i\omega} \overline{H(\omega + \pi)}$, the following infinite products can be calculated [52–54]:

$$\Psi(\omega) = e^{-i\frac{\omega}{2}} \overline{H(\frac{\omega}{2} + \pi)} \prod_{m=2}^{\infty} H(\frac{\omega}{2^m}) \quad (3.24)$$

Taking the phase of both sides gives

$$\theta_{\Psi} = -\frac{\omega}{2} - \theta_H(\frac{\omega}{2} + \pi) + \sum_{m=2}^{\infty} \theta_H(\frac{\omega}{2^m}) \quad (3.25)$$

where θ_{Ψ} and θ_H are the phases of Ψ and H , respectively, and θ_H is 2π -periodic. The negative of the group delay can be found by taking the derivative of the (3.25) as follows:

$$\Gamma_{\Psi}(\omega) = -\frac{1}{2} \lambda(\frac{\omega}{2} + \pi) + \sum_{m=2}^{\infty} 2^{-m} \lambda(\frac{\omega}{2^m}) \quad (3.26)$$

where $\Gamma_{\Psi}(\omega) = d\theta_{\Psi}(\omega)/d\omega + 1/2$ and $\lambda(\omega) = d\theta_H(\omega)/d\omega$ are all even function.

The group delay of the desired signal is then matched with (3.26). Let $\mathbf{\Gamma}_F$ and $\mathbf{\Gamma}_{\Psi}$ be vectors containing the samples of the group delay of the desired signal and the matched wavelet, respectively. The optimal group delay of the matched wavelet is the solution of

$$\min_{\mathbf{\Gamma}_{\Psi}} \{(\mathbf{\Gamma}_F - \mathbf{\Gamma}_{\Psi})^T (\mathbf{\Gamma}_F - \mathbf{\Gamma}_{\Psi})\} \quad (3.27)$$

and $\lambda(\omega)$ has to be 2π -periodic in (3.26).

The optimal group delay of the matched wavelet, $\mathbf{\Gamma}_{\Psi}$, can be summed to provide the discrete phases of matched wavelet and when combined with the magnitude of the matched wavelet provide the full estimate of the discrete matched wavelet spectrum ($\Psi(n\Delta\omega)$). By taking inverse Fourier transform the discrete matched wavelet $\psi(k\Delta x)$ can be calculated in time domain.

References

- [1] B. G. Wallin and N. Charkoudian, "Sympathetic neural control of integrated cardiovascular function: insights from measurement of human sympathetic nerve activity," *Muscle and Nerve*, vol. 36, pp. 595-614, 2007.
- [2] J. S. Floras, "Sympathetic activation in human heart failure: Diverse mechanisms, therapeutic opportunities," *Acta physiologica scandinavica* vol. 177, pp. 391-398, 2003.
- [3] V. G. Macefield, B. Rundqvist, Y. B. Sverrisdottir, B. G. Wallin, and M. Elam, "Firing properties of single muscle vasoconstrictor neurons in the sympathoexcitation associated with congestive heart failure," *Circulation* vol. 100, pp. 1708-1713, 1999.
- [4] M. Elam and V. Macefield, "Multiple firing of single muscle vasoconstrictor neurons during cardiac dysrhythmias in human heart failure," *J Appl Physiol* vol. 91, pp. 717-724, 2001.
- [5] M. Esler, "The sympathetic system and hypertension," *Amer J Hypertens* vol. 13, pp. 99S-105S, 2000.
- [6] D. A. Mary and J. B. Stoker, "The activity of single vasoconstrictor nerve units in hypertension," *Acta Physiologica Scandinavica* vol. 177, pp. 367-376, 2003.
- [7] K. E. Hagbarth and A. B. Vallbo, "Pulse and respiratory grouping of sympathetic impulses in human muscle nerves," *Acta physiologica scandinavica* vol. 74, pp. 96-108, 1968.
- [8] B. G. Wallin, D. Burke and S. Gandevia, "Coupling between variations in strength and baroreflex latency of sympathetic discharges in human muscle nerves," *J Physiol*, vol. 474, pp. 331-338, 1994.
- [9] M. Abeles, M. H. Goldstein, "Multispikes train analysis," *Proceedings of The IEEE* vol. 65, pp. 762-773, 1977.

- [10] X. Yang, S. A. Shamma, "A totally automated system for the detection and classification of neural spikes," *IEEE Trans Biomed Eng* vol. 35, pp. 806-816, 1988.
- [11] A. F. Atiya, "Recognition of multiunit neural signals," *IEEE Trans Biomed Eng*, vol. 39, pp. 723-729, 1992.
- [12] I. N. Bankman, K. O. Johnson, W. Schneider, "Optimal detection, classification and superposition resolution in neural waveform recordings," *IEEE Trans Biomed Eng* vol. 40, pp. 836-841, 1993.
- [13] M. Lewicki, "Bayesian modeling and classification of neural signals," *Neural Comput* vol. 6, pp. 1005-30, 1994.
- [14] M. Lewicki, "A review of methods for spike sorting: the detection and classification of neural action potentials," *Comput Neural Syst* vol. 9, pp. R53-R78, 1998.
- [15] E. V. Goodall, K. W. Horch, "Separation of action potentials in multiunit intrafascicular recordings," *IEEE Trans Biomed Eng* vol. 39, pp. 289-295, 1992.
- [16] D. Stashuk, Y. Qu, "Adaptive motor unit action potential clustering using shape and temporal information," *Med Biol Eng Comput*, vol. 34, pp. 41-49, 1996.
- [17] J. C. Letelier, P. P. Weber, "Spike sorting based on discrete wavelet transform coefficients," *J Neurosci Methods* vol. 101, pp. 93-106, 2000.
- [18] H. Nakatani, T. Watanabe, N. Hoshimiya, "Detection of nerve action potentials under low signal-to-noise ratio condition," *IEEE Trans Biomed Eng* vol. 48, pp. 845-9, 2001.
- [19] K. G. Oweiss, D. J. Anderson, "Spike sorting: a novel shift and amplitude invariant technique," *Neurocomput* vol. 44-46, pp. 1133-9, 2002.
- [20] K. H. Kim, S. J. Kim, "A wavelet-based method for action potential detection from extracellular neural signal recording with low signal-to-noise ratio," *IEEE Trans Biomed Eng* vol. 50, pp. 999-1011, 2003.

- [21] Z. Nenadic and J. W. Burdick, "Spike Detection Using the Continuous Wavelet Transform," *IEEE Trans Biomed Eng* vol. 52, pp. 74-87, 2005.
- [22] L. Citi, J. Carpaneto, K. Yoshida, K. P. Hoffmann, K. P. Koch, P. Dario, "On the use of wavelet denoising and spike sorting techniques to process electroneurographic signals recorded using intraneural electrodes," *J Neurosci Methods* vol. 172, pp. 294-302, 2008.
- [23] D. L. Donoho, "Ideal spatial adaptation by wavelet shrinkage," *Biometrika* vol. 81, pp. 425-455, 1994.
- [24] D. L. Donoho, "De-noising by soft-thresholding," *IEEE Trans Inf Theory* vol. 41, pp. 613-627, 1995.
- [25] A. Diedrich, W. Charoensuk, R. J. Brychta, A. C. Ertl and R. Shiavi, "Analysis of raw microneurographic recordings based on wavelet de-noising technique and classification algorithm: Wavelet analysis in microneurography," *IEEE Trans Biomed Eng* vol. 50, pp. 41-50, 2003.
- [26] R. J. Brychta, R. Shiavi, D. Robertson, A. Diedrich, "Spike detection in human muscle sympathetic nerve activity using the kurtosis of stationary wavelet transform coefficients," *J Neurosci Meth* vol. 160, pp. 359-367, 2007.
- [27] A. Salmanpour, L. J. Brown and J. K. Shoemaker, "Detection and Classification of Raw Action Potential Patterns in Human Muscle Sympathetic Nerve Activity," *Conf Proc IEEE Eng Med Biol Soc*, vol. 2008, pp. 2928-31, 2008.
- [28] A. Salmanpour, L. J. Brown and J. K. Shoemaker, "Performance Analysis of Stationary and Discrete Wavelet Transform for Action Potential Detection from Sympathetic Nerve Recordings in Humans," *Conf Proc IEEE Eng Med Biol Soc*, vol. 2008, pp. 2932-5, 2008.
- [29] O. T. Can, J. A. Taylor, A. Ler, M. A. Cohen, "Detection of Multifiber Neuronal Firings:

- A Mixture Separation Model Applied to Sympathetic Recordings,” *IEEE Trans Biomed Eng* vol. 56, pp. 147-158, 2009.
- [30] A. H. Tewfik, D. Sinha, P. Jorgensen, “On the optimal choice of a wavelet for signal representation,” *IEEE Trans Inf Theory*, vol. 38, pp. 747-765, 1995.
- [31] D. Farina, O. F. Nascimento, M. F. Lucas, C. Doncarli, “Optimization of wavelets for classification of movement-related cortical potentials generated by variation of force-related parameters,” *J Neurosci Methods* vol. 162, pp. 357-363, 2007.
- [32] D. Farina, E. N. Kamavuako, J. Wu, F. Naddeo, “Entropy-Based Optimization of Wavelet Spatial Filters,” *IEEE Trans Biomed Eng* vol. 55, pp. 914-922, 2008.
- [33] E. N. Kamavuako, W. Jensen, K. Yoshida, M. Kurstjens, D. Farina, “A criterion for signal-based selection of wavelet for denoising intrafascicular nerve recordings,” *J Neurosci Methods* vol. 186, pp. 274-280, 2010.
- [34] H. Szu, Y. Sheng, J. Chen, “Wavelet transform as a bank of the matched filters,” *Applied Optics*, vol. 31, pp. 3267-3277, 1992.
- [35] F. Laterza, G. Olmo, “Analysis of EMG signals by means of the matched wavelet transform,” *IEE Electronics Letters* vol. 33, pp. 357-359, 1997.
- [36] G. Olmo, F. Laterza, L. L. Presti, “Matched wavelet approach in stretching analysis of electrically evoked surface EMG signal,” *Signal Processing* vol. 80, pp. 671-684, 2000.
- [37] J. O. Chapa and R. M. Rao, “Algorithms for Designing Wavelets to Match a Specific Signal,” *IEEE Trans Signal Process* vol. 48, pp. 3395-3406, 2000.
- [38] R. C. Guido, J. F. Slaets, R. K. Koberle, L. O. Almeida, J. C. Pereira, “A new technique to construct a wavelet transform matching to a specified signal with applications to digital, real time, spike, and overlap pattern recognition,” *Signal Processing* vol. 16, pp. 24-44, 2006.

- [39] L. K. Shark, C. Yu, "Design of matched wavelets based on generalized Mexican-hat function," *Signal Processing*, vol. 86, pp. 1451-1469, 2006.
- [40] A. Salmanpour, L. J. Brown and J. K. Shoemaker, "Detection of Single Action Potential in Multi-unit Postganglionic Sympathetic Nerve Recordings in Humans: A Matched Wavelet Approach," *Conf Proc IEEE Acoust Speech Signal Process*, vol. 2010, pp. 554-557, 2010.
- [41] B. G. Wallin, "Sympathetic Microneurography. in Primer on the Autonomic Nervous System, second ed," *Elsevier:Oxford*, pp. 224-227, 2004.
- [42] V. G. Macefield, M. Elam, B. G. Wallin, "Firing properties of single postganglionic sympathetic neurones recorded in awake human subjects," *Auton Neurosci-Basic* vol. 95, pp. 146-159, 2002.
- [43] I. M. Johnstone, B. W. Silverman, "Wavelet threshold estimators for data with correlated noise," *J R Stat Soc* vol. 59, pp. 319-51, 1997.
- [44] J. T. Inglis, J. B. Leeper, D. Burke and S. C. Gandevia, "Morphology of action potentials recorded from human nerves using microneurography," *Exp Brain Res* vol. 110, pp. 308-314, 1996.
- [45] V. G. Macefield and B. G. Wallin, "Firing properties of single vasoconstrictor neurones in human subjects with high levels of muscle sympathetic activity," *J Physiol* vol. 516, pp. 293-301, 1999.
- [46] L. B. Jackson, "Digital Filters and Signal Processing, second ed" *Kluwer Academic Publishers* pp. 255-257, 1989.
- [47] R. J. Brychta, S. Tuntrakool, M. Appalsamy, N. R. Keller, D. Robertson, R. Shiavi and A. Diedrich, "Wavelet methods for spike detection in mouse renal sympathetic nerve activity," *IEEE Trans Biomed Eng* vol. 54, pp. 82-93, 2007.

- [48] C. Pouzat, O. Mazor, G. Laurent, "Using noise signature to optimize spike sorting and to assess neuronal classification quality," *J Neurosci Meth* vol. 122, pp. 43-57, 2002.
- [49] F. Abramovich, T. Sapatinas, B. W. Silverman, "Wavelet thresholding via a bayesian approach," *J R Statis Soc B* vol. 60, pp. 725-749, 1998.
- [50] B. Vidakovic, "Nonlinear wavelet shrinkage with bayes rules and bayes factors," *J Amer Stat Assoc*, vol. 93, pp. 173-179, 1998.
- [51] I. M. Johnstone, B. W. Silverman, "Needles and straw in haystacks: Empirical bayes estimates of possibly sparse sequences," *Ann Stat* vol. 32, pp. 1594-1649, 2004;.
- [52] S. G. Mallat, "A theory for multiresolution signal decomposition: the wavelet representation," *IEEE Trans Pattern Anal Mach Intell* vol. 11, pp. 674-693, 1989.
- [53] I. Daubechies, "Orthonormal Bases of Compactly Supported Wavelets," *Communication on Pure and Applied Mathematics*, vol. 41, pp. 909-996, 1988.
- [54] C. K. Chui, "An introduction to wavelets. in Wavelet Analysis and Its Application," *Academic Press:New York*, vol. 1, pp. 215-236, 1992.

Chapter 4

Relationship between size and latency of action potentials in human muscle sympathetic nerve activity

4.1 Introduction

The first recordings of human post-ganglionic sympathetic nerve recordings were reported by Hagbarth and Vallbo [1], initiating an exciting era in research regarding autonomic outflow and the neural control of the cardiovascular system [2, 3]. Traditionally, due to relatively poor signal-to-noise aspects, analysis of this multi-fiber recording from human peripheral nerves has, to a large extent, been constrained to the integrated neurogram signal through band-pass filtering, rectification and integration. These steps reduce background noise and provide a quantitative measure of sympathetic outflow, but eliminate all action potential information. For instance, the number of action potentials and their morphologies that contribute to a given sympathetic burst are lost during the integration process.

Nonetheless, observations based on the integrated neurogram have led investigators to hypothesize details about the properties of the single neurons that make up the multi-fiber re-

response. For example, variations in the size of the integrated bursts are deemed to reflect recruitment patterns from a pool of axons within the recording field of the electrode; however, uncertainty continues regarding the size of the pool of post-ganglionic sympathetic axons from which variations in recruitment can occur. Also, a provocative observation in human sympathetic recordings is that the conduction of sympathetic traffic, based on the delay of the burst from a representative R-wave of the ECG (Wallin et al. 1994), is inversely related to burst size. As burst size is expected to be related to the number of action potentials occurring within the same burst, the shorter reflex latency of larger bursts is hypothesized to be due to a) variations in synaptic delays between the brain stem and peripheral nerve; that is, more discharges of the same neurons per burst, and/or b) more than one population of efferent sympathetic neurons with progressive recruitment thresholds and conduction velocities [4]. Variations in baroreflex control of burst occurrence versus burst size have led some investigators to postulate different sites of control over these two features (i.e., the number of units recruited within a sympathetic burst) [5]. Macefield and Wallin [6] have provided considerable advances regarding the discharge properties of single sympathetic neurons in humans. These studies indicate that such neurons discharge in a probabilistic manner, typically firing only once in a sympathetic burst [6, 7]. However, multiple within-burst firings of the same neuron occur with increasing stress [6] and with some pathologies [8, 9]. From these studies on single-fibre recordings, Macefield and Wallin [6] have proposed that a) between-individual variations exist in the number of active sympathetic neurons and b) increases in firing probability of active neurons may be the primary mechanism by which burst intensity (size) is augmented.

By analogy, one may consider that properties of excitable neurons are similar across neural systems. For example, recruitment of additional motor units, of increasing size, is the strategy employed during muscular contraction of growing intensity [10, 11]. Here the larger neurons have a higher recruitment threshold (they are not recruited at rest) and, compared with smaller axons, exhibit faster conduction velocities [12]. Moreover, the firing rates of active neurons increases after recruitment [13]. Whether such an ordered pattern is a property of other excitable

nerve systems such as the sympathetic nervous system, remains untested.

To study post-ganglionic sympathetic discharge patterns, we developed a novel technique that enables the identification and morphological classification of multiple vasomotor neurons contributing to sympathetic bursts [14, 15]. This method was applied to human muscle sympathetic nerve activity (MSNA) data obtained at rest and during lower body negative pressure (LBNP) to elicit a wide range of MSNA. Using this approach we tested the hypothesis that variations in human MSNA are related to recruitment of a new population of efferent sympathetic fibres that differ in terms of action potential size and latency. The alternate outcome is that the increase in MSNA is accomplished primarily by increasing the firing probability of low-threshold axons that are present under baseline conditions. Our aim was to extract action potential content from extracellular sympathetic recordings during base-line and LBNP suction of -60 mmHg and classify these action potentials based on their peak-to-peak amplitude. LBNP was used to increase the sympathetic activity via baroreflex unloading to test the role of baroreceptor input in the regulation of action potential recruitment. This approach of action potential classification complements the single-unit approach that has been proposed previously [6, 7] by emphasizing the total number of action potentials per sympathetic burst, and the size of these action potentials, but not how a single axon behaves over time.

4.2 Methods

4.2.1 Subjects

Eight healthy individuals (four males, four females) participated in this study. They were 23 - 30 years in age, 47 - 98 kg in weight and 160 - 188 cm in height. All participants were healthy as determined by a medical questionnaire and family history. The participants provided signed consent to the study procedures and these procedures were approved by the Human Subjects Research Ethics Board at The University of Western Ontario.

4.2.2 Experimental Protocol

Data were obtained from supine individuals during five minutes of baseline and three minutes of LBNP -60 mmHg. Continuous beat-by-beat measurements of mean arterial pressure (MAP) were made with a photoplethysmograph finger cuff (Finometer; Finapres Medical Systems, Amsterdam, The Netherlands) from the middle finger of the right hand. Blood pressures obtained from the Finometer were validated with manual sphygmomanometer blood pressure measurements. Changes in cardiac output (CO) was acquired using the Finometer Modelflow algorithm. Heart rate was measured with a standard lead II electrocardiogram (ECG; Pilot 9200, Colin Medical Instruments, San Antonio, TX). Data were collected on Chart 5 Powerlab data acquisition system (ADInstruments, Colorado Springs, CO).

4.2.3 Sympathetic Neural Recordings

Recordings of MSNA were obtained from the fibular (peroneal) nerve using a 200 μm diameter, 35 mm long tungsten microelectrode tapering to an uninsulated 1 to 5 μm tip. This electrode was inserted percutaneously into the nerve just posterior to the fibular head. A reference electrode was positioned subcutaneously 1-3 cm from the recording site. An MSNA site was obtained by manually manipulating the microelectrode until a characteristic pulse-synchronous burst pattern was observed. The recording site was taken to provide MSNA when a) the burst pattern was not associated with skin paresthesias, b) increased in burst strength in response to voluntary apnea but not during arousal to a loud noise [1], and c) burst probability was inversely related to diastolic blood pressure [16]. Neurograms were measured with a nerve traffic analysis system (662C-3, Bioengineering of University of Iowa, Iowa City, IA). The neural signal was preamplified with a gain of 1000 (using preamplifier and isolation amplifier, gain=100 and 10, respectively) and further amplified with a gain of 75 (using a variable gain amplifier gain=0.1-99). This neuronal activity was then band-pass filtered (bandwidth of 700-2,000 Hz) and the filtered MSNA was rectified and integrated. Integration is accomplished with a leaky integrator set with a 0.1 s time constant. All signals were digitized with a data

acquisition system (PowerLab software, ADInstruments Inc.) at a sampling rate that varied from 100 Hz for the rectified and integrated neurogram to 10 kHz for the amplified and filtered neurogram. Previous work from our laboratory (unpublished) indicates that the band-pass filter settings applied to the raw data do not impair our ability to detect action potential waveforms. However, the impact of signal conditioning, including amplifier characteristics and band-pass filter settings, on action potential morphology requires further assessment.

4.2.4 Integrated MSNA burst Analysis

Integrated bursts of MSNA were identified as exhibiting pulse-synchrony, having an amplitude (i.e, the highest peak of the burst) twice as big as the previous minimum point of the burst, having characteristic rising and falling slopes, and increasing in incidence and size during end-expiratory apnoea but not startle. Burst occurrence was confirmed by visually inspecting the corresponding raw neurogram.

The strength of sympathetic activity was expressed both as number of bursts per 100 heartbeats (burst incidence) and burst per min (burst frequency). In addition, burst size was normalized to the mean amplitude both at rest and during LBNP to account for any electrode repositioning. Reflex latency was determined using the approach introduced by Fagius and Wallin [17] and used frequently since. This process is simply the time delay between the R-wave related to the burst (the previous R-wave in which the burst was observed) and the peak of the burst (the highest point of the integrated MSNA burst). Reflex latency was calculated for each burst and averaged for all detected bursts in each condition and volunteer (mean reflex latency). The baroreflex threshold diagram was used to compare the arterial baroreflex control of MSNA at rest and LBNP -60 mmHg. To do so, diastolic pressures of individual heart beats were grouped in intervals of 1 mmHg and for each interval burst incidence was calculated and plotted against the mean of the pressure interval [16].

4.2.5 Action Potential Detection and Analysis

Action potentials were detected and extracted from the filtered raw MSNA signal using the techniques developed previously [14]. Briefly, this technique uses a continuous wavelet transform (CWT) for action potential detection. The CWT used a “mother wavelet” that was adapted to an actual average action potential waveform constructed from physiological recordings of post-ganglionic sympathetic action potentials (i.e., matched mother wavelet had the same morphology as a physiological sympathetic action potential) [14]. The designing process involves a) detecting action potentials from the filtered raw MSNA signal and averaging them to build a mean action potential template and b) matching the amplitude and the phase of the new mother wavelet to that of the mean action potential template in the frequency domain [14].

The CWT with the matched mother wavelet was applied to the filtered MSNA to provide a wavelet coefficient between the signal of interest (i.e., an action potential) and the mother wavelet such that the wavelet coefficient was largest in the presence of the action potentials and negligible when applied to noise. Wavelet coefficients related to action potentials and noise were separated based on thresholding analysis [14]. The exact location of the negative peak for each action potential was then detected by isolating the largest supra-threshold wavelet coefficient. Using this location information the action potential waveforms were obtained from the original signal by putting the estimated location of action potentials in the center of a predefined window (3.2 ms). In this way, the amplitude and morphology of each extracted action potential remained unaltered. Extracted action potentials were then ordered based on peak-to-peak amplitude and histogram analysis was performed to separate action potentials into amplitude-based clusters based on Scott’s Rule [18]. The Scott’s rule proposes the optimal histogram bin width based on the sample size and an estimate of the standard deviation of the data. As such, the number of total clusters varied by subject.

The signal-to-noise ratio for a period of data was determined as the amplitude of the negative peak of the mean action potential over the standard deviation of the background noise (i.e. during sympathetic silence). Action potential latency was determined as the time delay

between the R-wave of the electrocardiogram related to the burst of action potentials (i.e., the previous R-wave in which the burst of action potentials was observed) and the negative peak of the action potential waveform, similar to that described previously [7].

4.2.6 Action Potential Summation Simulation

A limitation to the study of total action potential content in a burst is the potential problem of action potential summation if two (or more) axons fire simultaneously such that their electrical discharges summate in the neurogram. We have quantified the potential risk of this problem (for detailed explanation see [14]). Using published data from recordings of single post-ganglionic sympathetic axons [6], a simulation analysis was performed to determine the probability of action potential overlap. From these previous data, it was assumed that each axon was active only once within a burst of activity, had a mean firing frequency of 0.33 Hz, and had a firing probability (percentage of heart beats during which a neuron was active) of 35%. The shape and amplitude of each action potential was the same between “neurons” and the duration was fixed at 3.2 ms. A population of 30 simulated “neurons” was used for this simulation. Each “neuron” was active independently from the others. Using these criteria, 10,000,000 simulated bursts of sympathetic activity (containing 1.2×10^8 simulated action potentials) were generated. These data were then assessed for overlapping action potentials. The overlap was calculated based on the distance between the negative peaks of two action potentials where the complete overlap occurred if the distance was ≤ 0.3 ms and partial overlaps were counted if the distance was > 0.3 ms and ≤ 2 ms. Two possible patterns of summation were expected. First, complete superimposition would produce a larger-than expected action potential that would occupy a bin that was not contiguous in the binning designation. Second, incomplete summation would produce an aberrant waveform whose shape and amplitude would be misleading but, nonetheless, composed of two action potentials that could be counted. Thus, action potential clusters were eliminated if they were larger than all others and in a bin that was not contiguous with the remaining data. Further, action potential waveforms that were not tri-phasic and of small

amplitude were also eliminated from the analysis.

4.2.7 Statistical Analysis

Values are given as means \pm STD. The effect of condition (baseline vs LBNP) was assessed using a two-tailed, paired, t test. Probability values < 0.05 were considered statistically significant. Linear regression analysis was used to quantify the relationship between following variables (Burst amplitude vs Burst latency), (Burst Size vs Number of action potentials within a burst), (Burst size vs. Number of unique action potential clusters within a burst) and (Number of action potentials within a burst vs. Number of unique action potential clusters within a burst).

4.3 Results

This section summarizes the result of integrated burst and action potential analyses in sympathetic neural recordings. We divided our data into two different groups. Group (A) contains and compares sympathetic burst parameters and action potential content in MSNA data at baseline and LBNP -60 mmHg for seven subjects (three males, four females)(subject number: 1 to 7). Subject 8 was excluded from this group because a high level of motor unit activity was present only during LBNP -60 mmHg.

Group (B) compares the same parameters in MSNA data at baseline and LBNP -80 mmHg for only two subjects (two males)(subject number: 7 and 8). Because of the difficulty of obtaining the MSNA signal at -80 mmHg, this level of LBNP were recorded only for two subjects. Although subject 8 showed a high level of motor unit activity at LBNP -60 mmHg, clean sympathetic nerve signals (i.e., without motor unit activity) were recorded at baseline and LBNP -80 mmHg.

4.3.1 Baseline vs. LBNP -60 mmHg

Integrated Bursts Analysis

Corresponding filtered raw and integrated MSNA data were obtained for 300 s at baseline and 180 s of steady-state LBNP for burst and action potential analysis. An example of the raw MSNA data at base-line and LBNP -60 mmHg is shown in Figure 4.1. Compared with baseline, burst frequency (14 ± 4 vs. 33 ± 3 bursts.min⁻¹, $P < 0.001$) and burst incidence (24 ± 7 vs. 43 ± 8 burst.100 heart beats⁻¹, $P < 0.001$) were increased at LBNP -60 mmHg. Compared to baseline (0.21 ± 0.08 vs. 0.26 ± 0.09 V; $P < 0.05$ V), mean burst amplitude was increased slightly at LBNP -60 mmHg. In each participant the burst incidence was linearly related to diastolic blood pressure in a manner that was reset to higher sympathetic outflow with LBNP indicating that the sympathetic bursts reflected baroreflex-mediated sympathetic activity (see Figure 4.2). There was a linear relationship between the burst amplitude and corresponding burst reflex latency both at baseline (slope = -0.00082 ± 0.0002 ; $r = -0.5 \pm 0.1$, $P < 0.001$) and LBNP -60 mmHg (slope = -0.00098 ± 0.00029 ; $r = -0.56 \pm 0.13$, $P < 0.001$). Figure 4.3 illustrates this linear relationship for one representative subject at baseline and LBNP -60 mmHg. However, mean reflex latency was not different between baseline and LBNP -60 mmHg (1.28 ± 0.05 s vs. 1.29 ± 0.05 s). The regression line for the linear relationship between burst size and burst latency was used to calculate the mean reflex latency variation between largest and smallest bursts [4]. The mean reflex latency variations (i.e., latency of small - latency of large bursts) were 0.12 ± 0.03 at baseline and 0.12 ± 0.04 at LBNP -60 mmHg.

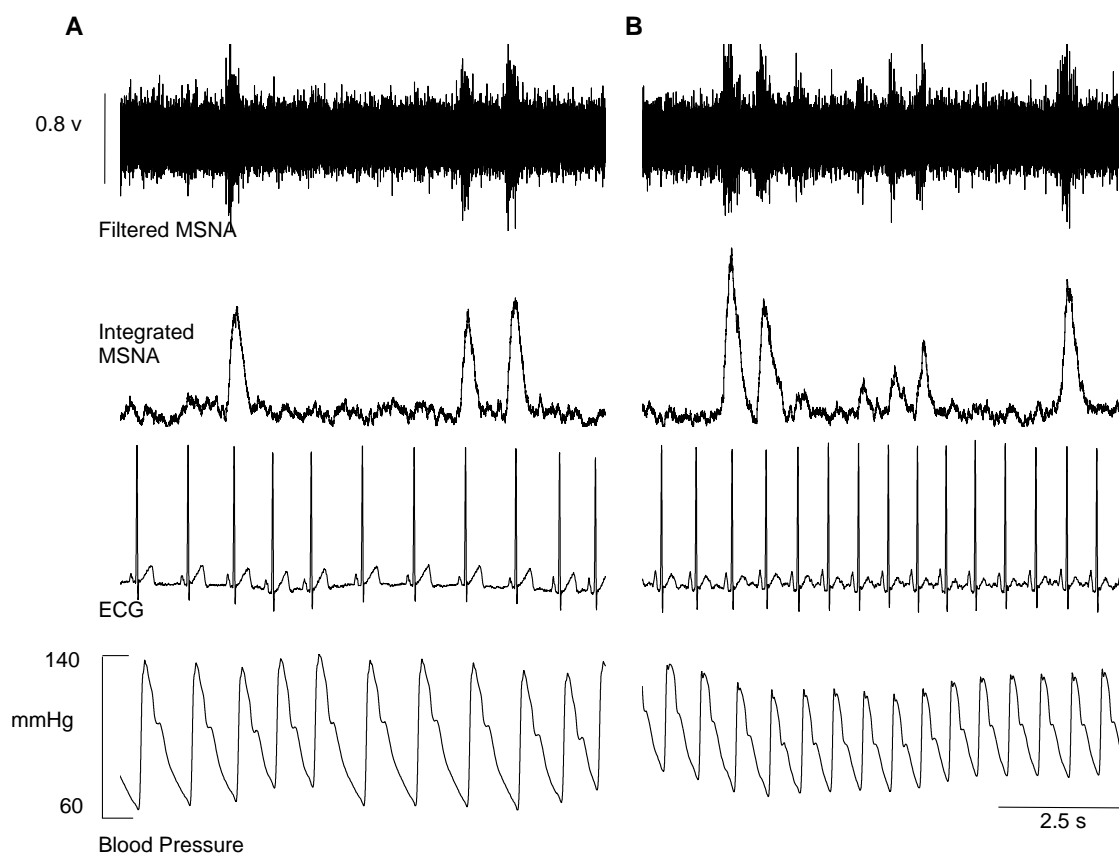


Figure 4.1: A representative example of filtered raw and integrated muscle sympathetic nerve activity. (A) at rest and (B) during LBNP -60 mmHg.

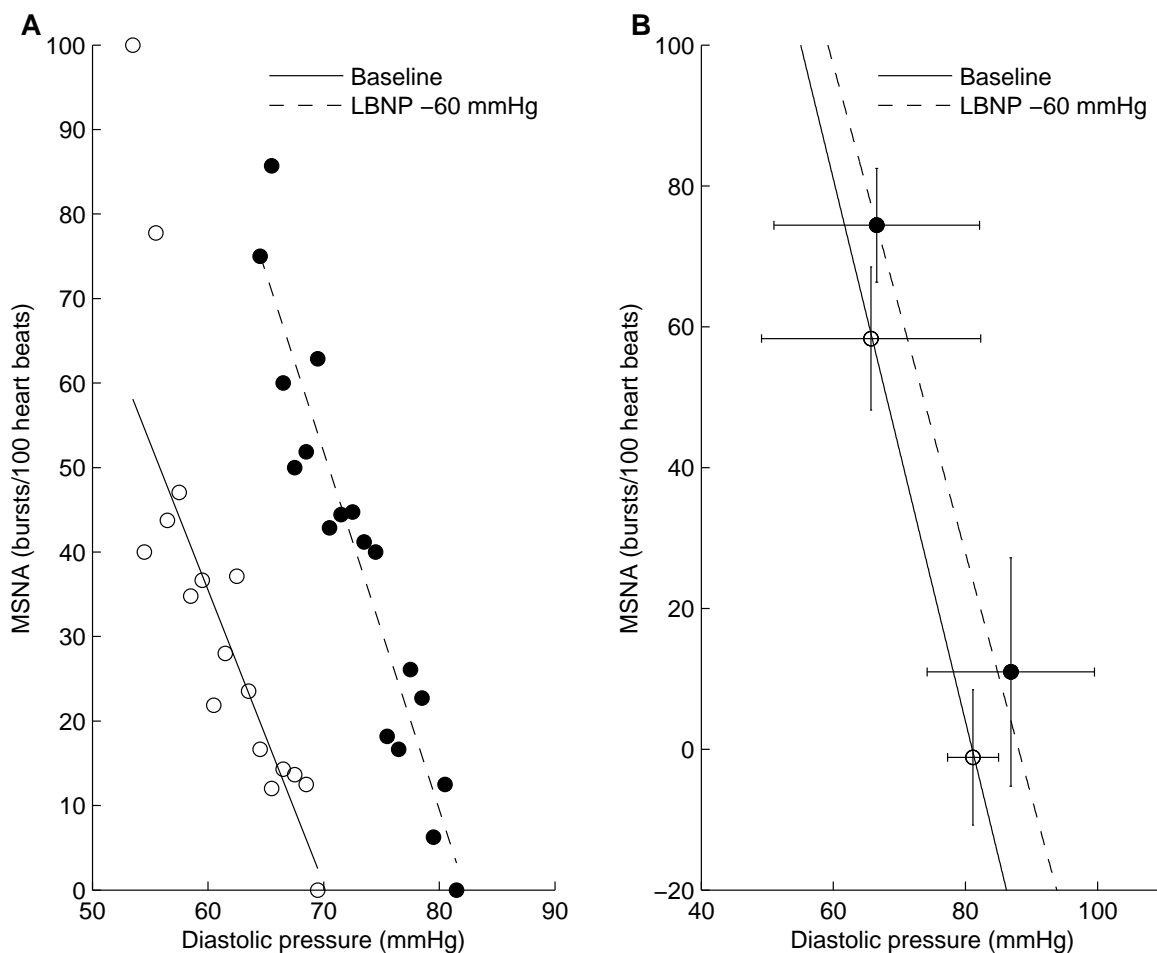


Figure 4.2: The occurrence of sympathetic bursts in relation to diastolic blood pressure. (A) Representative examples of baroreflex threshold diagram from one participant during baseline (circle - solid line) and LBNP -60 mmHg (filled circle - dashed line). (B) Mean baroreflex relations during baseline (circle-line) and LBNP -60 mmHg (filled circle - dashed line) ($n=7$). Mean values are from each subject's lowest and highest diastolic pressure at baseline (circle) and LBNP (filled circle). Error bars indicate SD. Baseline regression: $y = -3.85x + 312$, LBNP regression $y = -3.47x + 305$.

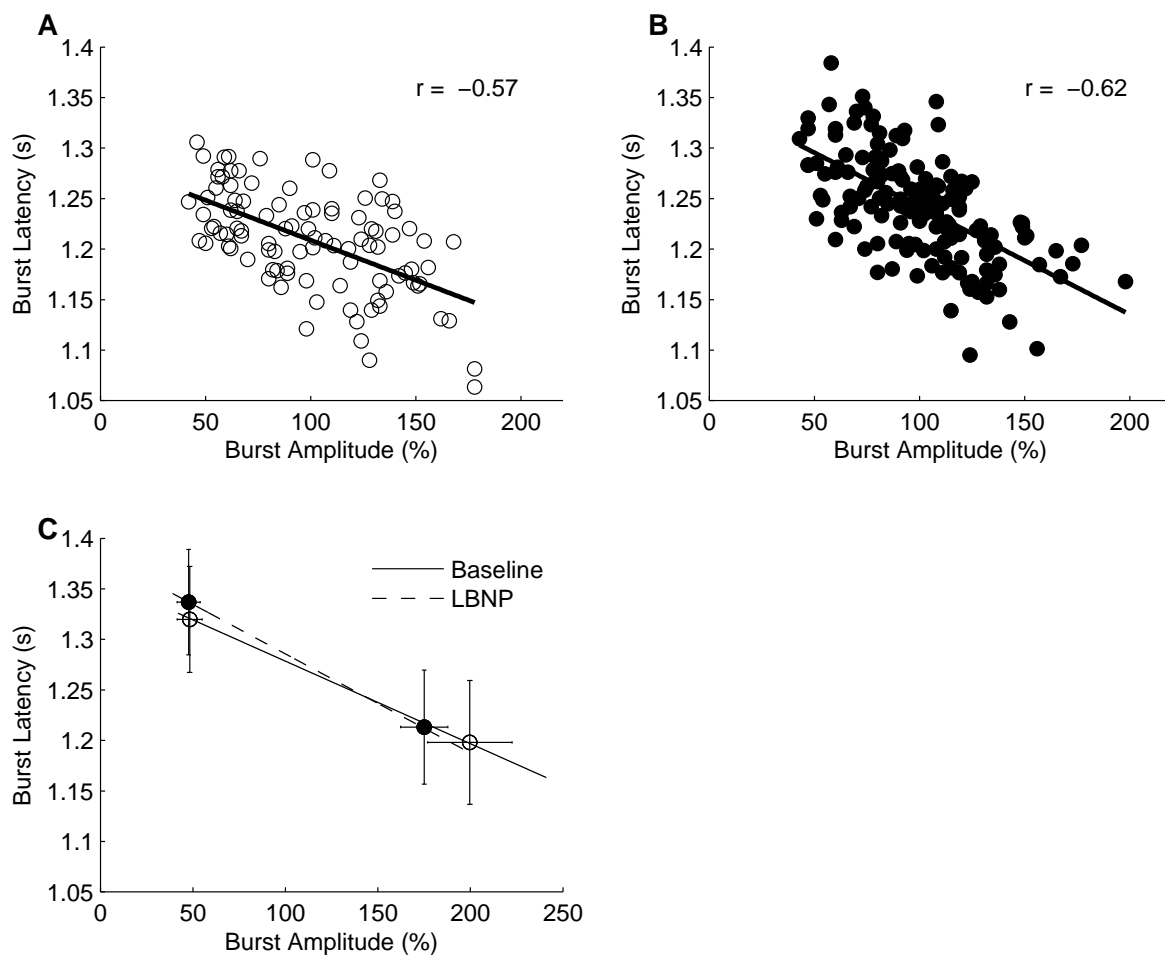


Figure 4.3: Relationship between relative integrated burst size and corresponding reflex latencies at baseline (A) and LBNP -60 mmHg (B). In each panel 100% represents mean burst size at baseline and LBNP -60 mmHg. (C) Mean response relation (i.e., reflex latency vs. burst size) during baseline (circle-line) and LBNP -60 mmHg (filled circle - dashed line) ($n=7$). Mean values are from each subject's lowest and highest burst amplitude at baseline (circle) and LBNP (filled circle). Error bars indicate SD. Baseline regression: $y = -0.00082x + 1.36$, LBNP regression $y = -0.00098x + 1.38$.

Action Potential Analysis

For sympathetic action potential analyses, 77 ± 21 integrated sympathetic bursts consisting of a total of 866 ± 499 detected action potentials at baseline and 98 ± 38 bursts consisting of a total of 1205 ± 908 detected action potentials at LBNP -60 mmHg were analyzed per subject. Compared to baseline, action potentials per minute (156 ± 91 vs. 420 ± 255 spikes.min⁻¹, $P < 0.05$) and action potentials per 100 heart beats (271 ± 172 vs. 557 ± 388 spikes.100 heart beats⁻¹, $P < 0.05$) were increased significantly during LBNP -60 mmHg. This increase in total action potential content over time was due to the increase in burst frequency and burst incidence because the number of action potentials per integrated burst at baseline was not changed by LBNP -60 mmHg (see Table 4.1).

The number of distinct “clusters” of action potentials was not different when detected action potentials were binned based on peak-to-peak amplitude at LBNP -60 mmHg and the same bin size was used for clustering at baseline, (see Table 4.1). A representative example of detected sympathetic action potential clusters is shown in Figure 4.4. The extracellular action potential in human MSNA is triphasic and templates similar to those produced in the current study have been shown in [6, 19].

Table 4.1: Post-ganglionic sympathetic action potentials (AP) and action potential clusters within sympathetic bursts detected at baseline and LBNP -60 mmHg for each participant.

| Subject | Baseline | | LBNP -60 mmHg | |
|---------|-----------|-----------------|---------------|-----------------|
| | AP/bursts | clusters/bursts | AP/bursts | clusters/bursts |
| 1 | 10 | 6 | 11 | 6 |
| 2 | 9 | 5 | 9 | 5 |
| 3 | 7 | 3 | 10 | 5 |
| 4 | 20 | 8 | 17 | 7 |
| 5 | 6 | 3 | 5 | 4 |
| 6 | 18 | 9 | 24 | 11 |
| 7 | 9 | 5 | 9 | 5 |
| Mean±SD | 11 ± 6 | 6 ± 2 | 12 ± 6 | 6 ± 2 |

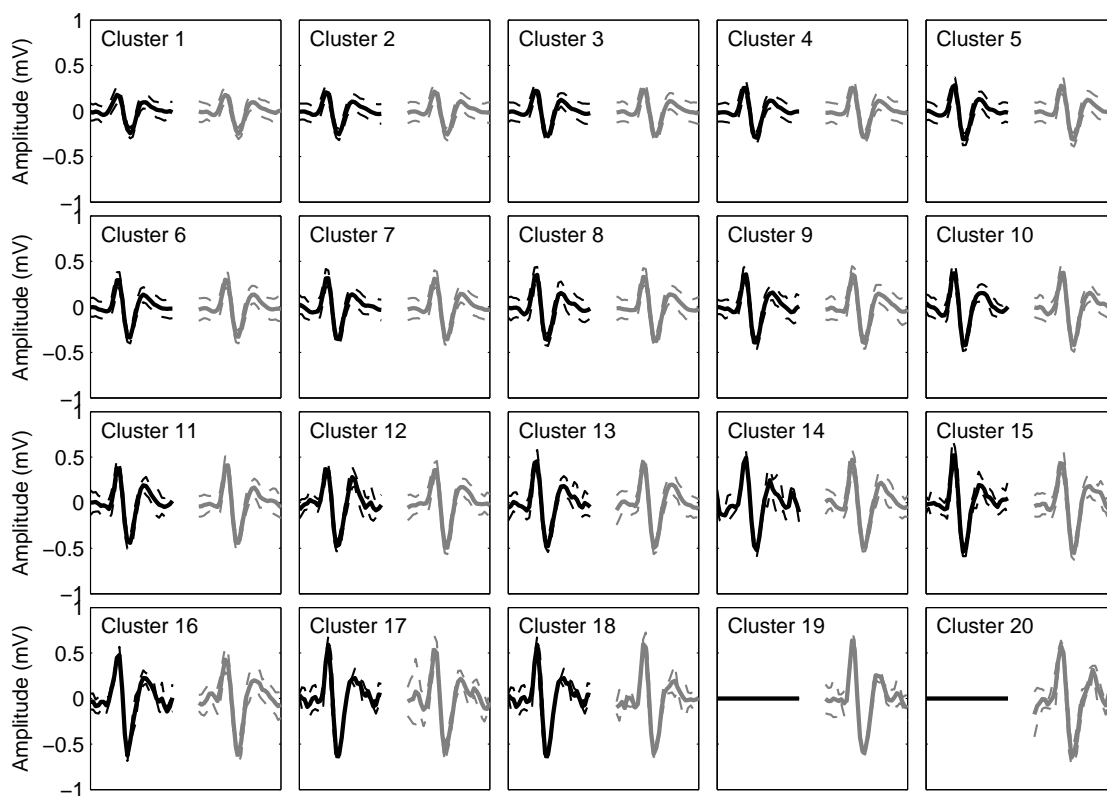


Figure 4.4: Mean action potential clusters. Representation of mean post-ganglionic sympathetic action potential clusters detected at baseline shown with black color (93 bursts, 971 action potentials) and at LBNP -60 mmHg shown with gray color (148 bursts, 1652 action potentials) in one participant. Solid and dashed lines represent means and standard deviations of cluster amplitudes. Clusters are binned based on peak-to-peak amplitude of each action potential.

Using linear regression analysis, there were strong relationships between relative integrated burst size and the number of action potentials per sympathetic burst both at baseline, $r = 0.76 \pm 0.1$ (range 0.61 to 0.88) ($P < 0.001$ in all subjects) and LBNP -60 mmHg, $r = 0.74 \pm 0.11$ (range 0.61 to 0.85) ($P < 0.001$ in all subjects). There were moderate to strong relationships between relative integrated burst size and the number of active action potential clusters at baseline $r = 0.6 \pm 0.12$ (range 0.47 to 0.77) ($P < 0.001$ in all subjects) as well as LBNP -60 mmHg, $r = 0.6 \pm 0.14$ (range 0.44 to 0.83) ($P < 0.001$ in all subjects). In addition, the number of detected action potentials and the number of distinct clusters within a given sympathetic burst were strongly correlated at baseline ($r = 0.7 \pm 0.1$, $P < 0.001$) (range 0.55 to 0.81) and at LBNP -60 mmHg ($r = 0.74 \pm 0.03$, $P < 0.001$) (range 0.69 to 0.8). Figure 4.5 represents these linear relationships between a) relative integrated burst size and the number of action potentials per burst, b) the relative integrated burst size and the number of unique action potential clusters per burst, and c) the number of action potentials versus the number of unique action potential clusters per bursts for one subject. Similar patterns in these relationships were observed for the remaining subjects (see Figure 4.5 section A3, B3 and C3 for mean responses).

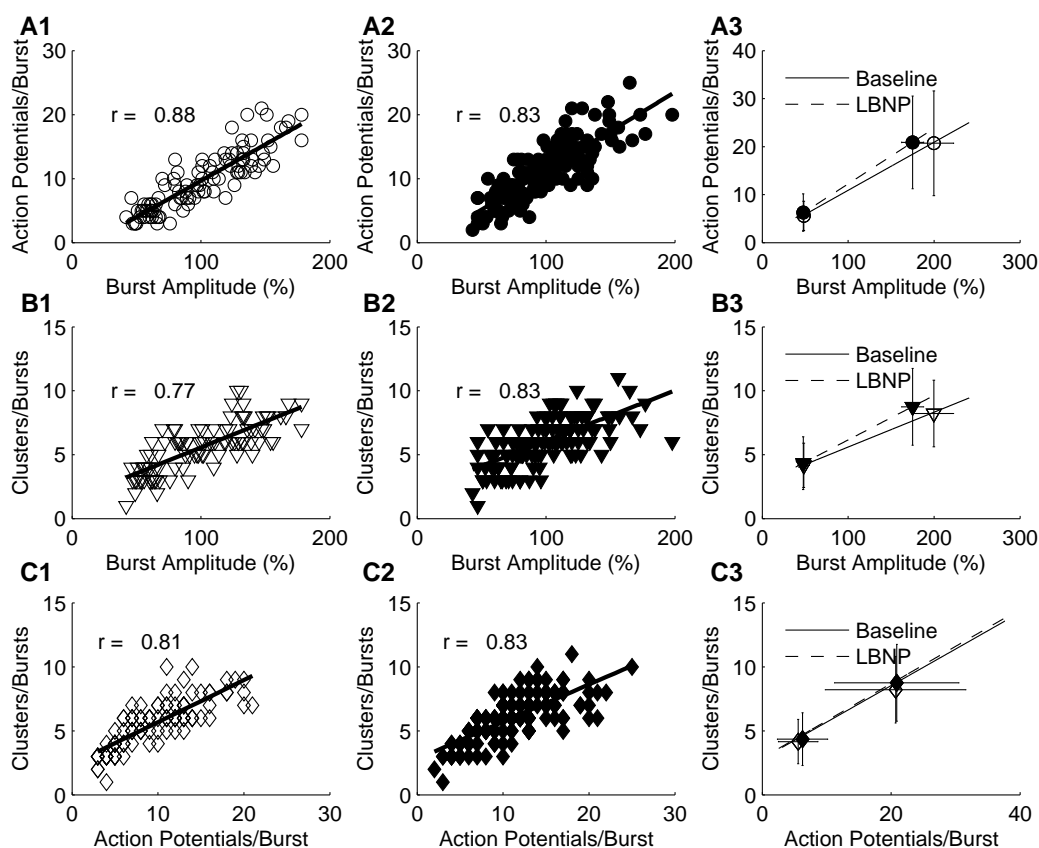


Figure 4.5: Relationship between action potential content and relative integrated burst size during baseline and LBNP. Number of post-ganglionic sympathetic action potentials as a function of relative integrated burst size at baseline (A1) and LBNP -60 mmHg (A2)(100% represents mean burst size at baseline and LBNP -60 mmHg). (A3) Mean response relations (i.e., number of action potential vs. burst size) during baseline (circle-line) and LBNP -60 mmHg (filled circle - dashed line) ($n=7$). Mean values are from each subject's lowest and highest burst amplitude at baseline (circle) and LBNP (filled circle). Baseline regression: $y = 0.1002x + 0.87$, LBNP regression $y = 0.1157x + 0.65$. Number of clusters occurring per burst as a function of relative integrated burst size at baseline (B1) and LBNP -60 (B2). (B3) Mean response relations (i.e., number of unique action potential cluster vs. burst size) during baseline (circle-line) and LBNP -60 mmHg (filled circle - dashed line) ($n=7$). Mean values are from each subject's lowest and highest burst amplitude at baseline (circle) and LBNP (filled circle). Baseline regression: $y = 0.0273x + 2.87$, LBNP regression $y = 0.0347x + 2.68$. Relationship between the number of post-ganglionic sympathetic action potentials and clusters occurring per burst at baseline (C1) and LBNP -60 mmHg (C2). (C3) Mean response relations (i.e., number of unique action potential cluster vs. number of action potentials) during baseline (circle-line) and LBNP -60 mmHg (filled circle - dashed line) ($n=7$). Mean values are from each subject's lowest and highest number of action potentials per sympathetic burst at baseline (circle) and LBNP (filled circle). Baseline regression: $y = 0.29x + 2.82$, LBNP regression $y = 0.29x + 2.88$. Error bars indicate SD. r values represent correlation coefficient between variables for each scatter plot.

The relationship between the occurrence of individual action potential clusters as a function of burst amplitude in one subject is shown in Figure 4.6A during baseline and in Figure 4.6B at LBNP -60 mmHg. In general, action potential clusters present at rest were also present during LBNP. Also, the larger action potential clusters tended to fire within larger bursts but not smaller bursts. At both baseline and LBNP -60 mmHg action potential cluster latency decreased in each subject as an inverse function of peak-to-peak amplitude. The mean response was fitted using an exponential function ($R^2 = 0.9863, P = 0.0015$) at baseline and ($R^2 = 0.9890, P = 0.0017$) at LBNP -60 mmHg. This exponential pattern was consistent with the well-defined relationship between action potential amplitude (proportional to the square of axon diameter) and conduction velocity [20] (see Figure 4.7). It was observed that the whole latency-size profile shifted upward around 9.5 ms during LBNP as the integrated mean reflex latency increased around 10 ms. The increase in mean reflex latency during LBNP was also reported in [21].

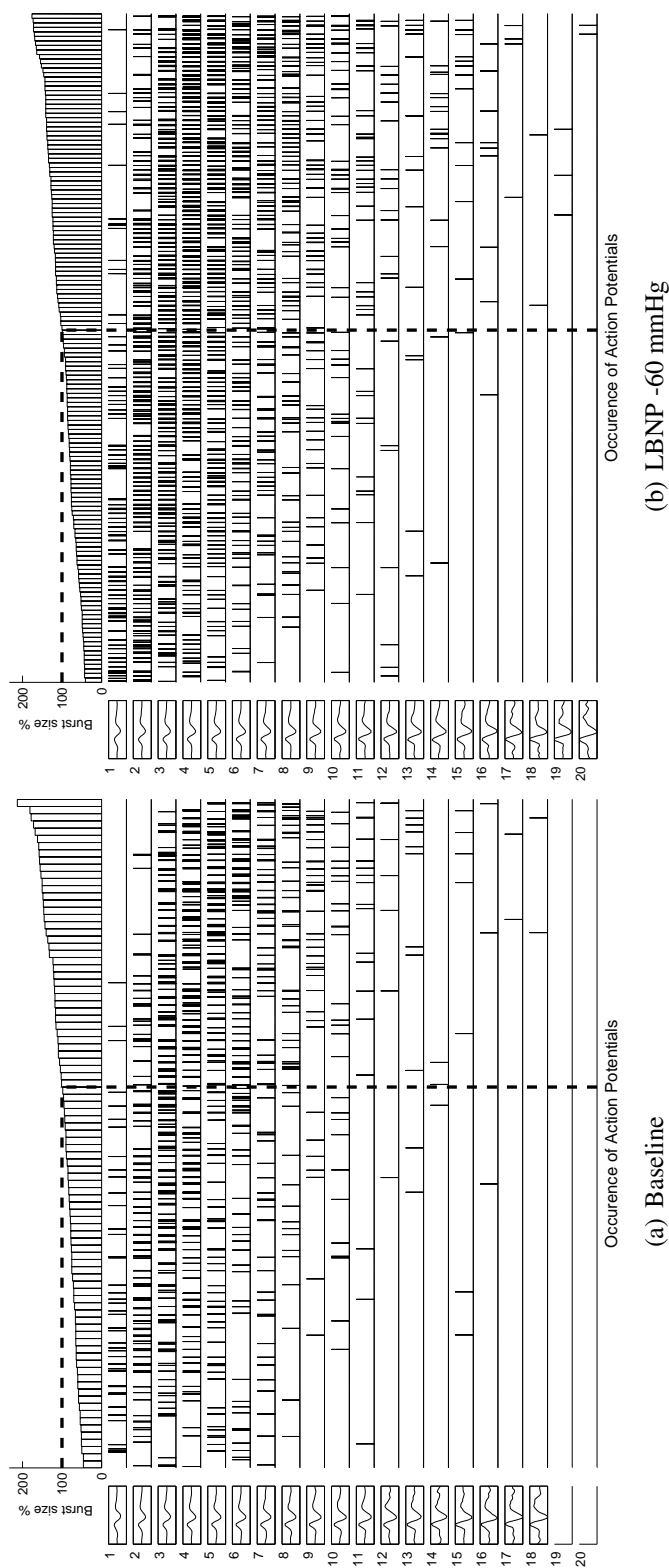


Figure 4.6: The relationship between the occurrence of individual action potential clusters as a function of burst amplitude in one subject during baseline (A) and LBNP -60 mmHg (B). In each section A or B, integrated sympathetic bursts are ordered by burst size where 100 % represents mean burst size at baseline in A and at LBNP -60 mmHg in B. Below the sympathetic burst size, occurrences of post-ganglionic sympathetic action potentials as a function of integrated burst size are indicated for each action potential cluster (left panel). Note that large action potential clusters are predominately recruited at larger bursts. Data presented are from the same participant presented in Figure. 4.4. (black and gray clusters for baseline and LBNP, respectively). Notice that the firing pattern of action potentials is similar during baseline and LBNP where large clusters occur during the large bursts. Also two new clusters (cluster 19 and 20) exist during LBNP but not during baseline.

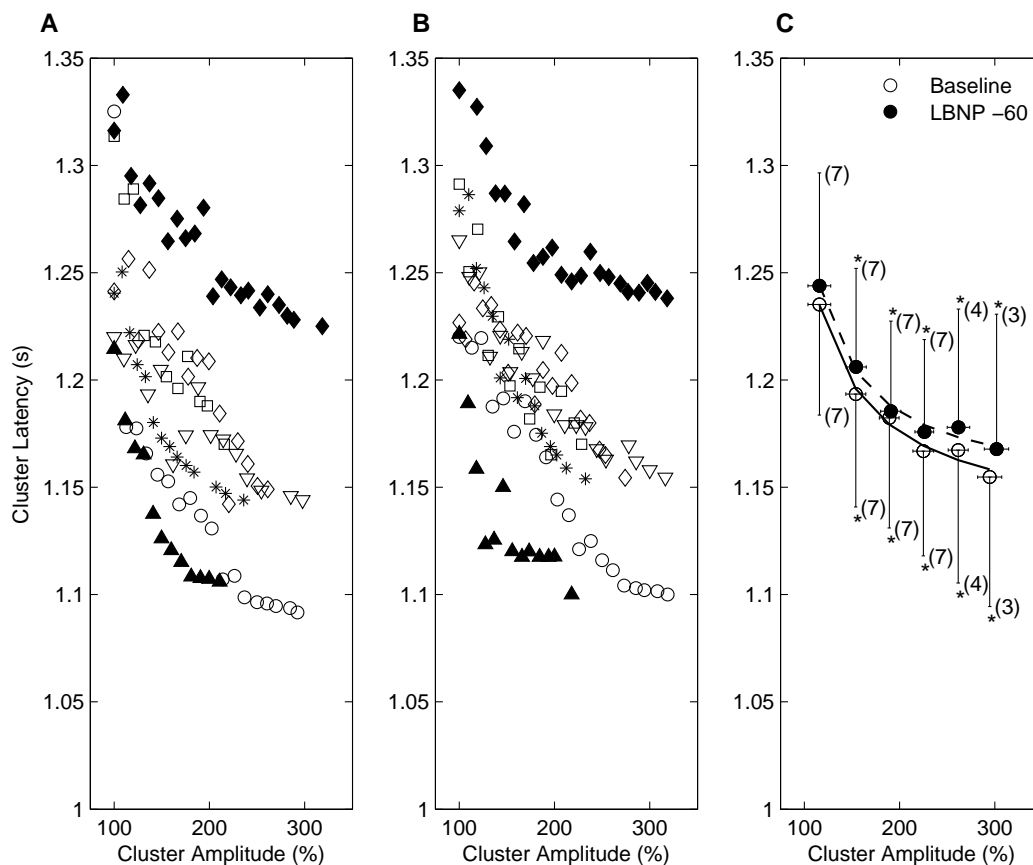


Figure 4.7: Mean action potential latency for each cluster as a function of normalized cluster amplitude (cluster 1 = 100%) for each participant during baseline (A) and at LBNP -60 mmHg (B). Mean cluster latency, binned across participants, as a function of normalized cluster amplitude during baseline and LBNP -60 mmHg (C). Numbers indicate the number of subjects per bin. The decrease in cluster latency as a function of amplitude was fit with a modified exponential decay (see text)(solid-line base-line, dashed-line LBNP). * Latency significantly different from first bin, $P < 0.05$ in both baseline and LBNP -60 mmHg.

As mentioned above, the effect of any action potential summation (i.e. two action potentials firing at exactly the same time to produce a summated action potential waveform) within larger bursts of activity was tested using a simulation. The simulation results indicated that the probability of complete overlap and summation to produce a single, larger amplitude, waveform (i.e., the time difference between the arrival times of the two spikes ≤ 0.3 ms) was around 0.28%. However, partial overlap occurred when two action potentials fired within > 0.3 and ≤ 2 ms with a probability of 3%. Within this range, action potentials with a separation of > 0.7 ms could be detected as distinct waveforms and only action potentials with a separation > 1.4 ms were classified further based on peak-to-peak amplitude. For a complete performance evaluation of our spike detection algorithm on overlapping spikes see [14]. Notice that this cut-off of 1.4 ms will also capture multiple firings of single units that appear to display maximal instantaneous firing rates of up to 230 Hz in single-unit sympathetic recordings [6, 7].

4.3.2 Baseline vs. LBNP -80 mmHg

Figure 4.8 shows an example of the raw MSNA data at baseline and LBNP -80 mmHg. Notice the increase of the amplitude of integrated sympathetic bursts during LBNP -80 mmHg for this individual. Table 4.2 compares the sympathetic bursts parameters (i.e., burst amplitude, burst latency, burst frequency and burst incidence) for group (B). It was observed that the LBNP -80 mmHg increased burst frequency and burst incidence in both subjects. However, the burst latency did not change in this group. The amplitude of the sympathetic bursts were increased about 80% in subject 8 and 34% in subject 7. The total number of action potentials per sympathetic bursts and the number of active action potential clusters per sympathetic bursts were increased for subject 8 but not for subject 7 (see Table 4.3.) Figure 4.9A-B illustrates the relationship between the occurrence of individual action potential clusters as a function of burst amplitude in subject 8 during baseline and LBNP -80 mmHg, respectively and shows the increased firing of action potentials during LBNP.

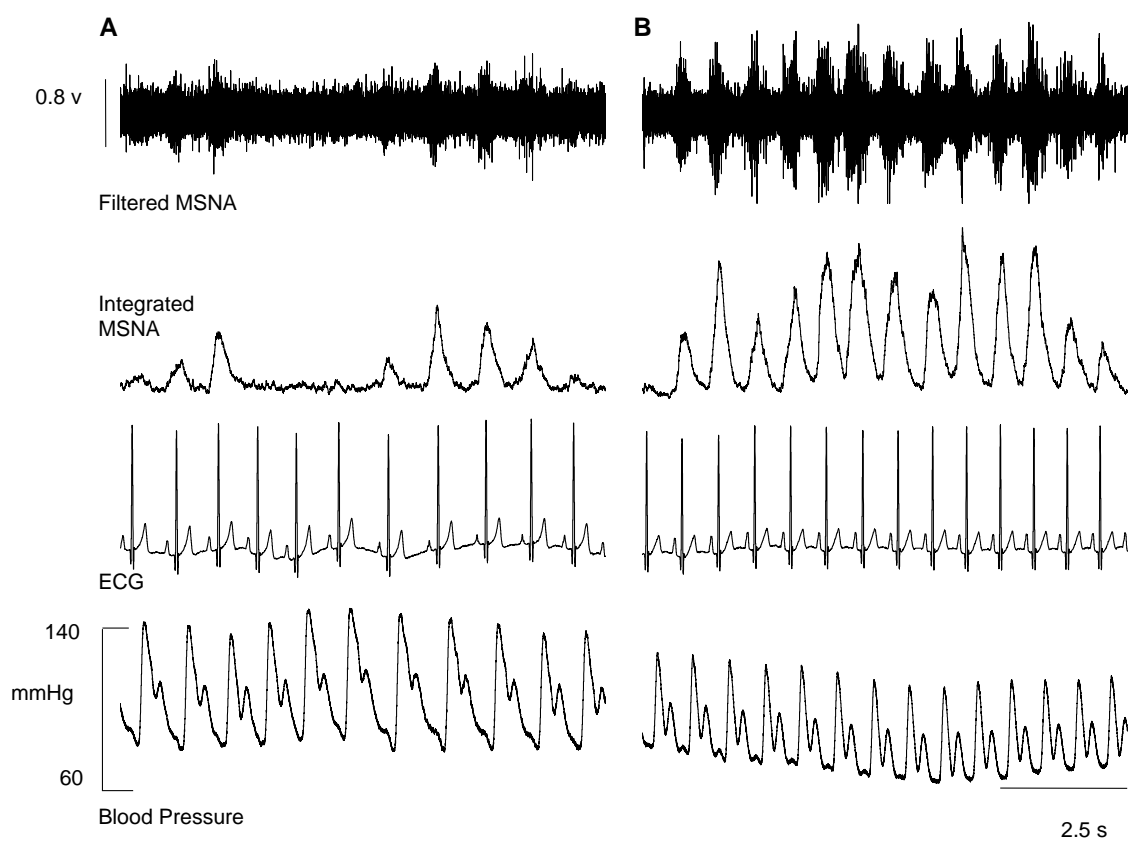


Figure 4.8: A representative example of filtered raw and integrated muscle sympathetic nerve activity at rest (A) and LBNP -80 mmHg (B).

Table 4.2: Sympathetic burst parameters at baseline and LBNP -80 mmHg for group (B).

| Burst Parameters | Subject 7 | | Subject 8 | |
|---------------------|-----------|---------------|-----------|---------------|
| | Baseline | LBNP -80 mmHg | Baseline | LBNP -80 mmHg |
| Burst Amplitude (v) | 0.13 | 0.18 | 0.3 | 0.54 |
| Burst Latency (s) | 1.29 | 1.29 | 1.37 | 1.37 |
| Burst/min | 17 | 30 | 29 | 70 |
| Burst/100 hb | 35 | 50 | 44 | 80 |

Table 4.3: Post-ganglionic sympathetic action potentials (AP) and action potential clusters within sympathetic bursts detected at baseline and LBNP -80 mmHg for group (B).

| Subject | Baseline | | LBNP -80 mmHg | |
|---------|-----------|-----------------|---------------|-----------------|
| | AP/bursts | clusters/bursts | AP/bursts | clusters/bursts |
| 7 | 9 | 5 | 11 | 5 |
| 8 | 13 | 5 | 33 | 9 |
| Mean±SD | 11 ± 3 | 5 ± 0 | 22 ± 16 | 7 ± 3 |

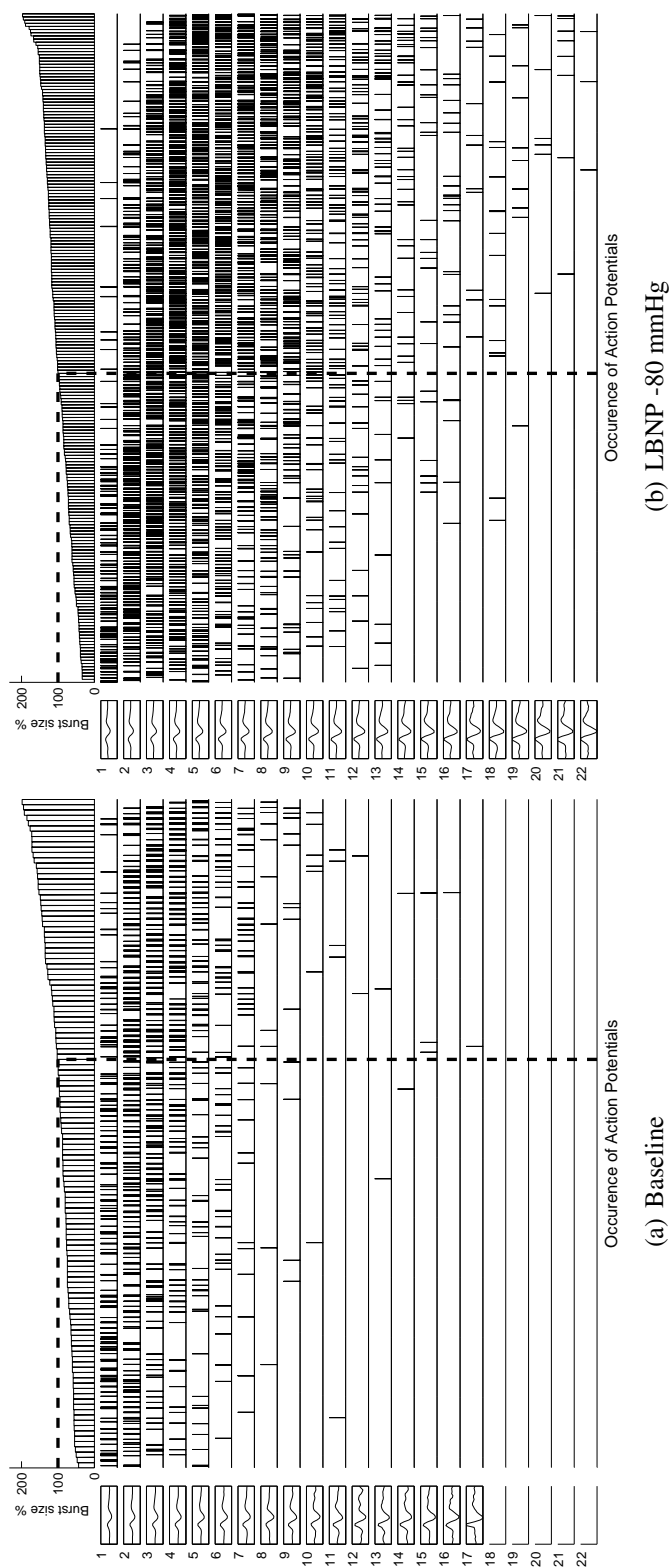


Figure 4.9: The relationship between the occurrence of individual action potential clusters as a function of burst amplitude in one subject during baseline (A) and LBNP -80 mmHg (B). In each section A or B, integrated sympathetic bursts are ordered along the top by burst size where 100 % represents mean burst size at baseline (A) and LBNP -80 mmHg (B) separately. Below, occurrences of post-ganglionic sympathetic action potentials as a function of integrated burst size are indicated for each action potential cluster (numbers in left panel show action potential clusters). Notice that large action potential clusters are predominately present within larger bursts. Data presented are from the same participant presented in Figure. 4.4. (black and gray clusters for baseline and LBNP, respectively). Notice the increase of the activity of pre-existing action potential clusters (cluster 1-17) and firing of the new additional clusters (cluster 18-22) during LBNP -80 mmHg.

4.4 Discussion

There were two important new findings of the current study. First, clusters of larger axons exhibited shorter latency and, from a probabilistic perspective, were more likely to be present in larger bursts. Second, this range of action potential size and latency was observed at rest and persisted unaltered during the orthostatic stress of -60 mmHg of LBNP. Thus, the results indicate that there exists a fundamental pattern of recruitment of additional larger, faster conducting neurons as the sympathetic bursts become stronger (i.e., larger amplitude bursts) and that moderate levels of baroreceptor unloading do little to modify this fundamental pattern.

Although LBNP increased burst frequency and burst incidence, it did not change the number of detected action potentials or the number of distinct clusters within a sympathetic burst. This latter observation implies that the same population of neurons at baseline fires more often during LBNP -60 mmHg. Yet, within each condition, there appears to be a recruitment strategy whereby the larger action potentials are recruited with a lower probability and, once recruited, contribute to the larger integrated MSNA burst.

4.4.1 Integrated burst and action potential Analysis

The integrated bursts were explained by a baroreflex mechanism as their occurrence was linearly related to diastolic blood pressure. However, the strength of each integrated burst was not explained by blood pressure, consistent with the understanding that burst occurrence, but not strength, is under baroreflex modulation [5], at least when assessed under conditions of supine rest when baroreflex inputs are strong. The current study extends this understanding to high (but not extreme) levels of baroreceptor unloading.

Recently, we reported observations that severe chemoreflex activation produced important increases in the strength of integrated MSNA bursts in humans [22]. This earlier study revealed that the pattern of action potential recruitment during breath-hold displayed an ordered pattern whereby larger bursts were more likely to contain larger action potentials with faster

conduction velocity. This earlier study also indicated that progressive and severe chemoreflex stress can elicit very large bursts of MSNA with the conclusion that large action potentials are reserved for high stress circumstances. However, this earlier study did not emphasize action potential discharge patterns at baseline. The current data suggest that this ordered pattern of sympathetic action potential recruitment is present even under baseline conditions and may, therefore, not necessarily be reflex-specific, but rather be evidence for a generalized principle of postganglionic sympathetic neural recruitment.

However, the conclusion of a generalized sympathetic discharge pattern, that is extended by severe chemoreflex stress, raises the question of why baroreceptor unloading would not lead to a greater proportion of larger axons being recruited, if they are supposedly reserved for high stress circumstances. LBNP of -60 mmHg is analogous to upright posture which can elicit ~ 300% increase in sympathetic outflow and is certainly a strong and physiologically relevant stress. Nonetheless, it remains possible that this level of baroreceptor unloading is not severe enough to elicit the recruitment of latent postganglionic neurons. To test this idea, we examined the MSNA outflow in two individuals in whom the MSNA recording site was maintained at -80 mmHg of LBNP. These preliminary data are provided in Figure 4.9. These data indicate severe baroreceptor unloading can lead to the appearance of new and larger amplitude action potential clusters indicative of a latent population of neurons that are recruited during severe stress, just like the chemoreflex responses reported previously [22]. However, this new population of action potentials was elicited in only one of two individuals, suggesting that individual variations exist in terms of post-ganglionic recruitment of MSNA at high stress levels. We do not know if this reflects the severity of the baroreflex stress which at -80 mmHg may be closer to maximal tolerance in one subject than the other.

The mechanisms mediating varying levels of action potentials of different recruitment thresholds are likely related to the proportion and activity of strong versus weak pre-ganglionic inputs to post-ganglionic neurons. Specifically, the pattern of strong and weak pre-ganglionic inputs to post-ganglionic neurons is recognized and known to impact post-ganglionic recruit-

ment [23, 24]. Just how this anatomical basis produces functional differences in multi-fiber recruitment of larger versus smaller axons, and burst composition, remains to be understood. Nonetheless, our findings are in agreement with the previous study by [4]. These authors, in the absence of action potential analysis, measured integrated burst reflex latencies during apnoea and LBNP and concluded that the recruitment of faster conducting sympathetic neurons might be one mechanism explaining the variation of reflex latencies between large and small sympathetic bursts. In addition, the inverse relationship between action potential amplitude and its latency follows the pattern of recruitment based on the “size principle” originally described for motor units neurons [11] which indicates that neurons with high threshold of activation have larger diameters (i.e., higher amplitude action potential) and higher conduction velocities (i.e., shorter latency) than neurons with low thresholds of activations. If this rule was valid for the human MSNA signal, it can be expected that small sympathetic bursts contain neurons that exhibit a low activation threshold and a low conduction velocity (i.e., low amplitude action potentials with longer latencies) whereas, large integrated bursts would contain these smaller action potentials as well additional neurons with higher threshold, larger amplitudes, and faster conducting velocities. Our results would support this expectation.

4.4.2 Action Potential Size - Latency Relationship

The shorter latency of larger action potential clusters is the basis of an assumption that these action potentials are generated by larger neurons. It remains possible, however, that the larger amplitude action potentials could be the result of summation of any two medium size action potential that fire at the same time [25, 26]. We believe this is possible but rare. First, the same axon will not superimpose upon itself even though it can fire at the theoretical maximum of 500 Hz. Even if such high rates were observed for single units our analysis does not classify the amplitude of any spikes with inter-spike distances of < 2 msec. Second, our simulation analysis argues against substantial superimposition of axons. It is also possible that the larger amplitude clusters simply reflect action potentials from neurons that are geographically close

to the recording electrode. However, this would not explain their shorter latency.

4.4.3 Baroreflex Control?

A common observation in integrated MSNA reports is that the baroreflex affects the probability of burst occurrence but not its size. In an analogous manner, the current data suggest that the level of baroreceptor unloading affected the number of action potentials per minute but had little impact on the recruitment of larger action potentials (i.e., the number of spikes per bursts was not different at this level of LBNP). Thus, it may be that these larger action potentials with faster conduction velocities reflect a level of control that is minimally affected by baroreflex pathways, at least, perhaps, until severe baroreceptor unloading occurs.

Although LBNP -60 mmHg produced modest increases in the amplitude of integrated bursts, it seems that this amount of increase was not the result of the recruitment of additional neurons (i.e., the number of action potentials and distinct clusters within sympathetic bursts were not significantly different at this level of LBNP). That is, the action potential clusters present during LBNP were those already present at baseline. This could be explained using a hypothetical model for arterial baroreceptor influence on MSNA presented by Kienbaum et al [5]. Based on the observation that the baroreflex regulated the occurrence of sympathetic bursts but not their strength, these authors suggested that two different sites of control were involved in the modulation of these two independent features of sympathetic outflow. These earlier conclusions were based on observations made in resting man. The current data, assessed at a moderate level of orthostatic stress, support and extend this hypothesis to a wider range of baroreceptor loading. Nonetheless, one may argue that severe baroreflex stress may be required. However, the standard approach of relating burst probability to diastolic pressure as a measure of baroreflex control, consistently indicates a weak baroreflex control over burst strength. However, removal of some baroreceptor input in the current study did result in some shift towards increased burst size and probability of larger action potentials. Therefore, the baroreflex mechanism may exert some regulatory influence over action potential recruitment

and burst strength. Our data from two individuals at -80 mmHg LBNP support that idea that more severe orthostatic stress may expose a greater inhibitory role of baroreceptor inputs on MSNA burst strength with a low-pressure threshold at least in some individuals. In support of this conjecture, the recent work by [27] showed that the severe levels of LBNP (e.g., suction ≥ 80 mmHg) may affect the both amplitude and reflex latency of integrated bursts significantly. Thus, one would expect that the higher levels of LBNP might affect the action potential content differently than that of lower/medium levels of LBNP.

4.4.4 Limitations

The current approach for action potential detection in MSNA bursts provides information on the size and latency of action potentials within MSNA bursts. A limitation of the approach is that it cannot be determined whether separate action potentials with the same shape (i.e., size) are from the same or different neurons. Generally, those clusters active during baseline continued to be active during LBNP. However, whether or not these are the same neurons is not known. All that can be said here is that action potentials of similar size are present both at rest and during LBNP.

Also, the performance of the correct detection of action potentials by this method is a function of the signal-to-noise ratio. We have tested the accuracy of the current action potential detection method using a simulated MSNA data with varying sets of burst rate, action potential rate and signal-to-noise ratios [14]. In the present study, the average signal-to-noise ratio for the data was 3.7 ± 0.3 . Based on a previous performance analysis [14] this level of signal-to-noise would produce a correct detection rate of $91 \pm 11\%$ and a false positive detection rate of 3%. In addition, the observed exponential relationship between size and latency of action potentials suggests that large action potentials fire in the first part of the burst; moreover, any complete overlapping action potential causing a larger action potential could occur anywhere within a sympathetic burst which is not necessarily fitted with the observed size-latency relationship. Therefore, the potential for the larger action potentials to be due to signal summation, or to be

a function of the analytical approach, is small.

4.4.5 Summary and Conclusions

Earlier, Wallin et al [4] pondered the mechanism(s) producing the shorter latency of larger integrated bursts and suggested that altered synaptic delays and/or latent populations of neurons with higher recruitment thresholds and faster conduction velocities could account for such burst-by-burst variations in latency. When combined with information derived from the behavior of single sympathetic units, the current data lend support to both options of additional sympathetic outflow. This outflow can change spontaneously and such variations occur at baseline and during reflex activation. At rest, burst strength predicts not only the number of active sympathetic units but also the size and latency of these units. Thus, the current results suggest that various populations of sympathetic post-ganglionic units exist with varying recruitment thresholds and conduction velocities. Baroreceptor unloading enhances burst incidence due to the increased probability of recruiting the same action potential population that was present at baseline. The shorter latency of larger bursts, both at rest and during LBNP, is, at least partly, the result of more and faster conducting larger action potentials in the larger bursts. In conclusion, this study has provided new evidence that exposes post-ganglionic action potential discharge patterns and provides detailed information about size and latency of action potentials in human MSNA recordings. The findings indicate that a hierarchical pattern of recruitment of a new population of efferent sympathetic fibres can explain variations in MSNA burst size at rest and baroreflex unloading; moreover, the moderate levels of baroreceptor unloading do not change the pattern of neural sympathetic recruitment in human MSNA.

4.5 Acknowledgments

This work was supported by research grants from the Natural Sciences and Research Council of Canada (NSERC) to K. Shoemaker.

References

- [1] K. E. Hagbarth and A. B. Vallbo, "Pulse and respiratory grouping of sympathetic impulses in human muscle nerves," *Acta physiol scand* vol. 74, pp. 96-108, 1968.
- [2] W. Delius, K. E. Hagbarth, A. Hongell, B. G. Wallin, "General characteristics of sympathetic activity in human muscle nerves," *Acta Physiol Scand* vol. 84, pp. 65-81, 1972
- [3] B. G. Wallin and N. Charkoudian, "Sympathetic neural control of integrated cardiovascular function: insights from measurement of human sympathetic nerve activity," *Muscle and Nerve* vol. 36, pp. 595-614, 2007.
- [4] B. G. Wallin, D. Burke and S. Gandevia, "Coupling between variations in strength and baroreflex latency of sympathetic discharges in human muscle nerves," *J Physiol* vol. 474, pp. 331-338, 1994.
- [5] P. Kienbaum, T. Karlsson, Y. B. Sverrisdottir, M. Elam, B. G. Wallin BG, "Two sites for modulation of human sympathetic activity by arterial baroreceptors?" *J Physiol* vol. 531, pp. 861-869, 2001.
- [6] V. G. Macefield and B. G. Wallin, "Firing properties of single vasoconstrictor neurones in human subjects with high levels of muscle sympathetic activity," *J Physiol* vol. 516, pp. 293-301, 1999.
- [7] V. G. Macefield, B. G. Wallin, and A. B. Vallbo, "The discharge behaviour of single vasoconstrictor motoneurons in human muscle nerves," *J Physiol* vol. 481, pp. 799-809, 1994.
- [8] M. Elam and V. Macefield, "Multiple firing of single muscle vasoconstrictor neurons during cardiac dysrhythmias in human heart failure," *J Appl Physiol* vol. 91, pp. 717-724, 2001.

- [9] M. Elam, D. McKenzie and V. Macefield, "Mechanisms of sympathoexcitation: single-unit analysis of muscle vasoconstrictor neurons in awake OSAS subjects," *J Appl Physiol* vol. 93, pp. 297-303, 2002.
- [10] E. D. Adrian and D. W. Bronk, "The discharge of impulses in motor nerve fibres Part 656 II. The frequency of discharge in reflex and voluntary contractions," *Journal of Physiology* vol. 67, pp. 19-151, 1929.
- [11] E. Henneman, "Relation between size of neurons and their susceptibility to discharge," *Science* vol. 126, pp. 1345-1347, 1957.
- [12] E. Henneman, G. Somjen and D. O. Carpenter, "Functional significance of cell size in spinal motoneurons," *J Neurophysiol* vol. 28, pp. 560-580, 1965.
- [13] R. H. Westgaard and C. J. De Luca, "Motor control of low-threshold motor units in the human trapezius muscle," *J Neurophysiol* vol. 85, pp. 1777-1781, 2001.
- [14] A. Salmanpour, L. J. Brown, J. K. Shoemaker, "Spike detection in human muscle sympathetic nerve activity using a matched wavelet approach," *Journal of Neuroscience Methods* (September 8, 2010). doi:10.1016/j.jneumeth.2010.08.035.
- [15] A. Salmanpour, L. J. Brown and J. K. Shoemaker JK, "Detection of Single Action Potential in Multi-unit Postganglionic Sympathetic Nerve Recordings in Humans: A Matched Wavelet Approach," *Conf Proc IEEE Acoust Speech Signal Process* vol. 2010, pp. 554-557, 2010.
- [16] G. Sundlof and B. G. Wallin BG, "Human muscle sympathetic nerve activity at rest, relationship to blood pressure and age," *J Physiol* vol. 274, pp. 621-637, 1978.
- [17] J. Fagius, B. G. Wallin, "Sympathetic Reflex Latencies and conduction velocities in normal man," *Journal of the Neurological Sciences* vol. 47, pp. 433-448, 1980.

- [18] D. W. Scott DW, "On optimal and data-based histograms," *Biometrika* vol. 66, pp. 605-610, 1979.
- [19] J. .T. Inglis, J. B. Leeper, D. Burke and S. C. Gandevia, "Morphology of action potentials recorded from human nerves using microneurography," *Exp Brain Res* vol. 110, pp. 308-314, 1996.
- [20] H. P. Clamann, E. Henneman, "Electrical measurement of axon diameter and its use in relating motoneuron size to critical firing level," *J Neurophysiol* vol. 39, pp. 844-851, 1976.
- [21] J. Fagius, G. Sundolf, B. G. Wallin, "Variation of sympathetic reflex latency in man," *Journal of the Autonomic Nervous System* vol. 21, pp. 157-165, 1987.
- [22] C. D. Steinback, A. Salmanpour, T. Breskovic, Z. Dujic, and K. J. Shoemaker, "Sympathetic neural activation: an ordered affair," *J Physiol* (October 11, 2010), doi:10.1113/jphysiol.2010.195941, 2010.
- [23] W. Janig and E. M. McLachlan EM, "Characteristics of function-specific pathways in the sympathetic nervous system," *Trends Neurosci* vol. 15, pp. 475-481, 1992.
- [24] R. M. McAllen, D. Trevaks, "Are pre-ganglionic neurones recruited in a set order?" *Acta Physiol Scand* vol. 177, pp. 219-225, 2003.
- [25] J. W. Spickler, P. Kezdi, "Probability of spike summations in baroreceptor electro-neurograms," *J Appl Physiol* vol. 27, pp. 919-922, 1969.
- [26] M. C. Andresen and M. Yang M, "Interaction among unitary spike trains: implications for whole nerve 4 measurements," *Am J Physiol* vol. 256, pp. R997-1004, 1989.
- [27] W. H. Cooke, C. A. Rickards, K. L. Ryan, T. A. Kuusela and V. A. Convertino, "Muscle sympathetic nerve activity during intense lower body negative pressure to presyncope in humans," *J Physiol* vol. 587, pp. 4987-4999, 2009.

Chapter 5

Conclusions

During the past three decades, researchers have used microneurography to study autonomic nervous system function. This is accomplished by recording muscle sympathetic nerve activity (MSNA) which is a direct recording of sympathetic nerve activity representing post-ganglionic vasoconstrictor nerve traffic. The technique involves inserting a 200 μm diameter tungsten electrodes with a 1-5 μm uninsulated tip into a post-ganglionic nerve fiber (commonly the peroneal). This signal is then amplified, bandpass-filtered (bandwidth 700-2,000 Hz), rectified and integrated to provide a mean voltage neurogram. Studies have focused on this mean voltage neurogram because of the low signal-to-noise ratio of the raw MSNA signal. Although this traditional processing (i.e., integrating raw MSNA signal) provides a quantitative measure of sympathetic outflow, it removes very important information regarding sympathetic action potentials and how this discharge pattern contributes to the total nerve activity.

The current thesis has attempted to provide a new method for retrieving action potentials embedded within the high level of back ground noise. This technique provides detailed information about the action potential content (i.e., the total number of action potentials per sympathetic burst and the size of these action potentials) and it complements the traditional processing of MSNA signal.

We believe that the current approach can be applied to the MSNA signal for testing and

understanding the recruitment strategy of sympathetic neurons used by central nervous system to achieve the spontaneous activity and stress responses.

Major contributions of this thesis are 1) proposing a novel approach for detecting action potentials in human muscle sympathetic nerve activity and 2) its application for understanding the recruitment strategies of sympathetic neurons.

5.1 Summary of results

The main goals of Chapter 2 were 1) to examine the performance of discrete wavelet transform (DWT) and stationary wavelet transform (SWT) with non-matched wavelet (i.e., “Symlet 7” in this case) for spike detection in human MSNA signal, 2) to develop a method for finding mean action potential templates before bandpass filtering and before pre-amplification to examine the effect of band-pass filtering on action potential’s shape, and 3) to classify action potentials extracted from original filtered MSNA based on their morphology using the k-means clustering approach.

It was concluded that the SWT method performs better than the DWT method for the detection of sympathetic action potentials embedded within a high level of background noise in sympathetic recordings. This conclusion is a direct result of translation invariance of the SWT method; moreover, it is in agreement with the previous study by Brychta et al [1]. These authors also showed improved performance of the SWT method in spike detection from renal sympathetic nerve activity (RSNA) in the mice. Using an inverse filtering approach, we found the shape of the mean action potential template after the electrodes. Although the overall morphology of this mean template was similar to that of the template after band-pass filtering (i.e., both templates showed the tri-phasic waveforms), some differences were evident. The main difference was the dominant negative peak for the mean action potential template after electrodes while the mean template after bandpass filtering showed both a prominent positive peak before the dominant negative peak. This result suggests that the hardware used to ob-

tain and condition the neurogram may affect action potential morphology. Specifically, the pre-amplification, variable gain amplification and application of a band-pass filter will alter the shape of the recorded action potential. The effect of bandpass filtering on action potential's morphology was also reported in [2]. These authors suggested that the different setting of bandpass filter (i.e., different pass band) may distort the overall shape of action potential recorded by microneurography. Nonetheless, our result that the mean action potential template after electrodes has a main negative component is in agreement with the single-unit recording of C fiber action potentials reported previously [3–6].

In Chapter 3, the main objectives were 1) to increase the accuracy of action potential detection in human MSNA by designing a wavelet matched to a real mean action potential template and modifying the previous wavelet-based approaches, 2) to develop a method for realistic simulation of MSNA signal with different burst rate, spike rate and signal-to-noise ratio for evaluation of the proposed method, 3) to test and calculate the probability of the overlapping spikes in sympathetic bursts and to evaluate the performance of the proposed action potential detector methods on the overlapping spikes and 4) applying the new method on real MSNA signal obtained at rest and during LBNP protocol.

It was concluded that the matched wavelet detector (MWD), which uses the continuous wavelet transform (CWT) with matched mother wavelet, performs better than the SWT and DWT methods with a non-matched wavelet (i.e., “Symlet 7”) for detection of sympathetic action potentials in human MSNA. Specifically, the MWD offers a very low false positive rate (less than 3 % for SNRs of 1 to 5) which is an important feature for any physiologist. Also, a flexible model for simulation of MSNA signal was proposed. By combining the template with the statistical properties measured from real signals, realistic simulated MSNA signals can now be created.

Also, using a simulation, it was shown that the probability of overlapping spikes is relatively low but can happen during multi-fiber recording of MSNA signal. This is a direct result of low firing frequency of sympathetic neurons [see 3, 4] compared to other neural systems

that show high firing frequency of neurons that increase probability of overlapping spikes [see 8, 9]. The MWD method successfully detected overlapping spikes with separation of ≥ 0.7 ms.

The mean spike rates detected using the matched wavelet detector method during lower body negative pressure protocol were shown to be highly correlated to commonly used integrated burst rate ($r = 0.86$) and burst area rate ($r = 0.89$) parameters. These correlations were comparable to those previously reported with the SWT method using kurtosis analysis ($r = 0.85$ and $r = 0.91$, respectively) [10] and were improved from than those previously reported with the DWT method ($r = 0.79$, $r = 0.52$, respectively) [7].

Also, we have implemented the MWD method as stand-alone custom software written using MATLAB (version 2009a, Mathworks, Natick, MA). The complete designing and processing of a MSNA signal that is sampled at 10 KHz and 6-min long takes only 16 s on a Intel (R) Core (TM) 2 CPU 2.00-GHz personal DELL laptop with 2 GB RAM.

In Chapter 4, the main goal was to apply the MWD method presented in chapter 3 to real MSNA signal in order to study recruitment patterns of post-ganglionic sympathetic neurons during rest and baroreflex un-loading. Specifically, we were trying to answer a fundamental question: Is there an ordered pattern in the recruitment of post-ganglionic sympathetic neurons?

The main conclusion of this study indicated that there exists a hierarchical pattern of recruitment of additional larger, faster conducting neurons as the sympathetic bursts become stronger (i.e., larger amplitude bursts) and that moderate levels of baroreceptor unloading do little to modify this fundamental pattern. This study has provided significant new information on how the sympathetic nervous system grades its output during rest and baroreflex unloading.

5.2 Overall Conclusions

In conclusion, based on the work presented here, the following generalizations are concluded:

1. The SWT method performs better than the DWT method for the detection of sympathetic action potentials embedded within a high level of background noise in human

sympathetic recordings.

2. To study the effect of bandpass-filtering and signal conditioning on action potentials morphology, an inverse filtering approach can be used to estimate the shape of the mean action potential template during different stages of signal conditioning of the MSNA signal.
3. Once action potentials are extracted from raw filtered MSNA signal, K-means clustering approach can be used to classify different action potentials based on their morphology.
4. The continuous wavelet transform (CWT) that uses a matched mother wavelet performs better than the SWT and DWT methods with a non-matched wavelet for detection of sympathetic action potentials in human MSNA and it has much lower false positive rate.
5. It is possible to simulate realistic MSNA signals by using action potential templates with the statistical properties measured from real MSNA signals.
6. By using statistical information from single-unit MSNA recordings, it is possible to estimate the probability of overlapping spikes.
7. The matched wavelet detector method can detect successfully overlap spikes with separation above $0.7 \geq ms$.
8. By applying the matched wavelet detector method to real MSNA signal, it is possible to study recruitment strategy used by the sympathetic nervous system.
9. It appears that the sympathetic nervous system uses a hierarchical pattern of recruitment of sympathetic neurons based on their size. This fundamental pattern is evident at rest and may not be altered by the medium level of baroreceptor unloading.
10. This recruitment information may have important implications for how blood pressure and blood flow are controlled, and the malleability of sympathetic activation in health and disease.

5.3 Future Directions

There are some future directions that can be taken to further analyses based on the work presented here. We showed the effect of bandpass filtering on sympathetic action potential's shape in chapter 2. Currently, there are two different band-pass settings used in multi-fiber (700-2000 Hz) and single-fibre (300-5000 Hz) recordings of muscle sympathetic nerve activity. The effect of these different band-pass filter settings on signal conditioning of action potentials can be further investigated. In general, a less restrictive pass-band might be a better choice for recording sympathetic action potentials.

The matched wavelet detector developed in chapter 3 can detect and identify spikes of different sizes. Peak-to-peak clustering of detected action potentials can provide different classes of spikes based on their size. A limitation of this approach is that it cannot be determined whether separate action potentials with the same shape (i.e., size) are from the same or different neurons. Therefore, implementing a statistical method to automatically sort the detected spikes into classes derived from individual neurons would be a useful addition.

While our algorithm is designed to detect and extract sympathetic nerve activity from background noise, it cannot be applied to recordings that reflect the mixture of more than one type of nerve recordings. Presence of motor unit activity can create a such mixture nerve activity during recording of MSNA signal. Developing a method for separating such mixed signals would be very beneficial. The challenge here is that these nerve types produce similar AP shapes.

The analysis presented in chapter 4 for understanding the recruitment of post-ganglionic sympathetic neurons in healthy individuals can be applied to study neural recruitment properties in patients with disorders that involve the autonomic nervous system (e.g., hypertension, congestive heart failure). This latter is one the ultimate goals of the work presented in this thesis.

Finally, it is hoped that the sympathetic action potential detection procedures developed here can be applied to understand further the recruitment strategies used by the sympathetic

nervous system, how these strategies are modified by disease and how neuroplastic phenomena can be explained in the peripheral nervous system.

References

- [1] R. J. Brychta, S. Tuntrakool, M. Appalsamy, N. R. Keller, D. Robertson, R. Shiavi and A. Diedrich, "Wavelet methods for spike detection in mouse renal sympathetic nerve activity," *IEEE Trans. Biomed. Eng.*, vol. 54, no. 1, pp. 82-93, Jan. 2007.
- [2] J. T. Inglis, J. B. Leeper, D. Burke and S. C. Gandevia, "Morphology of action potentials recorded from human nerves using microneurography," *Exp Brain Res* vol. 110, pp 308-314, 1996.
- [3] V. G. Macefield, B. G. Wallin , and A. B. Vallbo, "The discharge behaviour of single vasoconstrictor motoneurons in human muscle nerves," *J Physiol* vol. 481, pp. 799-809, 1994.
- [4] V. G. Macefield and B. G. Wallin, "Firing properties of single vasoconstrictor neurones in human subjects with high levels of muscle sympathetic activity," *J Physiol* vol. 516, pp. 293-301, 1999.
- [5] H. Murai, S. Takata, M. Maruyama, M. Nakano, D. Kobayashi, K. Otowa, M. Takamura, T. Yuasa, S. Sakagami, S. Kaneko, "The activity of a single muscle sympathetic vasoconstrictor nerve unit is affected by physiological stress in humans," *Am J Physiol Heart Circ Physiol* vol. 290, pp. H853-60, 2005.
- [6] E Lambert, N Straznicky, M Schlaich, M Esler, T Dawood, E Hotchkin, G Lambert, "Differing pattern of sympathoexcitation in normal-weight and obesity-related hypertension," *Hypertension* vol. 50, pp. 862-8, 2007.

- [7] A. Diedrich, W. Charoensuk, R. J. Brychta, A. C. Ertl and R. Shiavi, "Analysis of raw microneurographic recordings based on wavelet de-noising technique and classification algorithm: Wavelet analysis in microneurography," *IEEE Trans Biomed Eng* vol. 50, pp. 41-50, 2003.
- [8] M. C. Andresen and M. Yang M, "Interaction among unitary spike trains: implications for whole nerve measurements," *Am J Physiol* vol. 256, pp. R997-1004, 1989.
- [9] J. W. Spickler, P. Kezdi, "Probability of spike summations in baroreceptor electroneurograms," *J Appl Physiol* vol. 27, pp. 919-922, 1969.
- [10] R. J. Brychta, R. Shiavi, D. Robertson, A. Diedrich, "Spike detection in human muscle sympathetic nerve activity using the kurtosis of stationary wavelet transform coefficients," *J Neurosci Meth* vol. 160, pp. 359-367, 2007.

Curriculum Vitae

Name: Aryan Salmanpour

Education

Post-Secondary Education and Degrees: 2007-2010 Ph.D.,
Electrical and Computer Engineering (Biomedical Systems)
the University of Western Ontario, London, ON, Canada

2002-2005 M.Sc.,
Biomedical Engineering (Bio-electric)
Amirkabir University of Technology (Tehran Polytechnic), Tehran, Iran

1998-2002 B.Sc., (Hons)
Electrical/Biomedical Engineering
Science and Research Branch, Azad University, Tehran, Iran

Related Work Experience: Teaching Assistant
The University of Western Ontario
2007 - 2010

Publications:

- **Journal Papers:**

1. **A Salmanpour**, LJ Brown and JK Shoemaker, "Spike detection in human muscle sympathetic nerve activity using a matched wavelet approach", *Journal of Neuroscience Methods* vol. 193, pp. 343-355, 2010.
2. **A Salmanpour**, LJ Brown, C Steinback, CW Usselman, R Goswami, Y Liu and JK

Shoemaker, “Relationship between size and latency of action potentials in human muscle sympathetic nerve activity,” *Journal of Neurophysiology*.

3. CD Steinback, **A Salmanpour**, T Breskovic, Z Dujic, and JK Shoemaker, “Sympathetic neural activation: an ordered affair,” *Journal of Physiology* vol. 588, pp. 4825-4836, 2010.
4. T Breskovic, CD Steinback, **A Salmanpour**, Z Dujic, and JK Shoemaker, “Recruitment pattern of sympathetic neurons during functional residual capacity and total lung capacity apnea in breath hold divers and controls”, *Experimental Physiology*.
5. M Zamir, R Goswami, L Liu, **A Salmanpour**, JK Shoemaker “Myogenic activity in autoregulation during low frequency oscillations,” *Autonomic Neuroscience* (2010) doi:10.1016/j.autneu.2010.07.029.

- **Peer-Reviewed Conference Proceedings:**

1. **A Salmanpour**, LJ Brown and JK Shoemaker, “Detection of Single Action Potential in Multi-unit Postganglionic Sympathetic Nerve Recordings in Humans: A Matched Wavelet Approach,” *IEEE International conference on Acoustics Speech and Signal Processing (ICASSP)* pp. 554-557, 2010.
2. **A Salmanpour**, LJ Brown and JK Shoemaker, “Detection and Classification of Raw Action Potential Patterns in Human Muscle Sympathetic Nerve Activity,” *International conference of the IEEE Engineering in Medicine and Biology Society (EMBS)*, pp. 2928-31, 2008.
3. **A Salmanpour**, LJ Brown and JK Shoemaker, “Performance Analysis of Stationary and Discrete Wavelet Transform for Action Potential Detection from Sympathetic Nerve Recordings in Humans,” *International conference of the IEEE Engineering in Medicine and Biology Society (EMBS)* pp. 2932-5, 2008.

- **Published Abstracts:**

1. **A Salmanpour**, LJ Brown and J Kevin Shoemaker, “Action potential content in human muscle sympathetic nerve activity”, *Autonomic Neuroscience*, vol. 149, pp. 76-77, 2009.
2. CD Steinback, **A Salmanpour**, MF Frances and JK Shoemaker, “Action potential content in human postganglionic sympathetic nerve activity during severe reflex mediated autonomic arousal,” *Autonomic Neuroscience*, vol. 149, pp. 81, 2009.
3. CD Steinback, **A Salmanpour**, T Breskovic, Z Dujic, JK Shoemaker, “The recruitment pattern of post-ganglionic sympathetic neurons from multi-unit recordings in humans,” *Ontario Exercise Physiology* 2010.